

# Advances in enantioselective resolution applying preferential crystallization and enzymatic racemization

## **Dissertation**

for the award of the degree

**Doktoringenieurin**

**(Dr.-Ing.)**

by **M. Sc. Thiane Carneiro**

Date of birth: December 7, 1988, in Fortaleza, Brazil

Accepted by the Faculty of Process and Systems Engineering  
of the Otto-von-Guericke-University Magdeburg

Reviewer:	apl. Prof. Dr. Heike Lorenz	(Chairman)
	Prof. Dr. Andreas Seidel-Morgenstern	(Reviewer)
	Prof. Dr. Stephan Lütz	(Reviewer)
	Dr. Jan von Langermann	(Reviewer)

Submitted on: February 22, 2021

Graduation Colloquium on: June 21, 2021



## Abstract

Enantiomers are pairs of identical chiral molecules that have different spatial arrangement. They present similar physical and chemical properties, but can interact differently in living organisms. When used as chiral drug substances, enantiomers often promote distinct therapeutic and toxicological effects. For that reason, regulatory agencies demand for the provision of enantiopure substances. Enantiomers are often chemically synthesized as 50:50 mixtures which must be separated subsequently. Preferential Crystallization (PC) is a powerful, cost-effective technique to purify enantiomers that crystallize as conglomerates. PC is modeled using laborious population balance equations and there is a lack of simple tools allowing analysis of productivity in early process design. The method also suffers from maximum yield limitation of 50%. A racemization step can be integrated to convert the unwanted enantiomer into the target, increasing the theoretical yield to 100%. Certain enzymes are attractive racemization catalysts that are active under mild conditions required for PC.

In this thesis, the use of enzymatic racemization was investigated to overcome yield limitations of preferential crystallization. To support quantitative design a simplified mathematical model capable of describing the essential features of batch preferential crystallization was proposed. The process was studied for the resolution of the chiral amino acid asparagine. The present work investigates the use of an immobilized amino acid racemase (EC 5.1.1.10) to assist chiral resolution by PC.

The kinetic behavior of the enzyme was studied in both soluble and immobilized form. A column reactor packed with the immobilized racemase was evaluated under coupling conditions. The enantiomeric excess was identified as an important constraint for the coupling: PC generates small differences in the concentrations of the two enantiomers, limiting the driving force for the reaction. This challenge can be counterbalanced by increasing the dosage of the stable biocatalyst and by guaranteeing its reusability via enzyme immobilization. A new shortcut model (SCM) was developed to estimate performance indicators of PC. The reduced mathematical framework is composed of only three differential equations requiring three experiments for parametrization. The relatively simple SCM provides significant information during early stages of process development

without the need for applying more detailed population balance equations. The model prioritizes relative simplicity for overall estimation of process productivity at the expense of no precise information of particle size distribution and of accepting deviations beyond strict purity specifications. A detailed experimental study to validate the model is demonstrated. The crystallization parameters and kinetics of the amino acid racemase determined experimentally were used in the SCM to evaluate improvements in performance of PC coupled with enzymatic racemization for the production of pure L-asparagine monohydrate.

The results and tools reported in this work are seen as valuable contributions for more rapid performance assessment of preferential crystallization and for further development of combinations of PC with enzymatic racemization. Other purification processes may profit from the immobilized amino acid racemase characterized and successfully applied. The SCM is flexible to be adapted to other PC configurations and it is seen as advantageous for comparing PC with competing resolution techniques. This work contributes to a better understanding of coupling PC and racemization, promotes application of preferential crystallization and supports the design of more efficient and robust enantioselective crystallization processes.

## Kurzfassung

Enantiomere sind Paare identischer chiraler Moleküle mit unterschiedlichen räumlichen Strukturen. Sie besitzen identische physikalische und chemische Eigenschaften, interagieren in biologischen Organismen jedoch unterschiedlich. Bei chiralen pharmazeutisch aktiven Substanzen weichen beide Enantiomere häufig erhebliche in ihrer therapeutischen und toxikologischen Wirkung voneinander ab. Aus diesem Grund fordern Regulierungsbehörden die Bereitstellung enantiomerenreiner Substanzen. Somit müssen als 50:50 Mischung erzeugte Enantiomere im Anschluss getrennt werden. Bevorzugte Kristallisation ist eine leistungsstarke und kostengünstige Technik zur Auftrennung einer bestimmten Klasse chiraler Moleküle namens Konglomerate. Für Simulationsstudien dieses Trennverfahren stehen komplexe detaillierte Prozessmodelle zur Verfügung. Einfache mathematische Modelle für Analyse von Produktivität im frühen Prozessdesign sind jedoch rar. Ein weiterer Nachteil bei der Trennung von racemischen Mischungen ist die auf 50% beschränkte Ausbeute. Durch die Kombination der Kristallisation mit Racemisierung steigt die theoretische Ausbeute auf 100%. Die Racemisierung kann von unter milden Bedingungen aktiven Enzymen katalysiert werden.

In dieser Arbeit werden die Verwendung von enzymatischer Racemisierung zur Erhöhung der Kristallisationsausbeute ausgearbeitet und ein vereinfachtes mathematisches Modell vorgestellt, welches die bevorzugte Kristallisation im Batch-Prozess quantitativ beschreibt. Als Modellsystem dienen die Enantiomere der chiralen Aminosäure Asparagin in Kombination mit einer Aminosäure-Racemase (EC 5.1.1.10).

Das kinetische Verhalten der Racemase wurde sowohl im ungebundenen als auch im immobilisierten Zustand untersucht. Die immobilisierte Racemase wurde als Festbettreaktor unter geeigneten Kopplungsbedingungen eingesetzt und bewertet. Das Maß des Enantiomerenüberschusses wurde als entscheidender Faktor bei der Kopplung identifiziert, da die bevorzugte Kristallisation nur kleine Konzentrationsunterschiede zwischen den Enantiomeren erzeugt, was die Triebkraft für die Reaktion einschränkt. Bei der Dosierung der stabilen und wiederverwendbaren immobilisierten Racemase könnte diese Anforderungen der Teilprozesse angepasst werden. Eine neuentwickelte vereinfachte Berechnungsmethode (Short Cut Model, SCM) zur Abschätzung von Leistungsindikatoren

der bevorzugten Kristallisation wurde entwickelt und validiert. Kern des Modells sind lediglich drei gewöhnliche Differentialgleichungen, für deren Parametrisierung drei Experimente erforderlich sind. Das SCM liefert in frühen Stadien der Prozessentwicklung wichtige Informationen ohne die Notwendigkeit aufwendigere Populationsbilanzen lösen zu müssen. Das Modell verzichtet dabei auf eine präzise Kristallgrößenbetrachtung und akzeptiert Abweichungen von strengen Reinheitskriterien zu Gunsten einer schnell zugänglichen Produktivitätsprognose. Eine experimentelle Studie zur Validierung des Modells wird für die Enantiomeren von Asparagin demonstriert. Die experimentell bestimmten Parameter zur Beschreibung der Kristallisation und der Kinetik der Aminosäure-Racemase wurden im verwendet, um Abschätzungen zur Leistungssteigerung des gekoppelten Modellprozesses für die Produktion von optisch reinem L-Asparagin-Monohydrat vorzunehmen.

Die vorliegende Arbeit leistet einen Beitrag zur schnelleren Leistungsbewertung der bevorzugter Kristallisation und für die weitere Entwicklung der Racemattrennung in Verbindung mit enzymatischer Racemisierung. Andere entantioselektive Trennverfahren können von der hier vorgestellten immobilisierten Aminosäure-Racemase profitieren. Das SCM kann an weitere Betriebsweisen angepasst werden und bildet eine wertvolle Grundlage für den quantitativen Vergleich mit anderen Trennprozessen. Diese Arbeit trägt zum besseren Verständnis der Kopplung von bevorzugter Kristallisation und Racemisierung bei, fordert zum breiteren Einsatz der bevorzugten Kristallisation auf und trägt somit zum Design effizienterer und robusterer Kristallisationsprozesse zur Enantiomerentrennung bei.

# Contents

<b>Abstract</b> .....	<b>iii</b>
<b>Kurzfassung</b> .....	<b>v</b>
<b>Contents</b> .....	<b>vii</b>
<b>Nomenclature</b> .....	<b>x</b>
<b>1 Introduction</b> .....	<b>1</b>
1.1 Motivation .....	1
1.2 Aim and outline of the thesis.....	4
<b>2 Fundamentals of Crystallization and Preferential Crystallization</b> .....	<b>7</b>
2.1 Thermodynamics of crystallization .....	7
2.1.1 Phase diagrams .....	10
2.2 Kinetics of crystallization.....	12
2.2.1 Nucleation.....	12
2.2.2 Crystal growth .....	14
2.3 Preferential Crystallization.....	16
2.3.1 Preferential Crystallization and racemization.....	21
2.3.2 Driving force calculations in the TPD.....	23
2.3.3 Modeling of Preferential Crystallization .....	25
<b>3 Fundamentals of Enzymatic Racemization</b> .....	<b>33</b>
3.1 Biocatalysis .....	33
3.1.1 Production of recombinant proteins.....	35
3.1.2 Purification .....	37
3.1.3 Immobilization of enzymes .....	39
3.2 Racemases .....	42
3.3 Enzyme kinetics.....	44
3.3.1 Reversible-3-step mechanism.....	47
3.3.2 Inhibition effects.....	51
3.4 Types of enzymatic batch reactor.....	52
3.4.1 Stirred tank reactor .....	52
3.4.2 Packed bed reactor.....	53
<b>4 Experimental Section</b> .....	<b>55</b>
4.1 Model system .....	55
4.1.1 Asparagine monohydrate .....	55

---

4.1.2	Amino acid racemase.....	57
4.2	Materials.....	58
4.2.1	Reagents and immobilization supports.....	58
4.2.2	Buffers.....	59
4.3	Preferential Crystallization setup and procedures.....	59
4.4	Overexpression of amino acid racemase.....	60
4.5	Purification of amino acid racemase.....	62
4.6	Immobilization of amino acid racemase.....	63
4.7	Enzyme activity.....	66
4.7.1	Activity assay of free protein.....	66
4.7.2	Kinetics of free AAR.....	67
4.7.3	Activity assay of immobilized AAR.....	67
4.8	Recycling of immobilized AAR.....	67
4.9	Kinetics of immobilized AAR in batch reactor.....	68
4.10	Steady-state racemization in packed bed reactor.....	68
4.11	Analytics.....	69
4.11.1	Chromatography analysis.....	69
4.11.2	Protein quantification.....	70
<b>5</b>	<b>Characterization and Application of an Enzymatic Reactor.....</b>	<b>71</b>
5.1	Kinetics of free enzyme.....	71
5.1.1	Influence of reaction parameters.....	73
5.2	Immobilization of AAR.....	75
5.2.1	AAR immobilization from crude extract on affinity binding supports.....	75
5.2.2	AAR immobilization from purified enzyme on covalent binding supports.....	77
5.3	Stability of immobilized AAR.....	79
5.4	Kinetics of immobilized enzyme.....	82
5.5	Application in packed bed reactor.....	83
5.6	Outlook for the coupling of PC and racemization.....	85
<b>6</b>	<b>Development and Application of a Shortcut Model for Preferential Crystallization ....</b>	<b>90</b>
6.1	Model assumptions.....	91
6.2	Formulation of mass balances and initial conditions.....	93
6.3	Calculation of driving forces.....	96
6.4	Experimental assessment of the SCM.....	98
6.5	Performance criteria for process evaluation.....	99
6.6	Illustration of the potential of the SCM.....	100
6.7	General strategy to implement the SCM.....	101

---

6.7.1	Calculation of SCM parameters.....	103
6.8	Experimental evaluation.....	107
6.8.1	Determination of model parameters .....	108
6.8.2	Model validation.....	110
6.8.3	Influence of crystallization temperature on SCM parameters .....	111
6.8.4	Process performance: evaluation of productivity .....	112
6.9	Coupling Preferential Crystallization and enzymatic racemization .....	114
6.9.1	Process variant 1: one-unit configuration .....	115
6.9.2	Process variant 2: two-unit configuration.....	117
6.10	Results of performance assessment of coupled process .....	118
6.11	Summary and outlook.....	121
<b>7</b>	<b>Concluding Remarks.....</b>	<b>124</b>
	<b>References .....</b>	<b>128</b>
	<b>Appendix .....</b>	<b>138</b>
A.1	Coordinate transformation.....	138
A.2	List of variables for simulations .....	140
	<b>List of Contributions .....</b>	<b>141</b>

# Nomenclature

## Abbreviations

AA	amino acid
AAR	amino acid racemase
Asn	asparagine
BPD	binary phase diagram
IMAC	immobilized metal ion affinity chromatography
KPI	key performance indicator
MSZ	metastable zone
PBE	population balance equations
PBR	packed bed reactor
PC	preferential crystallization
RBR	rotating bed reactor
SCM	shortcut model
STR	stirred tank reactor
TCID	temperature cycling induced deracemization
TPD	ternary phase diagram

## Latin letters

$a_k$	parameter of $k^{eff}(S^0)$ correlation	[g h <sup>-1</sup> cm <sup>-2</sup> ]
$a_{k,T}$	parameter of $k^{eff}(S^0, T)$ correlation	[g h <sup>-1</sup> cm <sup>-2</sup> ]
$a_t$	parameter of $t_{stop}$ correlation	[h]
$A$	sectional area	[cm <sup>2</sup> ]
$b_k$	parameter of correlation of $k^{eff}(S^0)$	[-]
$b_{k,T}$	parameter of correlation of $k^{eff}(S^0, T)$	[-]
$b_t$	parameter of correlation of $t_{stop}$	[-]
$B$	PBE nucleation rate	[# h <sup>-1</sup> ]
$c$	molar concentration	[mol L <sup>-1</sup> ]
$c_k$	parameter of $k^{eff}(S^0)$ correlation	[-]

$c_{k,T}$	parameter of $k^{eff}(S^0, T)$ correlation	[-]
$D_c$	catalyst dosage	[g L <sup>-1</sup> ]
$ee$	enantiomeric excess	[-]
$E^{eff}$	effective activation energy	[kJ mol <sup>-1</sup> ]
$E_1$	target enantiomer (reaction mechanism)	
$E_2$	counter enantiomer (reaction mechanism)	
$f$	number density function	[# cm <sup>-1</sup> ]
$F_2$	counter enantiomer contamination factor	[-]
$G$	PBE growth rate	[cm h <sup>-1</sup> ]
$\overline{GB}^{eff}$	effective overall mass transfer rate	[g h <sup>-1</sup> ]
$k^{eff}$	effective crystallization rate constant, SCM parameter	[g h <sup>-1</sup> cm <sup>-2</sup> ]
$k_{pol}$	calibration parameter of polarimeter	[g g <sup>-1</sup> deg <sup>-1</sup> ]
$K_I$	inhibition constant	[mol L <sup>-1</sup> ]
$K_M$	Michaelis constant	[mol L <sup>-1</sup> ]
$L$	coordinate of particles in PBE	[cm]
$m$	mass	[g]
$m_{seeds}$	mass of seed crystals	[g]
$m_{S_{max}}$	maximum theoretical mass of solid product	[g]
$m_{tot}$	total mass of liquid phase	[g]
$M$	molar mass	[g mol <sup>-1</sup> ]
$n^{eff}$	effective order of crystallization kinetics	[-]
$N$	number of particles (SCM)	[#]
$OF$	objective function	[-]
$Pr$	productivity	[g h <sup>-1</sup> L <sup>-1</sup> ]
$Pu$	purity	[-]
$Q_R$	mass flow rate	[g h <sup>-1</sup> ]
$r$	reaction rate	[mol min <sup>-1</sup> L <sup>-1</sup> ]
$R$	radius of particles	[cm]
$R_G$	universal gas constant	[J mol <sup>-1</sup> K <sup>-1</sup> ]
$S$	supersaturation	[-]
$t$	time	[h]
$t_{dead}$	dead time or idle time during PC process	[h]
$t_{stop}$	stop time, SCM parameter	[h]
$T$	temperature	[°C]

$u$	velocity	[cm min <sup>-1</sup> ]
$V$	volume	[cm <sup>3</sup> ]
$\dot{V}$	volumetric flow rate	[ml min <sup>-1</sup> ]
$V_{max}$	maximum reaction rate parameter	[mol L <sup>-1</sup> min <sup>-1</sup> ]
$w$	mass fraction	[g g <sup>-1</sup> ]
$w_{sat}$	equilibrium mass fraction	[g g <sup>-1</sup> ]
$w_{ratio}$	solubility ratio	[-]
$X_P$	Cartesian coordinate of point P	[-]
$Y_P$	Cartesian coordinate of point P	[-]
$Y$	process yield	[-]
$Y_{im}$	immobilization yield	[-]
$z$	length	[cm]

### Greek Letters

$\alpha$	optical rotation	[deg]
$\varepsilon$	porosity	[-]
$\nu$	stoichiometric coefficient	[-]
$\rho$	density	[g cm <sup>-3</sup> ]
$\tau$	residence time	[min]

### Subscripts

1	target enantiomer
2	counter enantiomer
3	solvent
C	crystallizer
<i>cryst</i>	crystallization
<i>exp</i>	experimental
<i>i</i>	index of target and counter enantiomers (1, 2) or solvent (3)
<i>j</i>	index of iteration of $k^{eff}$ optimization
<i>L</i>	liquid phase
<i>max</i>	maximum

---

<i>pol</i>	polarimeter
<i>R</i>	racemization reaction or reactor
<i>S</i>	solid phase
<i>sat</i>	saturation
<i>sim</i>	simulated
<i>tot</i>	total

### Superscripts

0	initial condition
eff	effective



# 1 Introduction

## 1.1 Motivation

Every living organism has the ability to distinguish chiral molecules and react differently to each enantiomer of a pair. While one enantiomer is the desired active pharmaceutical ingredient (API), its antipode might be inactive, cause side effects or be toxic (Ali, 2007). This fact has been acknowledged since many decades and it became of extreme importance in pharmaceutical and fine chemical industries (Lorenz & Seidel-Morgenstern, 2014). Particularly after the changes in guidelines for chiral drugs of the regulatory agencies, there has been a strong augmentation of the research and industrial production of pure chiral compounds. New drugs are developed as single enantiomers and existing chemicals have been re-launched in pure form (Calcaterra & D'Acquarica, 2018).

Pure enantiomers can be obtained via two main paths: chiral approach and racemic approach (Lorenz & Seidel-Morgenstern, 2014). In the first route, optically pure molecules are directly synthesized for instance via selective metabolism during fermentation, or by stereoselective catalysis. This method is attractive, but often cannot provide required purity and it lacks attributes to address more general solutions. Consequently, a great effort has been done in developing techniques from the racemic approach (Femmer et al., 2016). The enantiomers are produced as racemic mixtures and further resolved via one or a combination of chiral separation techniques (Lorenz & Seidel-Morgenstern, 2020).

Different optical resolutions might be suitable depending on the type of crystalline racemate of the target substance. There are three known crystallization behaviors, which are based on the binary melting point phase diagrams (Jacques et al., 1994; Roozeboom, 1899): conglomerates, racemic compounds and solid solutions (Figure 1.1). Solid racemates from conglomerate-forming systems are a mechanical mixture of both optical isomers. Racemic compounds produce a stable solid phase holding equal amounts of the two enantiomers in the crystal lattice. More rarely, solid solutions (or pseudoracemates) form of a crystal lattice consisting of both enantiomers in a random fashion.

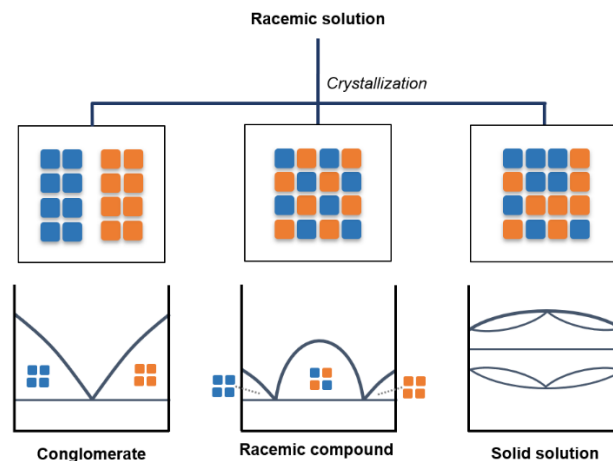


**Figure 1.1** Types of crystalline racemate of enantiomers and their respective binary phase diagrams (first described by Roozeboom (1899)).

Preferential crystallization (PC) is an attractive method for resolution of conglomerates (Coquerel, 2006). It is commonly less expensive than other techniques, for instance, chromatography, and it generates solid product, which is frequently the desired form in the industry. PC is performed by seeding a supersaturated racemic solution with the target enantiomer. This crystallization method is a kinetically driven process, so it must be carefully designed to avoid spontaneous nucleation of the non-seeded enantiomer.

An important challenge of preferential crystallization is the 50% yield limitation. This is a consequence of the racemic feed, since only half the solution composition comprises the target molecule. Combining PC with racemization of the non-target enantiomer is an attractive solution to overcome this limitation (Yoshioka, 2006) (see Figure 1.2). In addition to increasing the maximum yield and recycling the undesired molecule, this process coupling is advantageous because it secures product purity by alleviating supersaturation of counter enantiomer. This results in an increase in productivity (Würges et al., 2009a). To effectively improve the chiral resolution, the ideal racemization rate would be extremely fast, having no limiting values. In reality, high velocities of conversion are achieved by an efficient catalyst, as well by the application of high amounts of catalyst. The use of relatively large catalyst dosage is limited by economical aspects. Enzymes have been explored as catalysts in combination with PC only in soluble form (Fuereder et al., 2016; Würges et al., 2009a). Enzyme immobilization provides recyclability, stabilization, and easy separation from reaction media (Rodrigues et al., 2013; Sheldon & van Pelt, 2013). It also allows the application on enzymes in fix bed reactors,

which have already been effectively employed in combination with chromatography (Wrzosek et al., 2018), but so far have not been used for the improvement of preferential crystallization.

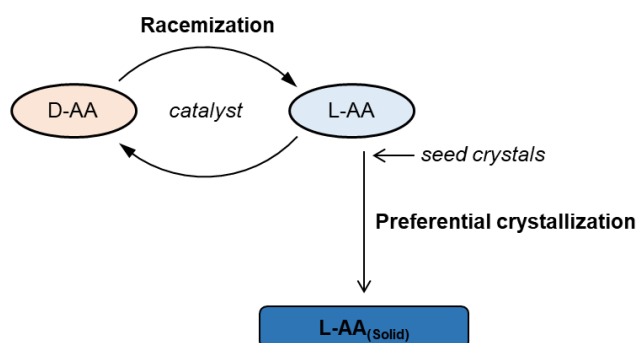


**Figure 1.2** Schematic combination of preferential crystallization and enzymatic racemization. The starting solution is supersaturated racemic mixture. The L-amino acid (L-AA) is the target enantiomer. Excess of D-amino acid (D-AA) is racemized into L-AA by a catalyst.

Successful design of crystallization processes is based on the evaluation of key performance indicators (KPIs) such as productivity, product purity and yield, which are not sufficiently reported in the existing literature in the field (Koellges & Vetter, 2018). In order to validate process feasibility and robustness, KPIs must be evaluated since early stages of the process development. Estimation of performance KPIs give a better understanding of the influence of operating conditions. They also help choosing the most efficient technique and process configuration for manufacturing. Simulations of preferential crystallization are achieved by population balance models (Ramkrishna, 2000). These models are efficient and highly valuable for the estimation of a detailed crystal size distribution at every discrete time instant. The prediction and control of particle size and shape are essential when handling solid populations. However, population balance models require time-consuming theoretical and practical work due to the use of discretization methods, as well as a significant number of experiments for parameter estimation. Such a comprehensive dynamic description of the solid population might not be needed during early process design. At this stage, the main objective is often to explore the overall performance of the resolution technique. This issue has not yet been addressed and there is a lack of simple tools to facilitate the assessment of performance KPIs in early design of preferential crystallization.

## 1.2 Aim and outline of the thesis

To address the challenges in process design and limited yield, the current study focuses on advances in performance of batch preferential crystallization for the production of pure enantiomers. In this context, the main goals are to investigate the potential of immobilized enzymes to improve preferential crystallization and to develop a model to efficiently estimate key performance parameters of PC.

The design of a racemization unit to improve preferential crystallization was investigated. The aim was to provide an effective bioreactor to be combined with chiral resolution of asparagine enantiomers. So far, a proof of concept had been reported for the combination of PC with *in situ* racemization using free soluble amino acid racemase (AAR) E.C. 5.1.1.10 from *Pseudomonas putida* KT2440 (Würges et al., 2009a). In the present work, a poly Histidine-tag was added to that enzyme to facilitate its purification. In order to obtain a stable and reusable catalyst, immobilization of the AAR was tested on various affinity and covalent binding supports. The optimization criteria evaluated for enzyme immobilization were specific activity and reusability of the immobilized enzyme. The performance of the enzyme in a packed bed reactor was exploited.

A novel simplified model was proposed to tackle the issue of rapidly assessing performance parameters of preferential crystallization. The *Shortcut Model* (SCM) is capable of describing the first stage of batch PC, which is the most relevant due to product purity constrains. Only two ordinary differential equations are needed, both originating from the mass balance of the target enantiomer in the liquid and solid phases. The model application is extended to solvate-crystal systems by adding a third equation for the mass balance of the solvent. Compared to population balance models, the SCM neglects the size distribution and focus on the total mass exchange between phases. The foundation of that is the assumption that all crystals are of similar increasing size and shape. An experimental demonstration of the model is presented for the enantiomers of the amino acid asparagine monohydrate. The SCM is extended to comprise the simulations of the coupling of PC and racemization.

Following this introduction, first the concepts necessary for the development of the present work are provided in more detail. Essential features regarding thermodynamic and kinetic aspects of crystallization are described in **Chapter 2**. It is in this chapter that

principles of preferential crystallization are presented, together with a literature overview of its integration with a racemization step. The methodology for calculation of crystallization driving forces and modelling of PC using population balance equations are then given.

To introduce the necessary concepts on enzymatic racemization, a brief overview on biocatalysis is given in **Chapter 3**. These general concepts are followed by important aspects on the production, purification and immobilization of recombinant enzymes. Finally, the typical mathematical description of enzymatic kinetics is given for a simple Michaelis-Menten approach and for a broader reversible mechanism. These models are key for the description of enzyme activity and for its characterization.

In **Chapter 4**, first the model substance and model enzyme are presented, followed by the materials including main reagents, immobilization supports and a table of buffer solutions used during experiments with the racemase. The methodology used during all experimental investigations of preferential crystallization and related to the enzyme are presented. Details of the amino acid racemase overexpression and purification will be given in this chapter.

Results of systematic investigations regarding the amino acid racemase are presented in **Chapter 5**. The sections elucidate the experimental results of reaction kinetics, the evaluation of reaction parameters such as dosage and enantiomeric excess, development of the immobilization strategy in affinity and covalent binding supports and characterization of the immobilized amino acid racemase in tank and fix bed reactor. The final part is dedicated to insights of the combination of preferential crystallization and enzymatic racemization, suggesting benefits and challenges of this coupling.

In **Chapter 6**, a new shortcut model is developed as a tool for rapid first evaluation of the productivity of preferential crystallization. The principles underlying the development of the model is described in the first section, along with the model assumptions. The description of model equations is then given, followed by an algorithm for calculation of the saturation mass fractions. Quantification of experimental assessment and process evaluation, such as productivity, yield and purity are specified. Next, an approach for application of the model and for parameter estimation is proposed. Experimental results of preferential crystallization of asparagine monohydrate enantiomers

are applied to parametrize the SCM and estimate productivity following the strategy suggested. The final section is dedicated to show the coupling of PC and enzymatic racemization modeled by the SCM in two different process variants and to discuss simulation results of productivity and yield for the resolution of asparagine enantiomers.

**Chapter 7** summarizes the main results and gives concluding remarks.

## 2 Fundamentals of Crystallization and Preferential Crystallization

Crystallization is an important technology in chemical and life-science industries for separation and purification purposes (Lorenz & Seidel-Morgenstern, 2020). It has a broad range of industrial applications in the pharmaceutical, food and fine chemicals industries. It is employed in a variety of scales: for instance, for the production of a few kilograms of high-added-value drugs, or for the provision of millions of tons per year of salt, sucrose and fertilizers (Tavare & Tavare, 1995). Crystallizing systems comprise the transfer of one or more substances from a continuous phase, which is most often in liquid form, but can also be in gaseous or amorphous solid state, to a crystalline solid form.

Crystallization can be successfully applied to separate enantiomers. For systems crystallizing as conglomerates, the resolution can be held by means of preferential crystallization, diastereomeric resolution or deracemization techniques.

In the present chapter, the foundations necessary to comprehend enantioselective resolution via crystallization are briefly reviewed. First, the essential thermodynamic features of the process are presented, i.e. supersaturation, metastable zone limits and phase diagrams. In sequence, the role of nucleation and growth are introduced as the kinetic aspects involved in crystallization. The principle and recent advances in preferential crystallization are discussed, followed by a brief review of the developments of its coupling with racemization. A summary of the alternative methods to separate conglomerate enantiomers are also given. The calculation of driving forces necessary for PC this process are illustrated for conglomerate-forming systems. Finally, there is an overview of the typical mathematical description of PC using population balance equations.

### 2.1 Thermodynamics of crystallization

A saturated solution, which is composed of solvent and solute, is in thermodynamic equilibrium with a solid phase at a given temperature. If excess of dissolved solute is present, the system is metastable and it is called *supersaturated*. Then, crystallization takes place in order to deplete supersaturation and to bring the system to an equilibrium state. Supersaturation

can be described by the dimensionless ratio between the concentration in solution  $w_i$  of component  $i$  and the saturation concentration  $w_{sat,i}$ :

$$S_i = \frac{w_i}{w_{sat,i}} \quad i = 1,2 \quad (2.1)$$

For a pair of enantiomers,  $i = 1$  is defined in this work as the target molecule and  $i = 2$  as the counter enantiomer. The solvent is described by index  $i = 3$ . The quantity  $w_{sat,i}$  is the liquid phase mass fraction under equilibrium conditions. If  $S < 1$ , the system is unsaturated; if  $S > 1$ , the system is considered supersaturated. Hereby, concentrations were expressed in weight fractions relative to the total mass of the liquid phase  $m_{tot} = m_1 + m_2 + m_3$ :

$$w_i = \frac{m_i}{m_{tot}} \quad i = 1,2 \quad (2.2)$$

The concentrations calculated by equation 2.2 may be given as a mass ratio (e.g. g/g) or as weight percent, for instance in grams of solute per 100 grams of solution (wt%). From the mass balance, the sum of mass fractions of all  $N$  solute components in a system is equal to the unit, as showed below:

$$\sum_{i=1}^N w_i = 1 \quad i = 1,2 \quad (2.3)$$

For a mixture of enantiomers,  $N = 2$ . The main parameters which can influence the level of supersaturation of a system are temperature, composition and solvent or solvent mixture. These variables play an important role on the design of a crystallization process. They define the main methods to create supersaturation (Myerson, 2002), which are:

- i) Changing temperature, either cooling or heating, depending on the behavior of the solubility curve;
- ii) Changing concentration of the solution, which can be achieved for instance by solvent evaporation;
- iii) Adding an anti-solvent, namely drowning-out crystallization, that acts by reducing solubility of the solute and causing crystallization.

An alternative way to build up supersaturation is to add an agent that entrains the occurrence of reactions. When the crystallization arises through chemical reaction in a relatively fast manner it is called *precipitation* reaction (Mullin, 2001).

Solubility curves provide a graphical representation of temperature dependency between a solvent (or solvent system) and the maximum dissolved amount of a solute. From these curves it is possible to determine the maximum product yield for a specific change in temperature, as well as the necessary variation in temperature for a desired solid yield. An exemplary solubility diagram is illustrated in Figure 2.1. For most substances solubility increases with temperature, as depicted in the solid blue curve, but it could also decrease or stay constant under temperature changes. To the right hand side of the illustrated solubility curve, the system is stable in a single phase (liquid). Such systems are called *undersaturated*. By decreasing temperature or increasing concentration, the system crosses the solubility curve and becomes supersaturated. This may happen by addition of solute or withdrawal of solvent. The region between the solubility line and the maximum allowable supersaturation without nucleation is called metastable zone (MSZ). The boundary of the MSZ, represented as dashed red curve, bounds the beginning of the unstable region where nucleation can occur spontaneously.

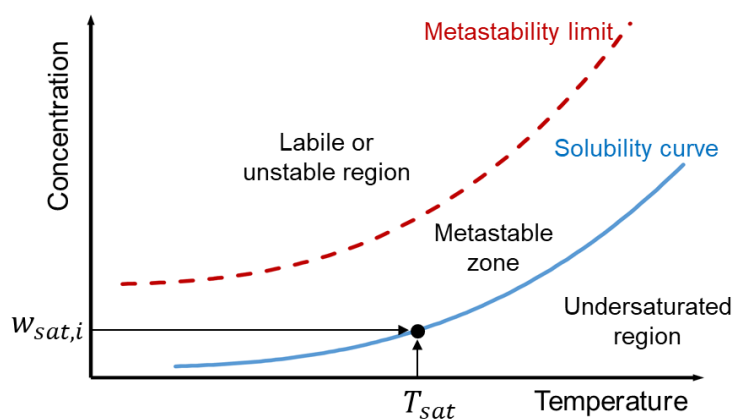


**Figure 2.1** Schematic illustration of solubility diagram. Solubility curve is the temperature-dependent saturation concentration  $w_{sat,i}$  of component  $i$  dissolved in a given solvent. The metastability limit bounds the region where spontaneous nucleation can occur. The area between the two curves in the metastable zone (MSZ).

The width of the MSZ is influenced by the presence of impurities, the cooling rate and also solution history (Mullin, 2001). Understanding this region and how it is affected by process parameters is important for designing of a crystallization unit. On one hand, it is interesting to operate a process far from the solubility line, since high supersaturation values generate more productive results. On the other hand, if the operating area is too close to the metastable limit, primary spontaneous nucleation becomes difficult to control. In the industry, typical values of supersaturation lay around 30% of the MSZ (Lorenz et al., 2006a).

Despite great advances achieved in the field in recent years, it is still difficult to predict solubility of a substance in a desired solvent. Therefore, the equilibrium concentrations  $w_{sat,i}$

at different temperatures should be measured experimentally. Solubility data of a large variety of binary and ternary systems are available in literature, but should be applied with caution for impurities can impact the solubility significantly (Mohan et al., 2002).

### 2.1.1 Phase diagrams

Phase diagrams give a physical representation of the solid-liquid equilibria under various conditions of temperature and composition. Their different areas indicate the existence of one or more phases, each composed by pure substances or mixtures. They can be classified as binary, ternary, or quaternary diagrams, depending on the number of substances present (Lorenz, 2013). A phase diagram of a pair of enantiomers is symmetric around the racemic composition. This is a consequence of their identical melting point and melting enthalpy. Enantiomers are often characterized as binary systems, when only the pairs of chiral isomers is represented, or as ternary systems, for mixtures of the two enantiomers in a solvent.

Melting point phase diagrams or binary phase diagrams (BPD) help distinguishing the types of enantiomers. As shown in Figure 1.1, these stereoisomers are classified as conglomerates, racemic compounds or solid solutions, based on the presence of single or double eutectic points or the existence of miscibility in the solid state. Crystallization may be carried out directly from the melt if the substance is stable at the melting temperature. More frequently, crystallization is performed from solution, and it is necessary to identify an appropriate solvent or solvent system for the process. Ternary phase diagrams (TPD) show the phases and equilibrium compositions of the three components of enantiomers in solution. TPD are used as tools for the design of enantiomeric resolution methods. Similarly to BPD, the types of crystalline racemate are also identified in the TPD. These two phase diagrams are interconnected, and the solubility isotherms in TPD are related to the liquidus curve from the melting phase diagrams.

Ternary mixtures in a TPD are commonly represented in equilateral triangles, as illustrated in Figure 2.2 for the three types of crystalline phases: (a) conglomerates, (b) racemic compound forming systems and (c) solid solutions. Each vertex represents a pure substance (enantiomers 1 and 2 and solvent 3). The lateral lines of the triangle are the binary mixtures (1-3 and 2-3 are the mixtures of each enantiomer and the solvent and 1-2 is the mixture of both enantiomers) and any point inside of the diagram represents a ternary mixture. Weight fractions  $w_i$  are characterized along the triangle sides. The composition of any point of the TPD can be found by drawing lines parallel to these sides. The resulting total composition of a mixture of

any two points inside the TPD is always on the straight line connecting these points. This characteristic is particularly valuable to assess the composition of each phase of a mixture located in an area where more than one phase exists. A complete description of the construction of ternary phase diagrams is given by Jacques, Collet and Wilen (Jacques et al., 1994).

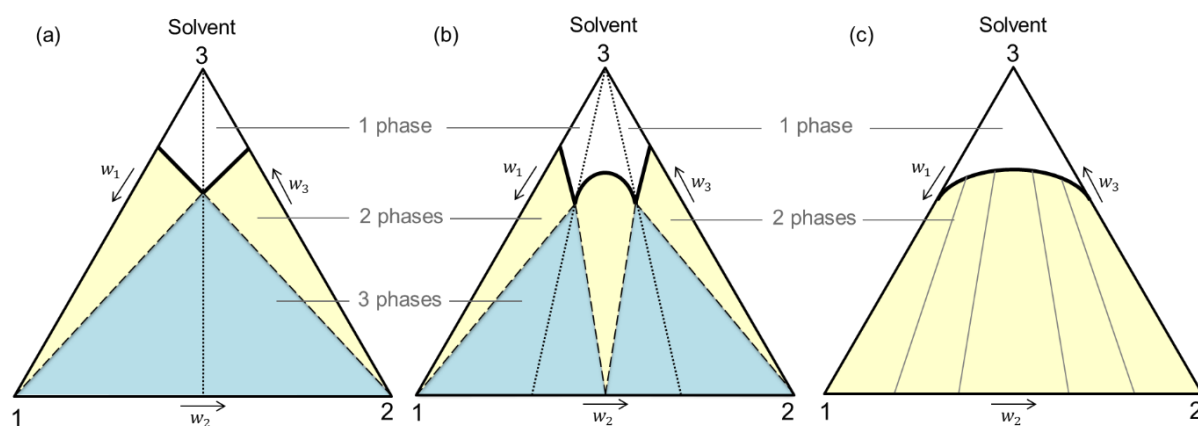


**Figure 2.2** Ternary phase diagrams illustrated for a (a) conglomerate, (b) racemic compound and (c) solid solution. Bold curves represent solubility isotherms; dotted lines in (a) and (b) are the eutectic compositions; dashed lines are boundary tie lines limiting number of phases that co-exist. Yellow and blue areas indicate two-phase and three-phase regions, respectively. In (c) the colored area is the two-phase region, with the respective compositions found along the tie-lines.

The different regions with respective number of phases are delimited in the TPD (Figure 2.2) by the solubility curves (black bold curves) and the tie-lines (dashed lines) connecting the eutectic composition to the pure enantiomers 1 and 2 (in panels (a) and (b)) and to the racemic compound (in panel (b)). Above the isotherm is the one-phase region, where all components are dissolved in an unsaturated solution. The number of regions below the solubility isotherm depends on the type of enantiomeric system. Conglomerates have two regions containing two phases (solid 1 + liquid and solid 2 + liquid) and one three-phase region (solid 1 + solid 2 + liquid). Racemic compound-forming systems have three two-phase regions (solid 1 + liquid, solid 2 + liquid and solid racemic compound + liquid) and two three phase regions in between. Solid solutions present a single two-phase region. The composition of the solid and liquid phases vary respecting the tie lines.

Important information on equilibrium states can be obtained from ternary phase diagrams, for instance: the theoretical yield of the process, the solid phase(s) that can be produced at certain conditions, the existence of solvates, polymorphs, intermediate compounds or solid solutions. However, not only thermodynamic conditions but also kinetically time-dependent states can be taken from the diagram. The metastable solubility is characterized in the TPD by

prolongations of the solubility isotherms beyond the eutectic compositions (Jacques et al., 1994). This metastable solubility defines a pseudoequilibrium state which controls the behavior of the system for a certain period of time. As it is described in section 2.3.2, the metastable solubility can be used to graphically calculate supersaturation over time during a crystallization process.

Ternary phase diagrams also provide representation of the relation between the solubility of the pure compounds and that of the eutectic composition. This relation dictates the shape of the solubility isotherms. In particular for conglomerate forming systems, it influences the steepness of the solubility curve, from pure enantiomer to racemic mixture. This affects the size of the metastable zone and has a strong impact on the choice of the resolution strategy. The solubility ratio  $w_{ratio}$  is the relation between the equilibrium composition of the racemic mixture  $w_{rac}$  and that of pure enantiomer  $w_{sat,1}$  at one specific temperature (equation 2.4). For ideal systems, solubility of the racemate is double of solubility of the pure enantiomer and hence  $w_{ratio} = 2$ .

$$w_{ratio} = \frac{w_{rac}}{w_{sat,1}} \quad (2.4)$$

## 2.2 Kinetics of crystallization

The thermodynamic aspects discussed in the previous section are the foundations of a crystallizing system, determining the initial and final state of the process. The path and time required between those two states are nevertheless intrinsic to a particular system and must be as well understood. After achieving supersaturation, by e.g. changing temperature, the system attempts to reach equilibrium through nucleation and growth. These are the two main phenomena involved in the kinetics of crystallization.

### 2.2.1 Nucleation

Nucleation is the genesis of a new phase. The number of molecules that compose a stable nucleus can vary 10 to 1000 molecules. Its formation can occur in very different timespans, ranging from less than a second to days (Chen et al., 2011). Depending on the conditions of nuclei formation, nucleation is typically categorized according to the following driving mechanisms (Mullin, 2001):

- i) Primary homogeneous nucleation, which occurs spontaneously in the absence of particles;
- ii) Primary heterogeneous nucleation, which is induced by the presence of traces of solid foreign bodies, such as foreign particles or dust;
- iii) Secondary nucleation, which takes place the presence of solute crystals.

For homogeneous nucleation to arise in a clear solution, a free-energy barrier must be passed. This formation of a new phase is described by classical nucleation theory, which started to be established based on the work of Volmer (1939) and Gibbs (1879). According to that theory, a cluster is formed by successive random addition of cluster-units. The resultant free energy of a cluster depends on its size  $L$  and it is equal to the sum of the positive free energy for the formation of nuclei surface  $\Delta G_a$  and the negative free energy for phase transformation, or volume-free energy  $\Delta G_v$  (see Figure 2.3). At the highest energy barrier level, the clusters reach a critical size  $L_c$  and form stable crystal nuclei. For cluster sizes below  $L_c$  the equilibrium tends towards the disintegration of the nucleus. Beyond the critical size, the nuclei free enthalpy decreases and the particles grow spontaneously.

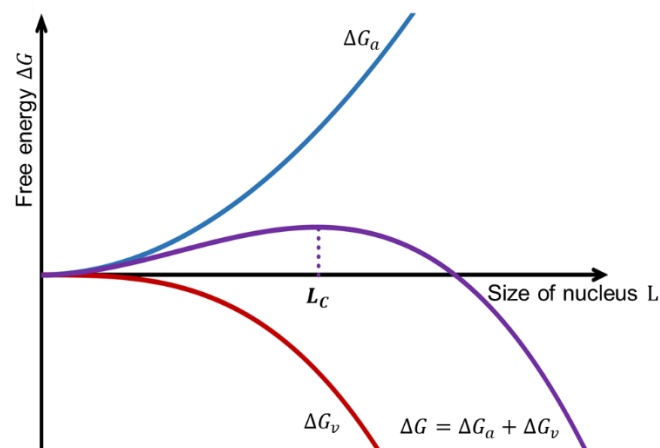


**Figure 2.3** Free energy diagram for primary nucleation. Illustration of the energy barrier required to reach the critical cluster size  $L_c$ .

Primary heterogeneous nucleation requires lower energy levels compared to homogeneous systems. The impurities present in a heterogeneous system are believed to facilitate nucleation by reducing the energetic demand for the cluster surface formation and, hence, by decreasing  $\Delta G_a$ . As a result, the supersaturation required for heterogeneous nucleation is also lower than that in a clear solution.

Secondary nucleation also occurs at lower supersaturation levels than primary homogeneous nucleation. This happens because preexisting crystals of the solute catalyze the generation of clusters. According to different theories, secondary nuclei can be a result of several mechanisms. For instance, they can originate directly on the surface of seeded solute crystals, from the collision of these particles with the environment, or from concentration gradients induced by the particles. The rate of secondary nucleation is affected, for example, by supersaturation, presence of impurities, cooling rate and degree of agitation (Myerson, 2002).

According to the classical theory, nucleation arises instantly once the system is supersaturated. In practice, there is a period of time elapsing before appearance of nuclei, called *induction time*  $t_{ind}$ . This quantity is intrinsically related to the metastable zone width (described in the previous section). The induction time is determined experimentally by the sum of the actual time required to form critical sized nuclei and the time for them to grow to a detectable size (Mersmann, 2001).

### 2.2.2 Crystal growth

The second phenomenon that contributes to crystallization is crystal growth. Classical growth theories are based on the assumption that solute species integrate into the crystal lattice surface. Several of those theories were developed from the elucidation of characteristics of the solid phase, such as crystal morphology, presence of dislocations, or surface energy (Mullin, 2001). Among the classical concepts, the diffusion-reaction theories can describe overall growth kinetics in bulk crystallization (Nernst, 1904; Noyes & Whitney, 1897). They assume that the growth process is divided into the following steps: (i) transport of solute from the bulk to the crystal surface and (ii) incorporation of the molecule on the crystal surface. For the crystal growth of component  $i$ , The combination of these two stages can be presented by the power law below:

$$\frac{dm_{S_i}}{dt} = K_{G_i} A_i (c_i - c_{sat,i})^{g_i} \quad i = 1,2 \quad (2.5)$$

In the equation above, the changes in solid mass  $m_{S_i}$  over time are a result of the product of an overall crystal growth rate coefficient of component  $i$ , namely  $K_{G_i}$ , the crystal surface area  $A_i$  and the driving force of order  $g_i$  generated by supersaturation. The quantity  $c_i$  is the concentration of solute  $i$  in the bulk solution and  $c_{sat,i}$  is the saturation concentration at equilibrium conditions.

If the surface integration step is the limiting resistance to the crystallization process, it can be assumed that the growth rate is dependent exclusively on supersaturation. On that scenario, McCabe (1929) proposed that geometrically similar crystals of the same material suspended in the same solution grow at the same rate  $G$  if the growth is measured as the increase in length  $L$ . The corresponding linear rate expression can be written for a component  $i$ :

$$G_i = \frac{dL_i}{dt} \quad i = 1,2 \quad (2.6)$$

For this expression to be valid, it is assumed that particles of different sizes have similar solubility and crystals retain similar geometry during the process (Canning & Randolph, 1967). Therefore, the McCabe's law implies that the growth rate is constant for all particles sizes. This assumption is used in section 2.3.3 to describe population balance equations for preferential crystallization. However, it is well known that this is a simplification and it might not be valid for every system. Two main approaches are applied to extend that proposition: (I) size-dependent growth and (II) crystal growth dispersion. Approach I describes growth as a monotonic function of the particle size. Crystals of the same size exposed to the same conditions grow at the same rate. On the other hand, in approach II, particles of similar size may exhibit different growth rates. Growth is described as a probability distribution, and a range of growth rates are attributed to a population of particles (Ulrich, 1989). The distributions in crystal growth dispersion can be described by constant crystal growth (CCG) model, common history (CH) model, or growth-diffusivity (GD) model. CCG model assumes that each individual particle has its own inherent growth rate. CH model assumes that all particles from the same seed population or nucleated at the same time under the same conditions have the same "history" and therefore share an inherent growth rate. GD model assumes that all particles of a population have similar growth rate, but it fluctuates randomly around a mean value (Srisanga et al., 2015).

Both approaches I and II have been used to model crystallization systems (Myerson, 2002; Randolph & Larson, 1988). Srisanga and coworkers have presented a comparison between the two model types (Srisanga et al., 2015). They showed that particles grow via a constant mechanism, but with significant amounts of growth dispersion. Crystal growth dispersion was described as the real phenomenon that affects the particulate populations and that can be measured. Size-dependent growth was considered valid only for crystals of size smaller than 1  $\mu\text{m}$ , due to the strong influence of surface energy in the thermodynamic stability of these particles.

Industrial relevant crystallization processes usually concerns bulk crystallization, where many other effects besides supersaturation may affect the process. For instance, presence of impurities, interaction with impellers and walls, breakage, and agglomeration can influence crystal growth (Mullin, 2001). It is easy to understand that ideal conditions assumed in classical crystal growth theories are not always observed. Even though these “classical” concepts provide solid theoretical background and mathematical means for prediction of crystal size and its morphology, empirical models are often used to describe growth rate in bulk crystallization.

More recent theories propose growth mechanisms by aggregation of nucleated crystals in mono- or polycrystalline structures, suggesting that these nuclei behave as colloidal systems (Andreassen & Lewis, 2017). These are promising models, in particular to help understanding the effects of impurities and highly viscous solutions on crystallization. Nevertheless, they are currently not able to provide a mathematical description for prediction of crystallization kinetics.

### **2.3 Preferential Crystallization**

Preferential crystallization (PC) is an important, cost-effective technology for separation and purification of chiral substances. Formerly named resolution by entrainment, PC was first reported by a student of Pasteur in 1866. Back then, the finding did not draw much attention of the scientific community, until it was “rediscovered” in the beginning of the 20<sup>th</sup> century by Werner (Ernst et al., 2011). This powerful technique has been explored by researchers ever since. The most famous industrial example is the production of L-glutamic acid via PC during the 1960s (Jacques et al., 1994). More recent industrial applications comprise, for instance, the resolution of enantiomers of modafinic acid, which is applied in the treatment of sleep disorders, and the enantiomeric purification of omeprazole, used in patients for the treatment of gastroesophageal reflux disease and similar gastric conditions (Levilain & Coquerel, 2010).

The separation of enantiomers by preferential crystallization is only possible because the kinetic aspects of the process have an important influence on crystallization. The ground principle for PC is stereoselective crystallization, which takes place when both enantiomers are supersaturated and should thus crystallize simultaneously. When a supersaturated solution is seeded, it rarely reaches equilibrium immediately. There is an intrinsic lag time for primary nucleation to occur, which is caused by the differences in energetic barrier between nucleation and growth. The energy required to grow the seeded crystals is lower than the one to trigger

spontaneous nucleation. This kinetic advantage allows the crystals of one enantiomer to grow preferentially over the other for a certain period of time.

Preferential crystallization must be performed in the three-phase region of the TPD (see Figure 2.2). For conglomerates (Figure 2.2a), resolution can be achieved starting from a racemic mixture. These substances present a full chiral discrimination in the solid state: each enantiomer forms chiral pure crystals and there is no stable racemic solid phase. Enantioseparation of racemic compounds (Figure 2.2b) by preferential crystallization is also possible. It requires, however, a prior enrichment close to the eutectic composition. That can be achieved, for instance, by chromatography (Lorenz et al., 2006b). The eutectic composition varies according to the substance and solvent system, and it is not necessarily near the 50:50 mixture. For instance, the eutectic composition of mandelic acid in water is around 70 wt% (Lorenz et al., 2002), while for the enantiomers of praziquantel in water the eutectic is found closer to the pure component, at 92 wt% (Liu et al., 2004). In this last example, the TPD presents a large two-phase region around the axis of racemic composition, where the only solid phase that can be crystallized is the racemic compound. The separation of enantiomers of bicalutamide face a similar challenge, for the eutectic composition of this racemic-compound-forming drug in the presence of methanol is 97.7 wt% at 0 °C and 95 wt% at 60°C. Kaemmerer and coworkers successfully investigated a the combination of chromatography and preferential crystallization for the resolution of racemic bicalutamide (Kaemmerer et al., 2012). The first separation process provided the enrichment needed for the crystallization, achieving an overall process productivity of 180 g of product per hour per liter of adsorbent.

To perform isothermal batch PC of a conglomerate, the racemic solution must first be prepared in saturated form (at  $T_{sat}$ ). Then, the solution is cooled down to the crystallization temperature  $T_{cryst}$  in order to reach a desired supersaturation degree. The supersaturation should be high enough to provide good product yield, but it must not surpass the metastable zone limits in order to avoid undesired primary nucleation. Preferential crystallization is initiated by adding homochiral seeds of the target enantiomer to the solution. A graphical illustration of PC is shown in Figure 2.4. The seeded crystals will grow preferentially for the given surface area. The crystallization of the counter enantiomer will be kinetically inhibited for a certain period. Eventually crystals of the non-target molecule crystallize, at the time point nominated in this work as *stop time* (see Chapter 6), and product purity is compromised. If given enough time, the system reaches equilibrium. At this state a racemic liquid phase is present

together with a racemic solid product. The crystals may have a slight excess of target compound because of the initial seeds.

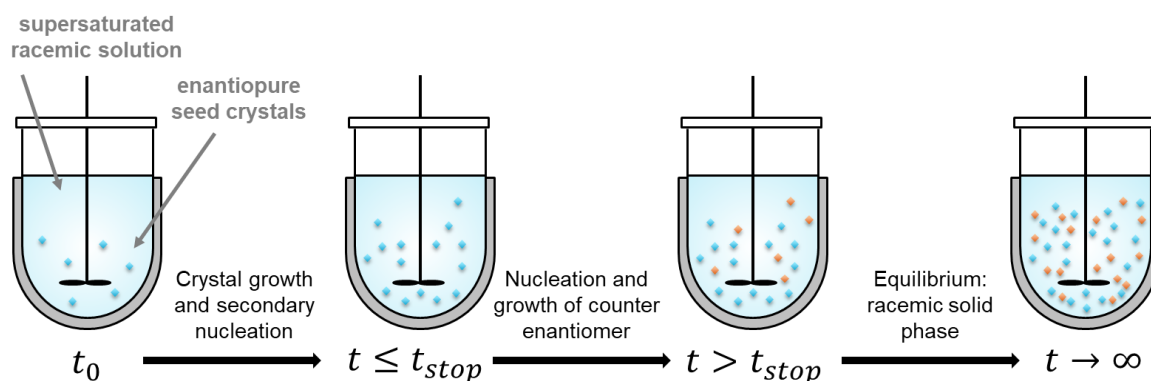


**Figure 2.4** Illustration of the principle of preferential crystallization in isothermal batch mode.

The trajectory followed during preferential crystallization can be represented in the ternary phase diagram. Figure 2.5 depicts a typical process curve of PC. The solid lines  $OT_{cryst}$  and  $MT_{sat}$  are solubility isotherms. The blue curve  $MO$  connecting the initial and final state points illustrates a process trajectory. The metastable solubility limiting preferential crystallization is characterized by the prolongation of the solubility isotherms beyond equilibrium (Jacques et al., 1994), represented in Figure 2.5 by dotted lines. The colored area is the metastable region between the saturation temperature and the crystallization temperature ( $T_{sat} > T_{cryst}$ ). This area defines the operating region where PC can take place. The size of the region is system-dependent. The shape of the isotherms define the size of this operating region. Substances that have a rather large solubility ratio racemic/pure enantiomer (equation 2.4) at the crystallization temperature present steeper solubility isotherms and hence narrower operating regions.

Upon seeding with single chirality particles of enantiomer 1, the solution composition moves away from the vertex 1, due to stereoselective crystallization of that enantiomer, towards the metastable solubility curve (dotted line). The curve  $MN$  in Figure 2.5 represents the period in which only the preferred enantiomer crystallizes, or the period between  $t_0$  and  $t_{stop}$  (see Figure 2.4). After that, crystallization of the counter enantiomer arises. The composition of the solution is therefore “pulled” away from the vertex of pure enantiomer 2, and towards the metastable solubility line on the left-hand side. The system eventually reaches equilibrium at point  $O$ , where both liquid and solid phases are at the racemic composition.

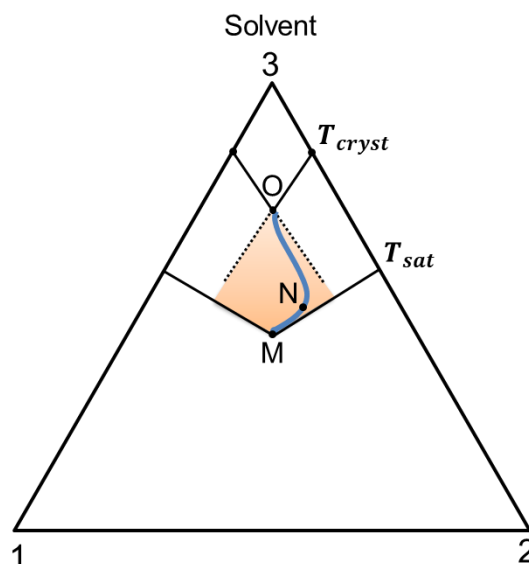


**Figure 2.5** Typical trajectory of isothermal batch preferential crystallization (blue curve) represented in the ternary phase diagram. The points  $M$  and  $O$  are the respective initial and final states.

To assure purity requirements, PC has to be designed in a way of avoiding crystallization of the counter enantiomer. In addition, since 50% of the initial material is the actual desired molecule, only 50% maximum theoretical yield is possible. Several configurations in both batch and continuous mode have been studied with the purpose of overcoming these limitations and making the process more robust. The choice of the most efficient operation mode is substance and process dependent. Several parameters impact the decision-making process, such as desired product form, crystal shape and size distribution, energy requirements, final product application, transportation, available techniques, and more. Most certainly, economic aspects play a crucial role, and may also include environmental impact considerations.

In the recent years there has been an increasing dedication in the scientific community to develop variants for crystallization in both batch and continuous mode (Wood et al., 2019). Several process configurations have been investigated for preferential crystallization, for instance, coupled crystallizers (Chaaban et al., 2013; Elsner et al., 2011; Hein et al., 2013), coupled crystallizer and dissolution tank (CPC-D) (Eicke et al., 2013), mixed suspension mixed product removal crystallizers (MSMPR) (Galan et al., 2015; Köllges & Vetter, 2016) and fluidized bed crystallization (Binev et al., 2016; Temmel et al., 2020; Tung et al., 2009). Comparative performance of liquid exchange PC processes was published by Majumder and Nagy (2017). Jiang and Braatz (2019) recently reviewed a large variety of continuous-flow crystallizers. The authors proposed a five-step procedure for the development of continuous crystallization, and highlighted the importance of batch mode in process design.

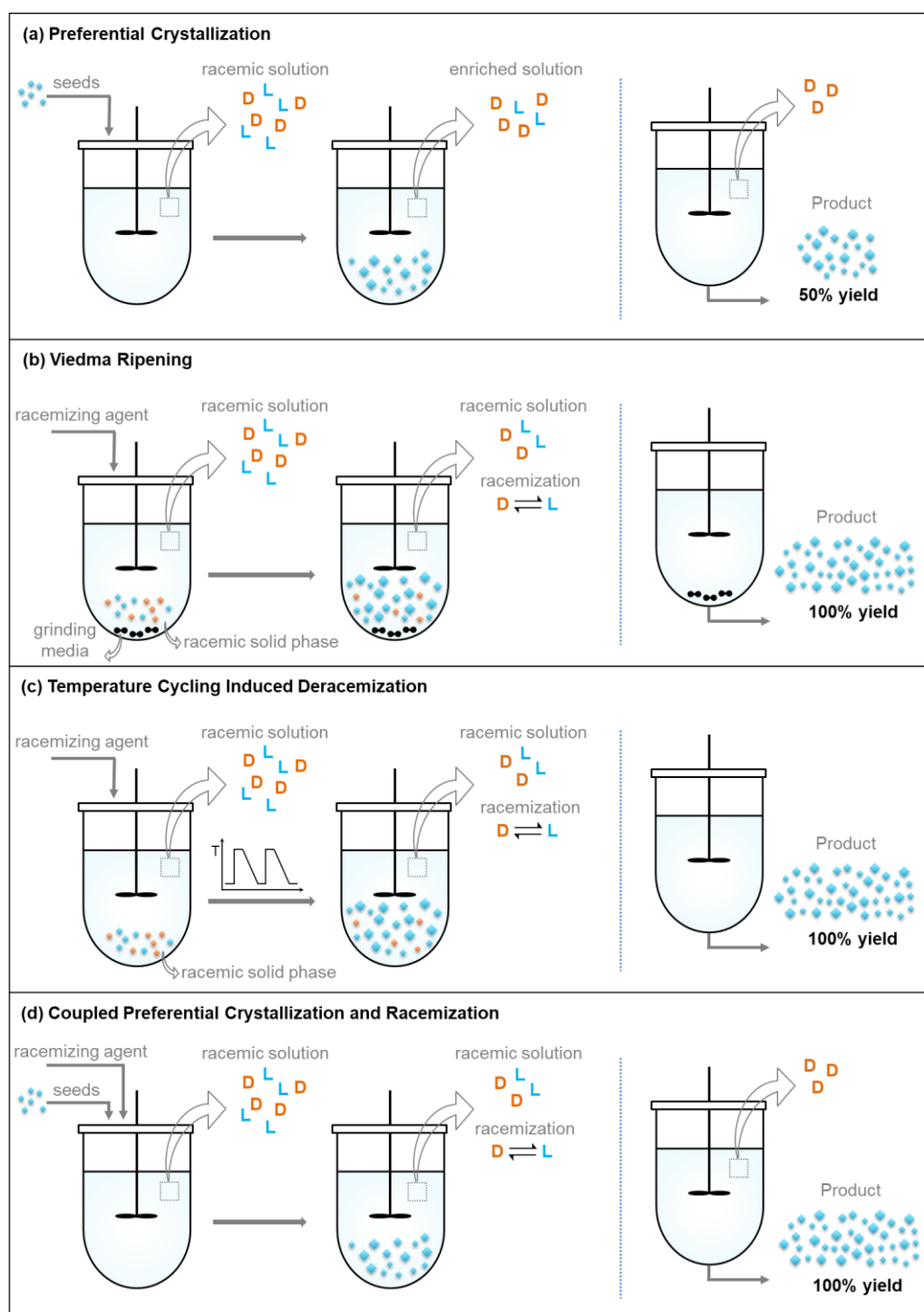


**Figure 2.6** Schematic representation of chiral resolution and maximum theoretical yields of (a) preferential crystallization, (b) Viedma ripening, (c) TCID and (d) coupled PC and racemization.. L (blue) and D (orange) are the target and counter enantiomers, respectively.

In addition to preferential crystallization, other crystallization-based techniques may be suitable for the preparation of optically pure conglomerate-forming enantiomers starting from the racemic mixture. Deracemization methods have been the scope of many studies in the last two decades, since the pioneer work of Viedma (Viedma, 2005). Contrary to PC,

deracemization operates near thermodynamic equilibrium and it can fully convert a racemic crystal population into a single enantiomorphic phase. Viedma ripening or *attrition-enhanced deracemization* (Figure 2.6b) is a result of an intricate multi-phenomenon interaction: crystal growth, dissolution, breakage and agglomeration, Ostwald ripening, and racemization in solution (Iggländ & Mazzotti, 2011; Noorduyn et al., 2010). The conversion of racemic solid phase into crystals of single chirality takes place in the presence of grinding media, and it has also been studied using ultrasound exposure (Xiouras et al., 2018). A systematic model-based study to enable comparison between PC and Viedma ripening in continuous mode has been reported (Koellges & Vetter, 2018). Preferential crystallization was shown to be more productive than Viedma ripening at similar process conditions. The ripening process might be attractive for certain applications for working on thermodynamic equilibrium and the choice of method is strongly compound and process dependent.

Deracemization can also be achieved by the application of small temperature gradients and/or thermal fluctuations instead of particle grinding. This variation was first studied by Viedma (Viedma & Cintas, 2011) and later demonstrated for the resolution a chiral molecule by the groups of Flood and Coquerel (Suwannasang et al., 2013). *Temperature cycling induced deracemization* (TCID) combines the variations between crystal dissolution and recrystallization during the heating and cooling periods, respectively, with racemization taking place in solution. Only very small fluctuations of ca. 2°C are needed to achieve deracemization (Suwannasang et al., 2016). An illustration of TCID is given in Figure 2.6c. This process has an intrinsic higher yield in comparison to preferential crystallization, since the full racemic solid phase is converted into the pure enantiomer, but it is limited to the amount of crystals that remain undissolved at the end of the cycles. The final cycle at lower temperature must be long enough to achieve 100% theoretical yield.

### 2.3.1 Preferential Crystallization and racemization

Coupling preferential crystallization and racemization offers the possibility of overcoming the yield limitations intrinsic to the optical resolution process. This is particularly interesting when only one of the enantiomers is the desired pharmaceutical ingredient. In that case, crystallizing both molecules of the chiral pair, for instance in preferential crystallization operated in coupled crystallizers, would not necessary be profitable. Racemizing the counter enantiomer is not only a more economical and sustainable design, promoting the recycle of the unwanted molecule, but it also helps avoiding the crystallization of that enantiomer and consequent contamination of the solid product. An in ideal coupling of PC with racemization,

the mother liquor is constantly kept at the racemic mixture and the product maintain 100% purity. A schematic representation of the coupling is given in panel d, Figure 2.6. This process combination has been referred to as “crystallization induced asymmetric transformation” (Yoshioka, 2006) and “second-order asymmetric transformation” (SOAT) (Levilain & Coquerel, 2010).

Pioneer works to report this process combination date from 1970s decade. In a cyclic manner, enantiomeric salts of the amino acid lysine were resolved by preferential crystallization and the waste solution with excess of the D enantiomer was racemized by thermal treatment at 170 °C. The successive resolution and racemization resulted in total 90% yield and around 98% purity of target enantiomer (Yamada et al., 1973). Optically pure  $\alpha$ -amino- $\epsilon$ -caprolactam, a lysine derivative, was produced via PC with *in situ* racemization realized by metal complexation with nickel ions in ethanol. As a result, the desired molecule was obtained with 92% yield and 97% enantiomeric excess (Sifniades et al., 1976). An intermediate of the antibacterial cephalosporin was obtained via PC with 80% yield and 84% enantiomeric excess using DBU as racemizing agent (Murakami et al., 1993). A more recent successful example is the resolution of a precursor of Paclobutrazol via PC with grinding. The *in situ* racemization was promoted by alkaline solution due to the presence of 1% sodium hydroxide. The enantiopure agrochemical with 96% enantiomeric excess has been obtained in 70% yield from the racemic mixture (Levilain et al., 2009).

While chemo-catalysis has been often used in the combination with PC, the application of enzymes for that purpose appeared only in the work from Würges, Petrussevska-Seebach and coworkers. The authors proposed for the first time the process integration which was named “enzyme-assisted preferential crystallization” (Würges et al., 2009b), and demonstrated a proof of concept (Würges et al., 2009a). The desired coupling was reported for the resolution of asparagine enantiomers with *in situ* enzymatic racemization via the amino acid racemase. The use of biocatalysts opens a larger range of possibilities for improving PC via the combination with racemization. The process conditions are also amplified, as chemical and thermal catalysis are set at rather harsh reaction conditions and can often lead to decomposition (Yoshioka, 2006). Along the present work, the expansion of this combination and process setups more adaptable to the industry are investigated, particularly with the use of immobilized enzymes and their application in flow reactor.

More recently, the group of Coquerel has shown an experimental-based comparison between coupled preferential crystallization and racemization with temperature cycling induced

deracemization (Oketani et al., 2018). The model compound used, namely 2-methoxy-1-naphthamide, is a conglomerate-forming system and presents spontaneous racemization in the absence of any racemizing agent. The experiments were performed in the 1 g to 10 g scale. The authors reported that the productivity of the integrated PC and racemization (average of 135 g/h/L) was over hundred times higher than TCID (average of 0.67 g/h/L). Such a comparison has also been reported in model-based investigation comparing the coupled process in continuous mode and Viedma ripening (Köllges & Vetter, 2016).

### 2.3.2 Driving force calculations in the TPD

The ternary phase diagram can be used to evaluate the driving forces during preferential crystallization (Jacques et al., 1994; Temmel et al., 2018). Figure 2.7 illustrates the driving force calculations for conglomerates that form (a) anhydrous and (b) solvate crystals. The curves  $AO$  and  $BO$  are the solubility isotherms at the crystallization temperature for target and counter enantiomer, respectively. The starting composition of the system (at point  $M$ ) is given by the racemate solubility at the saturation temperature  $T_{sat}$ , which is a higher than the crystallization temperature  $T_{cryst}$ . At the start of the process, both enantiomers are equally supersaturated. The distances between the initial point  $M$  and the extended solubility lines are the same, as showed in panel (a). When the target enantiomer starts crystallizing, its concentration depletes, and the process trajectory moves away from the pure enantiomer (or pure hydrate/solvate) towards the extended solubility curve. The distances between the prolonged solubility curve and the process point reduces (panel (b)). The supersaturation of the undesired enantiomer increases until primary nucleation occurs and this substance starts crystallizing. Then, its respective distances also deplete until the system reached equilibrium at point  $O$ .

Supersaturation is evaluated by the described *distances* between the extended solubility curve and the process trajectory. Saturation mass fractions  $w_{sat,i}$  are needed to calculate supersaturation (see equation 2.1). At a given process time,  $w_{sat,i}$  (red dots in Figure 2.7) can be obtained by the intersection between the prolongation of the solubility isotherms (dotted) and the tie-lines (dashed) connecting the time-dependent current liquid composition (at  $M$ ,  $N$  or any point along the process trajectory) with the corresponding pure enantiomer or pure hydrate/solvate (points 1 and 2).

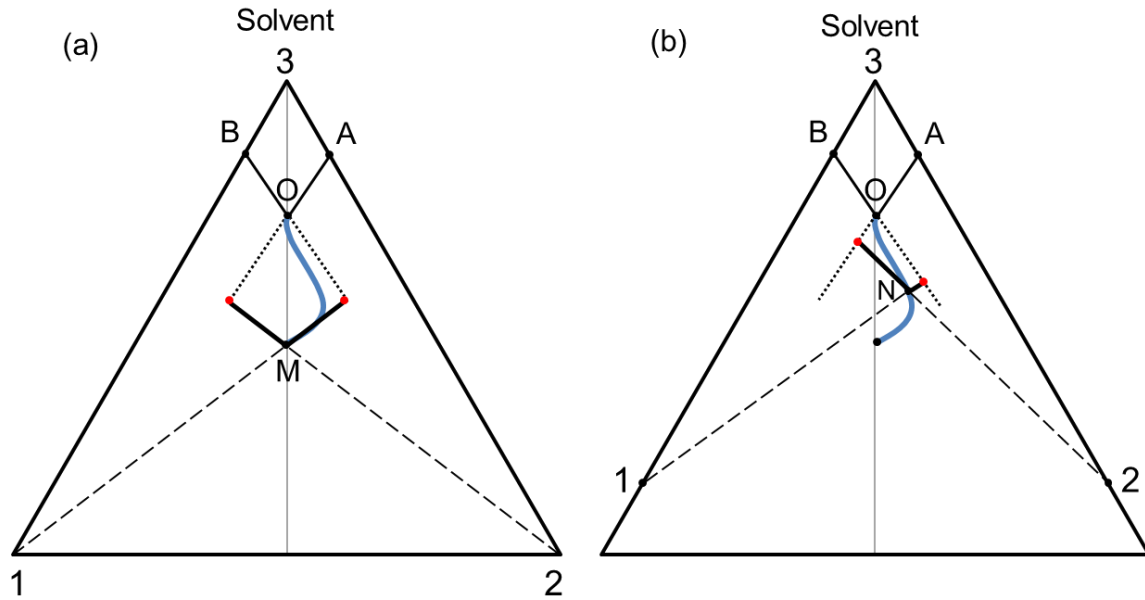


**Figure 2.7** Calculation of driving forces during preferential crystallization using the TPD. Conglomerates illustrated for (a) non-solvate and (b) solvate systems. Saturation concentration  $w_{sat,i}$  (red dots) are the intersection between metastable solubility and the tie lines connecting pure components and current state point. Illustration of the calculations are demonstrated at (a) initial condition M and (b) any process point N.

In order to find the intersection between solubility curves and the tie-lines, a mathematical description of each of these curves is needed. The characteristics of the equations (slope and intercept) are more easily calculated in the orthogonal X-Y or Cartesian plane. Mass fractions ( $w_1, w_2$ ) can be converted to Cartesian coordinates ( $X, Y$ ) by coordinate transformation. The equations for the transformation are shown below and their description can be found in Appendix A.1.

$$X = \frac{1}{2}(1 - w_1 + w_2) \quad (2.7)$$

$$Y = \frac{\sqrt{3}}{2}(1 - w_1 - w_2) \quad (2.8)$$

$$w_1 = 1 - X - \frac{Y}{\sqrt{3}} \quad (2.9)$$

$$w_2 = X - \frac{Y}{\sqrt{3}} \quad (2.10)$$

The approach here described is a convenient way to calculate supersaturation for each enantiomer when simulating PC. This method to evaluate the driving forces during PC was used

in the *Shortcut Model* described in Chapter 6. The same calculations can also be used in combination with population balance equations.

### 2.3.3 Modeling of Preferential Crystallization

Population balance equations (PBE) are the base for the most broadly used models to describe preferential crystallization. The use of PBE has considerably increased in the past two decades, and its applications are dedicated not only to the prediction of crystallization processes and crystal morphology, but also to a diversity of other fields, for instance, bioreactor design in bioengineering, cell biology for tissue engineering, and fluid dynamics in energy fuels (Ramkrishna & Singh, 2014).

The concept of population balances was extensively discussed by Randolph and Larson and later by Ramkrishna (Ramkrishna, 2000; Randolph & Larson, 1988). It is based on quantification of the dynamics of a population of entities interacting with a continuous phase. The nature of these entities can vary depending on the application, for instance, they can be solid particles, liquid droplets or gas bubbles. Characteristic driving forces induce the transfer of mass, momentum and energy between the two phases. In crystallization processes, the entities are solid particles (crystals) which are dispersed in a liquid phase. The fundamental aspect that dictates the changes in such systems is the equilibrium state. It is determined by solid-liquid equilibria described in phase diagrams. In addition to thermodynamic aspects, process kinetics needs to be considered in order to describe the dynamic behavior of the particulate population. Therefore, kinetic models for all phenomena involved in the studied crystallization process (e.g. growth, nucleation, aggregation, breakage, etc.) must be incorporated in the population balance. In the following sub-sections, a set of equations to describe batch PC is presented.

#### 2.3.3.1 Solid phase

To represent the independent properties of the particles, external and internal coordinates must be defined. The external coordinate describes the physical location of the particle. Assuming a perfectly mixed batch crystallizer, the population distribution is equal throughout the whole crystallization volume. Therefore, the changes in particle features are independent from spatial position and the external coordinate can be neglected. The internal coordinates represent intrinsic properties of the crystals, such as size (e. g. characteristic length, mass, or volume), porosity, and morphology. Often, only one internal coordinate is employed. The one-

dimensional PBE described in this work is defined along the characteristic length coordinate  $L$  (Figure 2.8).

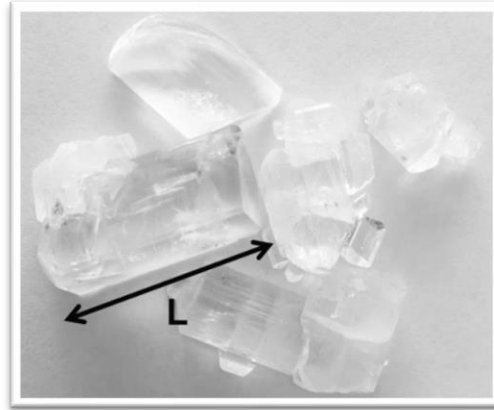


**Figure 2.8** Definition of characteristic length  $L$  used to represent the particulate system in PBE.

The formulation of PBE is based on the number density function  $f$ . It is commonly modeled by a partial differential equation (PDE) which must be defined for each enantiomer  $i$ . For a perfectly mixed batch PC process taking place in a constant volume, the PBE can be written as the following:

$$\frac{\partial f_i(L, t)}{\partial t} = -\frac{\partial}{\partial L}(G_i(S, L, t)f_i(L, t)) \quad i = 1, 2 \quad (2.11)$$

The expression on the left hand side describes the evolution in number density function of each enantiomer  $i$  ( $1 = \text{target}$ ,  $2 = \text{counter}$ ) with respect to time  $t$ . The function  $f_i(L, t)$  represents the particle size distribution and has the unit of number per length (e.g. #/m). In the particle size distribution each particle belonging to the population is associated to the internal coordinate  $L$ . On the right hand side of equation 2.11,  $G$  is the growth rate and it represents the transport of particles into and out of the size interval  $dL$ . The nucleation rate is introduced in the model as a boundary condition of the growth rate, when crystal size  $L$  is equal to zero. Other rates affecting a crystallization process may be introduced to the right hand side of the PBE to account for agglomeration, attrition and breakage. These phenomena are affected by kinetics and most importantly by mechanics of each specific system. Hence, they are difficult to formulate in a general manner (Mersmann, 2001). When describing preferential crystallization, it can be assumed that crystal growth due to supersaturation  $S$  is the most important factor for progress of the density function. Therefore other phenomena can be neglected. In this case, and assuming a size-independent growth rate, the PBE holds as the following:

$$\frac{\partial f_i(L, t)}{\partial t} = -G_i(S, t) \frac{\partial f_i(L, t)}{\partial L} \quad i = 1, 2 \quad (2.12)$$

Equation 2.12 is resumed to a homogeneous partial differential equation, composed of an accumulation term and a convective term, the last one generated by crystal growth. No flux terms of inlet or outlet are presented since it consists of a representation of a batch process. Initial conditions are necessary to solve the PBE. Since the process starts by seeding with the preferred enantiomer, the following initial conditions can be chosen:

$$f_1(L, t = 0) = f_{seeds} \quad (2.13)$$

$$f_2(L, t = 0) = 0 \quad (2.14)$$

$f_{seeds}$  represents the size distribution of the seed crystals of the target enantiomer. For the counter enantiomer, the initial number density function  $f_2$  is zero since only primary nucleation is considered. In equation 2.13, the initial particle size distribution of the seeds can be for instance approximated by a Gaussian distribution:

$$f_{seeds} = \frac{A_{seeds}}{(L \sigma_{seeds} \sqrt{2\pi})} e^{-0.5 \left( \frac{\ln(L-\bar{L})}{\sigma_{seeds}} \right)^2} \quad (2.15)$$

where  $\bar{L}$  and  $\sigma_{seeds}$  are respectively the mean crystal size and the standard deviation of the seeded crystals. Their values are determined from parameters of seed crystals measured during experiments.  $A_{seeds}$  is the scaling factor, which is implemented since only a sample of the mass of seed crystals  $m_{seeds}$  is analyzed. This factor is calculated as:

$$A_{seeds} = \frac{m_{seeds}}{m_{sample}} = \frac{m_{seeds}}{k_v \rho_S \int_0^L L^3 f_{sample} dL} \quad (2.16)$$

where  $m_{sample}$  is the mass of seeds sampled. This quantity is calculated from the third moment of the seed fraction density function  $f_{sample}$ .  $k_v$  is the volume shape factor and  $\rho_S$  the density of the solid phase.

The boundary condition for equation 2.12 is given at  $L = 0$  for the nuclei population density. This means that primary nucleation is assumed to take place at negligible size particles, i.e. size “zero”, and it is related to the nucleation rate  $B_i$  as the following:

$$f_i(L = 0, t) = \frac{B_i(S, t)}{G_i(S, t)} \quad i = 1, 2 \quad (2.17)$$

### 2.3.3.2 Continuous phase

In addition to population balance equations, conservation laws need to be taken into account. In an isothermal process no energy balance is required, but appropriate mass balance is needed to describe the continuous or liquid phase. The changes in bulk concentration of enantiomer  $i$  are equal to the changes in the solid phase, and the general mass balance is:

$$\frac{dm_i}{dt} + \frac{dm_{S_i}}{dt} = 0 \quad i = 1, 2 \quad (2.18)$$

where  $m_i$  and  $m_{S_i}$  are the mass of enantiomer  $i$  in the liquid and solid phases, respectively. The temporal changes in the solid mass can be related to the number density function  $f_i$  by the third moment of the size distribution, thus resulting on following the relation:

$$\frac{dm_i}{dt} = -3k_v\rho_S G_i(S, t) \int_0^\infty L^2 f_i(L, t) dL \quad i = 1, 2 \quad (2.19)$$

where  $k_v$  is the volume shape factor,  $\rho_S$  is the density of the solid phase and  $G_i$  is the size-independent growth rate. In the case of the formation of a hydrate or a solvate solid phase, a mass balance for the solvent (index 3) is also required. In PC, the transport of solvent from the continuous to the dispersed phase depends on the crystallization of both enantiomers:

$$\frac{dm_3}{dt} = -\left(\frac{m_1}{dt} + \frac{dm_2}{dt}\right) \left(\frac{M_S}{M_i} - 1\right) \quad (2.20)$$

where  $M_S$  and  $M_i$  are respectively the molar masses of the solid phase (which includes the respective solid content) and that of the non-solvate enantiomer. The initial conditions necessary to solve equations 2.19 and 2.20 are the following:

$$m_i(t = 0) = m_i^0 \quad i = 1, 2 \quad (2.21)$$

$$m_3(t = 0) = m_3^0 = m_{tot}^0 - m_1^0 - m_2^0 \quad (2.22)$$

where  $m_i^0$  is the initial mass of enantiomer  $i$  dissolved in the liquid phase and  $m_3^0$  is the initial mass of solvent calculated from the total mass balance in the liquid phase.

### 2.3.3.3 Kinetic models

The overall description of the system is completed with kinetic models for the evaluation of growth and nucleation rates. Some models are based exclusively on effects occurring on the molecular level. They are mostly difficult or even impossible to be parametrized experimentally (Mersmann, 2001). Instead, semi-empirical correlations have been proposed to lump all microscopic effects. Typical power laws can be used to describe kinetic models for preferential crystallization and are presented in the following.

The kinetics of both growth and nucleation are clearly dependent on supersaturation. Growth is the predominant kinetic effect in seeded crystallization. The phenomenon is, in practice, dependent on the individual crystal size (i.e. on its characteristic length  $L$ ), as discussed previously in this chapter. Nevertheless, for sake of simplification, growth rate dispersion and size-dependent growth effects were neglected. Thus, crystal growth rate  $G_i$  can be expressed as the power law (Randolph & Larson, 1988):

$$G_i(t) = k_{g_i}(S_i - 1)^{g_i} \quad i = 1,2 \quad (2.23)$$

Equation 2.23 derives from equation 2.5, which describes the temporal changes in mass due to growth according to the diffusion-reaction theory. The growth rate  $G_i$  in equation 2.23 gives instead the changes in the characteristic dimension  $L$  over time, i.e.  $dL/dt$ . The fitting parameters are the crystal growth coefficient  $k_{g_i}$  and the exponent  $g_i$ . The dependency of  $k_{g_i}$  on temperature  $T$  can be described using Arrhenius approach, where  $k_{g_i}^0$  is the pre-exponent term and  $E_{Ag_i}$  is the activation energy (Mullin, 2001):

$$k_{g_i} = k_{g_i}^0 e^{-\frac{E_{Ag_i}}{RT}} \quad i = 1,2 \quad (2.24)$$

Nucleation can be differentiated in primary or secondary, as described in the first section of this chapter. The overall effect of nucleation is a combination of these two processes:

$$B_i(t) = B_{sec_i}(t) + B_{prim_i}(t) \quad i = 1,2 \quad (2.25)$$

For the target enantiomer, secondary nucleation is the most relevant of those two during preferential crystallization. It takes into account the formation of new crystals in the presence of existing ones. They are formed essentially by breakage, through impact with, for instance,

the impeller, crystallizer walls or other particles. A power law to describe this phenomenon can be written as (Myerson, 2002):

$$B_{sec_i}(t) = k_{b_{sec_i}}(S_i - 1)^{b_{sec_a}}(\rho_{susp})^{b_{sec_b}} \quad i = 1,2 \quad (2.26)$$

The quantity  $k_{b_{sec_i}}$  is the secondary nucleation rate coefficient,  $\rho_{susp}$  is the crystal suspension density (mass of crystals per volume of solution) and  $b_{sec_a}$  and  $b_{sec_b}$  are the model exponents. If secondary nucleation is the main mechanism for nucleation, the order of suspension density  $b_{sec_b}$  tends to the value of 1 (Myerson, 2002). Similarly to the growth rate coefficient, the quantity  $k_{b_{sec_i}}$  can be represented by an Arrhenius formulation:

$$k_{b_{sec_i}} = \omega^{n_b} k_{b_i}^0 e^{-\frac{E_{Ab_i}}{RT}} \quad i = 1,2 \quad (2.27)$$

The equation shows the dependency of secondary nucleation on temperature, with the pre-exponential factor  $k_{b_i}^0$  and activation energy  $E_{Ab_i}$ .

Primary homogenous nucleation takes place at higher supersaturation levels. It accounts for the spontaneous formation of nuclei in absence of pre-existing crystals. Hence, during preferential crystallization this phenomenon is mostly relevant for the counter enantiomer. Based on classical nucleation theory, the primary nucleation rate can be formulated as (Mullin, 2001):

$$B_{prim_i}(t) = k_{b1_{prim}} e^{-\left(\frac{k_{b2_{prim}}}{\ln(S_i)^2}\right)} \quad i = 1,2 \quad (2.28)$$

where  $k_{b1_{prim}}$  is the pre-exponent factor and  $k_{b2_{prim}}$  is the exponential factor, which is dependent on process conditions such as crystal shape, crystal surface tension and temperature.

### 2.3.3.4 Numerical solution

The Method of Moments (MOM) (Hulburt & Katz, 1964) is an efficient reduction technique for the population balance equations of the type of equation 2.11. Whereas PBE give the complete particle size distribution, the MOM allows the calculation of representative terms to describe a particle size distribution, namely average values and total quantities. In addition, the method also helps fixing possible dimension incongruence that may occur between PBE and transport equations (Randolph & Larson, 1988).

To describe preferential crystallization, the  $k$ th moment must be calculated for each enantiomer  $i$ . The  $k$ th moment of a distribution is defined as the following:

$$\mu_k = \int_0^{\infty} L^k f(L) dL \quad (2.29)$$

The moments of the number density function  $f(L)$  correspond to different properties of the solid particles. Even though the calculation of an infinite number of moments is possible, only the first four (i.e.  $\mu_0$  to  $\mu_3$ ) represent physical properties and are sufficient to describe a crystal population (Mersmann, 2001). Each of them is calculated per unit volume of suspension.

Table 2.1 describes the properties of a crystal distribution calculated by the moment equations. The zeroth moment gives the volume-related total number of crystals and the first moment gives the volume-related cumulative length of all crystals. The second and third moments are proportional to the total surface area and total volume of particles, respectively. They are calculated using the area and volume shape factors ( $k_a$  and  $k_v$ ), which relate the respective area and volume of a particle to the characteristic length  $L$ .

**Table 2.1:** Features of a particulate distribution described by the first low order moments (0 to 3) using the method of moments.

Property of the distribution	Related moment	Formulation	Unit
Total number of particles	$\mu_0$	$N_{tot} = \mu_0$	[#/m <sup>3</sup> ]
Total length of particles	$\mu_1$	$L_{tot} = \mu_1$	[m/m <sup>3</sup> ]
Total surface area of particles	$\mu_2$	$A_{tot} = k_a \mu_2$	[m <sup>2</sup> /m <sup>3</sup> ]
Total volume of particles	$\mu_3$	$V_{S_{tot}} = k_v \mu_3$	[m <sup>3</sup> /m <sup>3</sup> ]

The total mass of a crystal population can also be calculated from the third moment using the density of the solid phase  $\rho_s$ . Applied to the population balance, this relation is used to estimate, for instance, the initial particle size distribution of seeds (section 2.3.3.1), and the temporal changes in the liquid phase due to crystallization (section 2.3.3.2).

$$m_{S_{tot}} = \rho_s k_v \int_0^{\infty} L^3 f(L) dL \quad (2.30)$$

Another relation that can be extracted from the moments of density function is the mean size of the particles, calculated as the ratio between the total length of all crystals (first moment) and total number of crystals (zeroth moment):

$$\bar{L} = \frac{\mu_1}{\mu_0} \quad (2.31)$$

As any reduction model, the MOM causes some loss of information on the size distribution. Nevertheless, it still gives a complete mathematical representation of particulate systems while requiring less computational time than full PBE. Therefore, it has been considered since some decades as an appropriate technique to describe the evolution of particulate systems (Ramkrishna & Singh, 2014; Randolph & Larson, 1988). Population balance equations together with the method of moments can be solved, for instance, using discretization methods such as high resolution finite volume method.

## 3 Fundamentals of Enzymatic Racemization

In this chapter, the fundamentals for understanding enzymatic reactions with focus on racemization are summarized. The first part is dedicated to an overview on biocatalysis, techniques for production of recombinant proteins, purification of His-tagged proteins and methods for enzyme immobilization. That is followed by the presentation of racemases and their relevance. The development of kinetic equations is then demonstrated for typical Michaelis-Menten mechanism and its reversible variation. Lastly, the mode of operation and mass balances for enzymatic batch and flow reactors are briefly introduced.

### 3.1 Biocatalysis

Catalysis is explored since early in history on the production of ether, alcoholic beverages (beer and wine), cheese, and soap. Since the time of first industrial revolution it has been progressively employed in the industry to promote or improve chemical production (Armor, 2011). *Catalysts* are essential agents of these processes. They act by facilitating the conversion of reactants into products in a series of elementary steps, but there are not consumed during the reaction. They are regenerated at the end of each cycle, leaving the possibility of being continuously reused (Dumesic et al., 2008). From an energetic point of view, catalysts decrease the activation energy necessary for the reaction, and consequently increase the rate of that reaction. Therefore, they change the kinetics of a chemical reaction, but not its thermodynamics. This effect is exemplified in Figure 3.1. The reaction proceeds at a different pathway with lower activation energy. However, the initial and final equilibrium plateaus remain unchanged.

The use of *biocatalysts* gives an attractive alternative to chemical catalysis. Their application under rather mild reaction conditions regarding solvent, temperature and pressure is the most prominent of the advantages, but they can also outdo chemo-catalysts by high stereo- and regio-selectivity, high substrate specificity, and biodegradability (Horn et al., 2008). Some limitations of using biocatalysts are narrow operation parameters, the fact that they are prone to inhibition and might require a cofactor (Faber, 2018). Another main issue is the separation from reaction media. Therefore, many studies have been dedicated to the advance in protein immobilization (Sheldon & van Pelt, 2013). Another challenge is the relatively long period required for development and design of a biocatalytic process. In this matter, the costs can

substantially increase, particularly if the production requires application of methods such as purification and immobilization (Fu et al., 2012). In case of highly-priced preparation, the application of enzymes is narrowed to the production of fine chemicals and pharmaceuticals. The most important analysis is the relation between the cost contribution of the biocatalyst and the added value brought by its implementation, which is, for instance, improved product yield and/or purity, fewer production or processing steps, environmentally friendly process (Tufvesson et al., 2011).

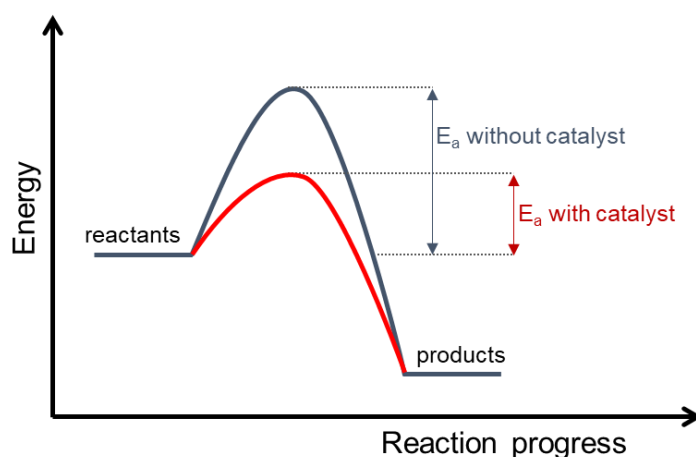


**Figure 3.1** Illustration of potential energy diagram of a generic exothermic reaction occurring in the absence and presence of a catalyst (blue and red curves, respectively). The resulting activation energy  $E_a$  is lower in a catalyzed reaction.

Biocatalysts or enzymes are proteins with catalytic functions. They are identified by the EC number (enzyme commission number) according to the chemical reaction that they catalyze. This classification was defined by the Nomenclature Committee of the International Union of Biochemistry and Molecular Biology (NC-IUBMB) (Webb, 1992). The format of the naming is the abbreviation “EC” followed by a numerical classification composed of 4 digits separated by periods. The first number represents the general class of the enzymes (see Table 3.1) that since 2018 it goes from 1 to 7 (Jeske et al., 2018). The subsequent numbers describe the type of substrate, bond or functional group, co-substrate and serial number.

Enzymes are used in diverse applications in the industry. Among their current larger use are the synthesis of drugs, fine chemicals and products for the food industry, for instance, antibiotics, pure amino acids, fructose syrup and lactose free milk. They are also applied in analytical tools in medicine, as in biosensors for measurement of blood sugar in diabetic patients. Another relevant application is waste treatment, where enzymes produced by

microorganisms act in bioreactors for the treatment of wastewater (Horn et al., 2008; Vogel & May, 2019).

**Table 3.1** Enzyme classification according to the NC-IUBMB.

	<b>Enzyme class</b>	<b>Catalyzed reactions</b>	<b>Examples</b>
1	Oxireductases	Oxidation and reduction	Oxidases, dehydrogenases
2	Transferases	Transfer of complete functional groups	Transferases, kinases
3	Hydrolases	Cleavage by H <sub>2</sub> O	Proteases, peptidases
4	Lyases	Bond formation and cleavage (non-hydrolytic)	Aldolases, decarboxylase
<b>5</b>	<b>Isomerases</b>	<b>Isomerization and racemization</b>	<b>Racemases, isomerases</b>
6	Ligases	Bond formation under energy consumption	Synthetases, carboxylases
7	Translocases	Transport of ions and molecules across cellular membrane	ATPases

### 3.1.1 Production of recombinant proteins

For their complex structure, enzymes cannot be synthesized chemically and must be produced in biological systems. Therefore, a DNA encoding the so called *recombinant protein* is engineered and cloned into a host cell (Overton, 2014). This allows the production of the desired enzyme in larger quantities than it would be naturally produced.

The host cell is often of a different species than the original one. The choice of the most appropriate host depends on the chemical properties of the target protein. For more complicated molecules, for instance glycosylated proteins, eukaryotic systems (mammalian cells) are the best choice. Prokaryotic systems are preferable for the expression of rather simple proteins (Vogel & May, 2019). Bacterial hosts are often used for their lower costs and shorter process times. *Escherichia Coli*, originally a mammalian gut bacterium, is a cost-effective, well-known metabolic system, and considered to be of safe use in laboratories and industry. Its first industrial application was the production of insulin by Genentech, approved in 1982 by regulatory agencies in Germany, United States, United Kingdom and the Netherlands (Johnson, 1983; Pieracci et al., 2018).

The first step of recombinant protein production is to clone the plasmid encoding the protein followed by its transformation to the host cell. The plasmid is the DNA molecule

composed, among other parts, by the protein gene, an antibiotic resistance gene and a promoter (Overton, 2014). The antibiotic resistance gene helps avoiding contamination of the culture by selection of the host microorganism containing the recombinant protein expression gene. The promoter regulates in which moment of the cell growth cycle the expression of the gene will take place. That is activated by a chemical inducer added during fermentation.

The expression vector can also contain a tag fused to the recombinant gene. Tags can be engineered either to the N- or C-terminus of the protein. Several commercial tags are available, and their applications are extensive: enable easier purification, enhance protein solubility, promote fusion with other proteins, detect protein location (e.g. fluorescence detection), transport the protein to a desired cellular compartment, study protein interaction and functional analysis (Jarvik & Telmer, 1998; Rosano & Ceccarelli, 2014).

Once the host is prepared, the next step is cell growth. The growth medium plays an important role on bacterial fermentation: it is the source of nutrients for the host, e. g. carbon and nitrogen sources, amino acids, metal ions and vitamins. During the fermentation, a chemical is added to activate the promoter and induce the protein expression. The induction strategy also needs to be contemplated (Figure 3.2). The protein expression can be induced at low or high levels of biomass, depending if growth is competing for resources with protein expression (Overton, 2014). In cases where cell growth critically inhibited by induction, the biomass decreases considerably after protein starts to be expressed.

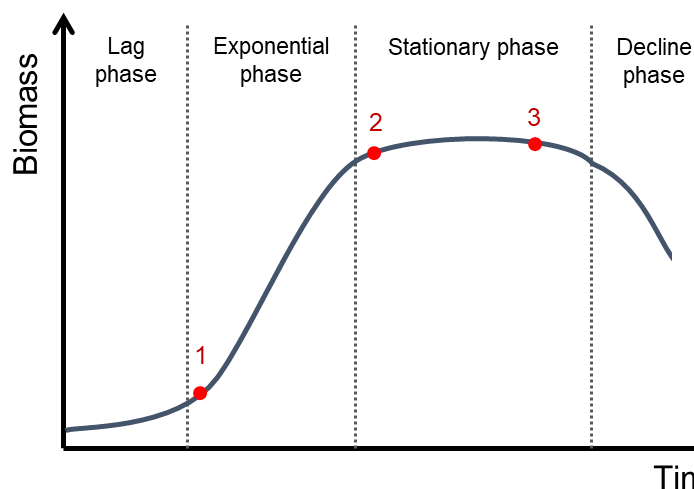


**Figure 3.2** Growth curve of bacterial population. Strategy for induction of recombinant protein expression: 1) induction at low biomass, possible if growth and expression do not compete for metabolic resources; 2) induction at high biomass, clear separation between growth and production of target protein; 3) induction is toxic and at any phase it can strongly inhibit growth and cause cell death.

During expression, the formation of inclusion bodies can occur. They consist of dense particles comprising unfolded or partially folded proteins (Baneyx & Mujacic, 2004). This happens because production of recombinant proteins is in “unnatural” high concentrations, and this can cause a metabolic burden for the host. It can be avoided by decreasing growth temperature and concentration of inducer, which minimizes the stress in the cell and allows accumulation of protein in the correct folded form.

When the desired biomass and protein content levels are reached, the protein can be captured. Recombinant proteins can be expressed intra- or extracellular. If they are released to the growth medium, only centrifugation is required to separate cells from fermentation media containing the protein. In the case of intracellular production, the cells are as well separated from the medium by centrifugation, but in this case the biomass is recovered. The final step is then to disrupt the tissue to release protein from within the cells. Several methods can be used for disruption, depending on the cell amount and type. The methods can be classified as (i) chemical, (ii) enzymatic, (iii) physical and (iv) mechanical. The first two methods are based on the use of additives, such as detergents or lysozyme. In (iii), osmotic, pH or temperature shock can be applied. Even though these past approaches are used, mechanical methods are considered the most industrially relevant (Pieracci et al., 2018). For instance, for relatively small volumes of bacteria, sonication can be applied, in which high frequency sound waves are applied to break the cells. In a larger scale, high pressure homogenization is preferable. In this method, the cell suspension is forced through a small orifice in order to disrupt the cells (Wilson & Walker, 2010). The resulting suspension must be centrifugated to remove the cell debris from solution.

### **3.1.2 Purification**

Many industrial enzymes are used in the crude form. These preparations consist of hundreds or thousands of proteins, buffer salts, and substances used during the fermentation. Typical cell extracts contain from 1 to 30% of the target protein (Faber, 2018). Novel recombinant proteins need to be purified to facilitate characterization. For the desired application, they can be employed in the crude form if the enzyme is sufficiently active. However, the impurities often interfere with the enzymatic activity. The non-specific proteins present in the extract solution can, for instance, catalyze side-reactions and impact the selectivity of the process (Chaplin & Bucke, 1990).

Classic techniques of protein purification are multi-step (Doonan, 2002; Murray et al., 2014). The successive methods exploit a combination of fractionated precipitations (e.g.

changing pH, adding salts, alcohols or organic solvents) with one or a sequence of chromatographic methods, for instance, ion exchange, size exclusion, affinity chromatography, and gel filtration.

Recombinant proteins can be tailored to be readily purified by affinity chromatography. The so called *fusion* or *tagged proteins* hold a pre-defined domain able to interact with a specific affinity support. One of the most popular approaches is the addition of a fusion tag with six consecutive histidine residues. The poly histidine residues are attached to the N or C terminus of the recombinant protein, the best choice being one that gives the tag accessibility to the protein surface (Todorova & Vijayalakshmi, 2005). The poly His-tag has strong affinity to transition metals and allow complexation with those ions. So, a simplified purification protocol using immobilized metal ion affinity chromatography (IMAC) is possible to achieve.

The concept of IMAC as a purification technique for complex molecules was first introduced by Porath and coworkers (1975). The histidine chain of the target protein binds to the metal ion chelated on a support to be separated from the cell extract and subsequently eluted (Figure 3.3). Elution can be held by addition of high concentrations of imidazole, a substance that competes with the Histidine chain for the metals. The most common metal used is nickel Ni(II), but other possibilities are iron Fe(II), copper Cu(II), zinc Zn(II) and cobalt Co(II). The support material varies with the supplier, the most typical ones are based on cross-linked agarose or high density Sepharose (Todorova & Vijayalakshmi, 2005).

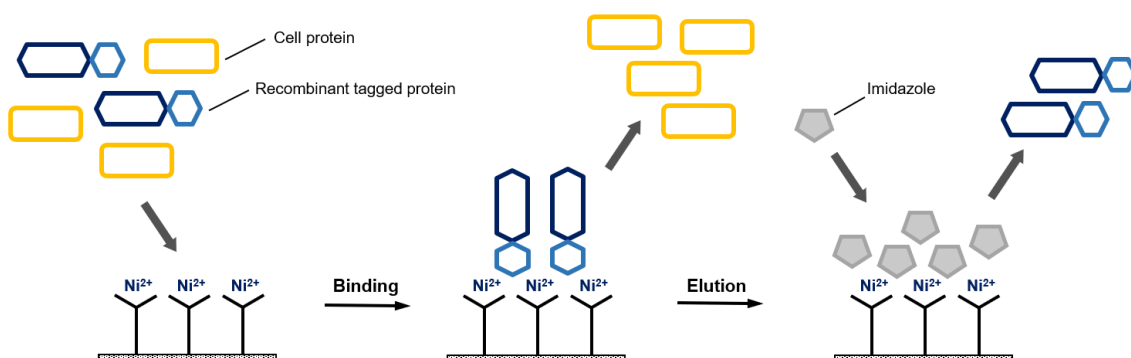


**Figure 3.3** Illustration of His-tag protein purification by immobilized metal ion affinity chromatography (IMAC).

Affinity tags provide the means for the recombinant protein to be selectively removed and recovered from the cell extract. They can also be facilitate protein immobilization via complexation, as discussed in the next section. The purification is relatively rapid and effective, but it often requires pre- and post-treatments. The additional steps include, for instance, filtration, centrifugation, concentration, desalting, buffer exchange, and cleavage of tag.

Unspecific cell proteins that have histidine residues can also bind to the metal ion, elute together with the tagged protein and decrease the final purity (Todorova & Vijayalakshmi, 2005). Another drawback from fusion tags are effects on protein structure, affecting its folding and consequently the enzymatic activity (Doonan, 2002; Murray et al., 2014).

### 3.1.3 Immobilization of enzymes

A catalytic reaction can be classified as homogeneous and heterogeneous. In biocatalysis, a homogeneous reaction is performed with free, soluble enzyme in cell extract or purified preparation. Homogeneous bioreactor can be achieved for instance in membrane reactors (Sheldon 2007). The setup consists of a vessel with ultrafiltration membranes, which enables substrates and products to flow through while retaining the enzyme in the reactor. This approach has been employed in the production of pure enantiomers via kinetic resolution by the company Degussa (Wöltinger et al., 2005) and has been investigated with a racemase in combination with SMB chromatography in a continuous process (Fuereder et al., 2016).

Heterogeneous biocatalysis is achieved upon enzyme immobilization. The advantages of confining the enzyme on a solid surface are to employ it repeatedly and possibly continuously, which can drastically reduce the impact of price the catalyst despite the additional immobilization costs (Tufvesson et al., 2011). Enzyme immobilization allows for recovery and convenient separation from reactants and products facilitating downstream processing. It can also increase the stability, improve prevention of microbiological contamination, and enable the application of different reactor configurations (Brena & Batista-Viera, 2006; Garcia-Galan et al., 2011; Sheldon & van Pelt, 2013). For many enzymes, immobilization is therefore the solution for cost-effective industrial applications. Two of the most relevant industrial applications of immobilized enzymes are the penicillin amidase for production of antibiotics and glucose isomerase for the production of high fructose corn syrup (Bornscheuer & Buchholz, 2005).

Enzyme immobilization techniques are commonly classified in three categories (Sheldon & van Pelt, 2013): (i) cross-linking, (ii) entrapment or encapsulation and (iii) binding to a solid support (Figure 3.4). Enzymes can be cross-linked to a gel matrix or a carrier, but more often this technique is applied as a carrier free immobilization (Murray et al., 2014). Cross-linked enzyme crystals (CLECs) or aggregates (CLEAs) are formed upon enzyme crystallization or precipitation followed by the addition of cross-linking agents (Sheldon & van Pelt, 2013). The aggregates become insoluble and, if they maintain the tertiary structure of the protein molecules, the activity is also preserved. In technique (ii), the enzyme is trapped into gels, fibers or

microencapsulation. It can be performed by the synthesis of a polymer in the presence of the enzyme, which is consequently entrapped in the polymeric network. The approach (iii) is among the most widely used. The nature of the binding can be irreversible, for a covalent coupling, or reversible, using for instance ionic, affinity or hydrophobic adsorption.

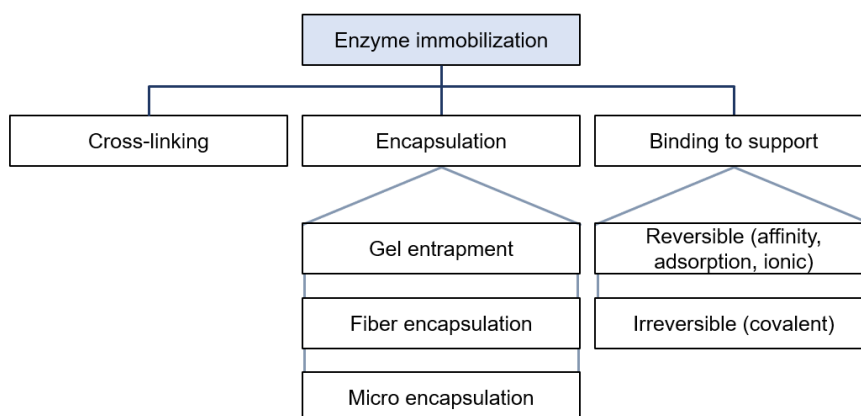


**Figure 3.4** Main techniques for enzyme immobilization.

Covalent binding is a well-known enzyme immobilization strategy. It has the advantage of building a strong, multipoint attachment, which prevents leaching of the catalyst (Figure 3.5). Limitations of this such robust binding are its nonreversible character and the fact that it can chemically modify the enzyme and cause its deactivation (Garcia-Galan et al., 2011). Common porous materials for covalent binding are methacrylic supports functionalized by epoxy or amino groups (Hanefeld et al., 2009). The surface of carriers are designed to either be activated upon a reactive function or are pre-modified to contain the active group.

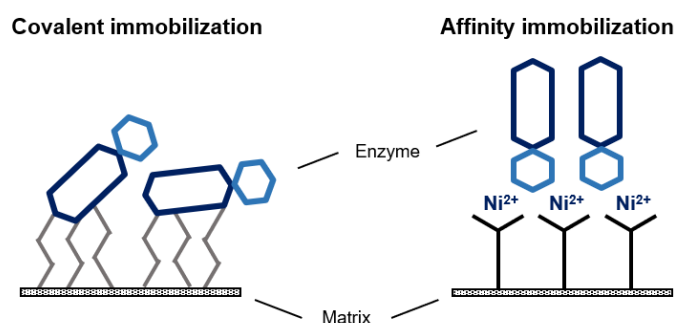


**Figure 3.5** Illustration of covalent and affinity binding immobilization.

Another attractive technique is affinity binding. It provides a combination of purification (or protein enrichment) and immobilization. This is an interesting advantage since it makes the overall process of enzyme production more time and cost-effective (Garcia-Galan et al., 2011). Affinity-binding immobilization also offers fewer risk of conformational change in the biocatalyst structure, provides selective orientation of the enzymes onto the support and the

possibility of re-using the carrier once the enzyme is deactivated (Andreescu et al., 2006). Tagged enzymes are great candidates for this type of enzyme-support binding (Figure 3.5). The immobilization can be performed for instance, on metal-chelate agarose matrixes (Kashlev et al., 1993), commonly used for His-tag purifications, or on metal-chelate porous glass surfaces (Cassimjee et al., 2014). The affinity attachments may generate a less stable immobilization in comparison to covalent binding due to weaker binding strength. The choice of the most appropriate material depends on the immobilized biocatalyst performance, the reaction conditions, and the desired applications. This must be investigated specifically for each case.

### 3.1.3.1 Characterization of immobilized enzymes

Enzymes are characterized by their operational stability and activity. Both of these features are measured by determination of the reaction rate. The properties of an enzyme immobilisate may differ from the soluble preparation. This is often desired, since enzyme immobilization is an important tool to improve operational stability, pH and thermal tolerance (Arya & Srivastava, 2006). However, immobilization may also have a unfavorable impact on the catalytic activity. The kinetic constants change, usually to a hindrance of the activity (Chaplin & Bucke, 1990; Sheldon & van Pelt, 2013). The differences can be due to modifications of the intrinsic activity or alterations of the three-dimensional structure of the protein. But most often the loss in catalytic properties is attributed to the mass transfer effects of substrate and products at the solid-liquid interface of the catalyst and in the porous materials.

Transport phenomena play an important role in reactions of immobilized enzymes. Compared to homogeneous bioreactions, there is limited access to the active site of the immobilized biocatalyst. The reaction rate observed is typically a result of both mass transport and catalytic reaction. The overall process is described by seven steps (Figure 3.6):

- 1) Transport of reactant from the bulk to the boundary layer;
- 2) Transport of reactant from the boundary layer to the particle surface;
- 3) Transport of reactant through the pore towards the enzyme active site;
- 4) Catalytic step;
- 5) Transport of product through the pore to particle surface;
- 6) Transport of product from the surface to the boundary layer;
- 7) Transport of product from the boundary layer to the bulk solution.

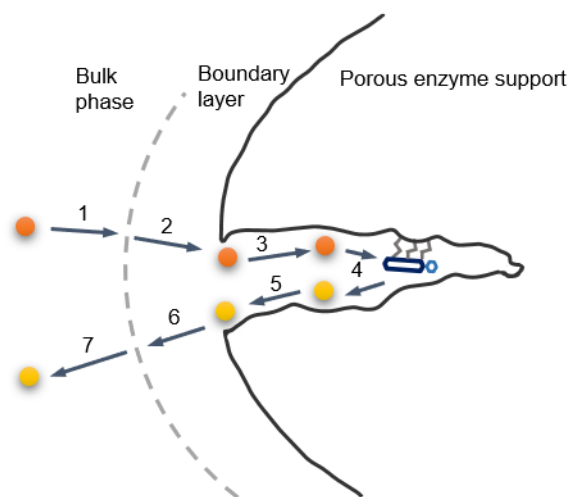


**Figure 3.6** Steps of mass transport in heterogeneous catalysis. Reaction substrate in orange and product in yellow.

In case of strong diffusion limitations, the concentration of substrate moving into the pore is extremely low and almost no reaction takes place. The transport of reactants and products in bulk solution can be improved by changes in the stirring rate or volumetric flow rate, depending on the type of reactor. Internal mass transfer in porous materials is influenced by the size of the particles, the pore diameter and the enzyme loading (Horn et al., 2008).

### 3.2 Racemases

The enzymes facilitating racemization are called *racemases* (Figure 3.7). The racemization reaction is the irreversible interconversion of a pure enantiomer or enantiomerically enriched solution into the racemic mixture. The main characteristic of this isomerization is the loss of optical activity (Ebbers et al., 1997).

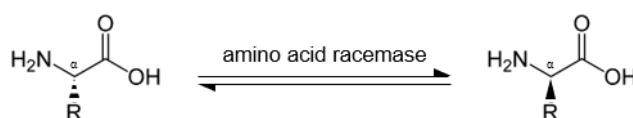


**Figure 3.7** Enzymatic racemization of an  $\alpha$ -amino acid.

Amino acid racemases (AARs) are the large majority of the currently available racemases (Femmer et al., 2016). They are identified by the number EC 5.1.1: main class of isomerases (number 5, see Table 4.1), sub-class of racemases and epimerases (number 1) acting on amino acids and derivatives (number 1). The primary natural application of AARs is the break of L-amino acids optical purity. Those L-stereoisomers are known to be the building-blocks of proteins and largely dominate in nature. Knowledge about functions of D-amino acids have

shown they play crucial roles in physiological processes. The D-enantiomers are employed, for instance, in the synthesis of bacterial peptidoglycans as part of a defense mechanism against degradation (Ebbers et al., 1997; Femmer et al., 2016; Radkov & Moe, 2013).

For the large majority of amino acid racemases, the catalytic activity depends on the presence of a cofactor. The most common cofactor is PLP (pyridoxal 5-phosphate), an active derivative of vitamin B<sub>6</sub>. PLP mediates the formation of an unstable Schiff-base intermediate that allows racemization to occur (Schnell et al., 2003).

For a long time racemization was thought of as an undesired side reaction without relevance in synthetic chemistry, but it has gained the deserved attention in the past decades in the field of asymmetric transformations (Nestl et al., 2007). The major biotechnical application of racemases is the recycling of the unwanted enantiomer in chiral resolutions (Femmer et al., 2016). The most well-known strategy is dynamic kinetic resolution (DKR) (Ebbers et al., 1997; Faber, 2001; Vogel & May, 2019). In DKR, one of the enantiomers in a racemate reacts selectively to supply pure amino acid, while the remaining component is racemized. This results in a theoretical process yield of 100%. Physical separation processes can also benefit from the increase in yield brought by racemization. Racemases have been investigated in combination with chromatography in free (Fuereder et al., 2016) and immobilized forms (Wrzosek et al., 2018). As previously mentioned throughout this thesis, soluble amino acid racemase was applied in-situ in combination with preferential crystallization for production of L-asparagine (Würges et al., 2009a). Other possible industrial applications are alternative routes for the production of D-amino acids starting from prochiral materials. The cheaper L-enantiomer is racemized to generate the D-stereoisomer, which is separated by an enantiospecific reaction. This concept was employed for the production of D-glutamate (Bae et al., 2002).

The enzyme studied in the present work is a well-known amino acid racemase from *Pseudomonas putida* KT2440. This racemase is dimeric protein, each monomer consisting of 409 amino acids with a molecular weight of circa 44 kDa (Würges et al., 2009b). Its activity is PLP-dependent. The amino acid racemase has a broad substrate specificity and potential for preparative biotransformations (Schnell et al., 2003). Kinetic properties of different preparations of this enzyme have been reported with several substrates, including asparagine monohydrate, and it has shown the highest racemization activity converting lysine enantiomers (Lim et al., 1993; Radkov & Moe, 2013). Other properties specific to this amino acid racemase are discussed in the model system section in Chapter 4.

### 3.3 Enzyme kinetics

In order to model an enzyme-catalyzed reaction, it is necessary to understand the mechanism of the progress of the reaction. Detailed mechanisms are rather complex, but useful kinetic rate equations can be developed considering certain assumptions. In the first decades of the 20<sup>th</sup> century, Henri and then Michaelis and Menten proposed a two-step enzymatic reaction mechanism (Cornish-Bowden, 2012). The mechanism is combination of substrate binding followed by chemical transformation with release of reaction product. an exemplification of this mechanism is showed in equation 3.1 for the conversion of the undesired enantiomer  $E_2$  into the target enantiomer  $E_1$  by the enzyme  $E$ .



The first step is a reversible second order reaction with rate constants  $k_1$  and  $k_{-1}$ . It is considered to be fast enough so that the reaction substrate  $E_2$  (counter enantiomer) and enzyme  $E$  are in equilibrium with the complex enzyme-substrate  $EE_2$  formed. The second step is an irreversible first order reaction with rate constant  $k_2$ . Under these considerations, the rate of product formation (target enantiomer) and the changes in concentration of the intermediate  $EE_2$  can be written as the following:

$$\frac{dc_1}{dt} = k_2 c_{EE_2} \quad (3.2)$$

$$\frac{dc_{EE_2}}{dt} = k_1 c_2 c_E - k_{-1} c_{EE_2} - k_2 c_{EE_2} \quad (3.3)$$

In the equations above,  $c_1$ ,  $c_2$ ,  $c_E$ , and  $c_{EE_2}$  are the concentrations of the target enantiomer (product of reaction), counter enantiomer (reaction substrate), enzyme and complex enzyme-substrate, respectively.

Briggs and Haldane (1925) proposed that a steady-state situation is rather quickly established for the formation and decomposition of the enzyme-substrate complex. Hence, this net rate of reaction of the intermediate complex is zero:

$$\frac{dc_{EE_2}}{dt} = 0 \quad (3.4)$$

Hence, equation 3.3 can be rearranged as

$$c_{EE_2} = \frac{k_1 c_2 c_E}{k_{-1} + k_2} \quad (3.5)$$

Assuming constant volume, the sum of the concentration free enzyme  $c_E$  and the enzyme bound to the substrate  $c_{EE_2}$  is the total concentration or catalyst dosage  $D_C$ :

$$D_C = c_E + c_{EE_2} \quad (3.6)$$

So, equation 3.5 can be expressed as a function of  $D_C$ :

$$c_{EE_2} = \frac{k_1 c_2 (D_C - c_{EE_2})}{k_{-1} + k_2} \quad (3.7)$$

Hence:

$$c_{EE_2} = \frac{D_C k_1 c_2}{k_{-1} + k_2 + k_1 c_2} \quad (3.8)$$

The rate of formation of product given by equation 3.2 can be rearranged using the expression for  $c_{EE_2}$  (equation 3.8) as the following:

$$\frac{dc_1}{dt} = D_C \frac{k_1 k_2 c_2}{k_{-1} + k_2 + k_1 c_2} \quad (3.9)$$

$$\frac{dc_1}{dt} = D_C \frac{k_2 c_2}{\frac{k_{-1} + k_2}{k_1} + c_2} \quad (3.10)$$

The elementary reaction rate constant  $k_2$  and the ratio  $\frac{k_{-1} + k_2}{k_1}$  are rewritten as the constants  $V_{max}$  and  $K_M$ :

$$\frac{dc_1}{dt} = D_C \frac{V_{max} c_2}{K_M + c_2} \quad (3.11)$$

The *Michaelis-Menten equation* is the fundamental of enzyme kinetics. It can be written as the reaction velocity scaled by the concentration of the enzyme (e.g. in mol per hour per mass of enzyme):

$$r = \frac{1}{D_C} \frac{dc_1}{dt} = \frac{V_{max}c_2}{K_M + c_2} \quad (3.12)$$

The constant  $V_{max}$  is the maximum reaction velocity, which characterizes is the limiting rate that can be achieved. In this equation,  $V_{max}$  is expressed in mols per unit volume per unit time. For a reaction taking place at rate values close to  $V_{max}$ , most active sites are occupied. In this case, an increase in substrate concentration does not significantly increase the reaction velocity. The parameter  $K_M$  is the Michaelis constant. It represents the dissociation constant of the complex enzyme-substrate.  $K_M$  can be defined as the concentration at which the velocity is half of the limiting one, that is,  $r = V_{max}/2$  (Figure 3.8). The Michaelis constant indicates the affinity of the substrate to the enzyme. When comparing different substrates, the lower the value of  $K_M$ , the greater the affinity enzyme-substrate.

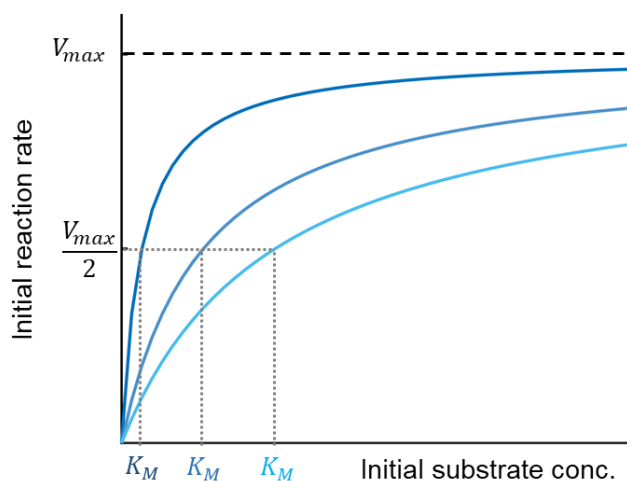


**Figure 3.8** Illustration of Michaelis-Menten hyperbolic plot (equation 3.12): effect of substrate concentration on the initial reaction velocity.  $V_{max}$  is the maximum velocity the enzyme can achieve under defined conditions.  $K_M$  is the substrate concentration at which the reaction velocity is half of the maximum. All curves have the same  $V_{max}$ , but the darker color represents an enzyme greater affinity to the substrate.

The enzyme kinetics can be influenced by several parameters. From the collision theory it is known that reaction rates increase by anything that can intensify the frequency or the energy of molecule collisions (Murray et al., 2014). This effect is also valid for enzyme-catalyzed reactions. Higher temperatures increase the kinetic energy of molecules, so the probability of collision and consequently the reaction rate increase. Every enzyme, however, has a range of temperature over which it can react without denaturation. Heat energy can disrupt non-covalent interactions so that the enzyme structure is irreversibly compromised. Another parameter that affects the reaction rate is substrate. As depicted in Figure 3.8, the rate increases linearly for relatively small concentrations, typically below  $K_M$  values, and it does not vary when the active

sites are saturated (Rao et al., 2006). If the protein is affected by substrate inhibition effects, the biocatalyst produces enzyme complexes that may not be active at high concentrations of reactant. This causes the reaction velocity at high substrate concentrations to reach values below the maximum reaction rate (see section 3.3.2). Another relevant parameter influencing the reaction rate is pH. The hydrogen ion concentration in solution may alter the charged state of the enzyme or the substrates, and it can also cause denaturation of the biocatalyst (Murray et al., 2014).

### 3.3.1 Reversible-3-step mechanism

A typical Michaelis-Menten equation describes the enzymatic rate as a function of substrate concentration for an irreversible reaction with a single substrate. Racemization reactions are in reality reversible processes (Schnell et al., 2003). Also, both substrate and product compete for the enzyme active sites and a second complex is formed between the enzyme and the product. The most complete version of the mechanism considers all the mentioned conditions. The following mechanism expression is written for the racemization reaction between enantiomers  $E_2$  (reaction substrate, undesired enantiomer) and  $E_1$  (reaction product, target molecule) catalyzed by the enzyme  $E$ :



The form of equation 3.13 represents a *reversible-3-step Michaelis-Menten* mechanism. In comparison to the mechanism shown in equation 3.1, the step of chemical transformation is separated from product release and both occur in a reversible manner. Therefore, two enzyme complexes are formed and both enantiomers can be converted into the other. The net changes in concentration of the intermediates  $EE_2$  and  $EE_1$  are:

$$\frac{dc_{EE_2}}{dt} = k_1 c_2 c_E - k_{-1} c_{EE_2} - k_2 c_{EE_2} + k_{-2} c_{EE_1} \quad (3.14)$$

$$\frac{dc_{EE_1}}{dt} = k_2 c_{EE_2} - k_{-2} c_{EE_1} - k_3 c_{EE_1} + k_{-3} c_E c_1 \quad (3.15)$$

Similarly to the previously discussed mechanism, a steady state assumption can be made for both enzyme-complexes and their value is set to zero:

$$\frac{dc_{EE_2}}{dt} = 0 \quad (3.16)$$

$$\frac{dc_{EE_1}}{dt} = 0 \quad (3.17)$$

The expressions can therefore be rearranged as:

$$c_{EE_2} = \frac{k_1 c_2 c_E + k_{-2} c_{EE_1}}{k_{-1} + k_2} \quad (3.18)$$

$$c_{EE_1} = \frac{k_2 c_{EE_2} + k_{-3} c_E c_1}{k_{-2} + k_3} \quad (3.19)$$

The total enzyme concentration (namely catalyst dosage) is in this mechanism the sum of the concentrations of free enzyme and that of the enzyme in each complex formation:

$$D_C = c_E + c_{EE_1} + c_{EE_2} \quad (3.20)$$

Hence, concentration of free enzyme  $c_E$  can be substituted in equations 3.18 and 3.19, that are rearranged are the following:

$$c_{EE_2} = \frac{k_1 c_2 D_C + (k_{-2} - k_1 c_2) c_{EE_1}}{k_{-1} + k_2 + k_1 c_2} \quad (3.21)$$

$$c_{EE_1} = \frac{k_{-3} c_L D_C + (k_2 - k_{-3} c_L) c_{EE_2}}{k_{-2} + k_3 + k_{-3} c_L} \quad (3.22)$$

The expressions for the concentrations of  $EE_2$  and  $EE_1$  are functions of the dosage and of the competing intermediate. Substituting  $c_{EE_1}$  in equation 3.21 and  $c_{EE_2}$  in equation 3.22 gives:

$$c_{EE_2} = D_C \frac{(k_{-2} + k_3) k_1 c_2 + k_{-2} k_{-3} c_1}{k_{-1} k_{-2} + k_{-1} k_3 + k_2 k_3 + (k_2 + k_{-2} + k_3) k_1 c_2 + (k_{-1} + k_2 + k_{-2}) k_{-3} c_1} \quad (3.23)$$

$$c_{EE_1} = D_C \frac{(k_{-1} + k_2) k_{-3} c_1 + k_2 k_1 c_2}{k_{-1} k_{-2} + k_{-1} k_3 + k_2 k_3 + (k_2 + k_{-2} + k_3) k_1 c_2 + (k_{-1} + k_2 + k_{-2}) k_{-3} c_1} \quad (3.24)$$

The rate of product formation for the forward reactions (consumption of  $E_2$ ) is:

$$\frac{dc_1}{dt} = k_3 c_{EE_1} - k_{-3} c_E c_1 \quad (3.25)$$

The concentration of free enzyme is substitute using equation 3.20:

$$\frac{dc_1}{dt} = -D_C k_{-3} c_1 + k_{-3} c_1 c_{EE_2} + (k_3 + k_{-3} c_1) c_{EE_1} \quad (3.26)$$

Replacing the rate equations 3.23 and 3.24 in equation 3.26:

$$\frac{dc_1}{dt} = D_C \frac{\frac{k_1 k_2 k_3}{k_{-1} k_{-2} + k_{-1} k_3 + k_2 k_3} c_2 - \frac{k_{-1} k_{-2} k_{-3}}{k_{-1} k_{-2} + k_{-1} k_3 + k_2 k_3} c_1}{1 + \frac{(k_2 + k_{-2} + k_3) k_1}{k_{-1} k_{-2} + k_{-1} k_3 + k_2 k_3} c_2 + \frac{(k_{-1} + k_2 + k_{-2}) k_{-3}}{k_{-1} k_{-2} + k_{-1} k_3 + k_2 k_3} c_1} \quad (3.27)$$

The previous equation can be simplified by defining the reaction parameters as the constants  $k_{E_1}$ ,  $K_{M_1}$ ,  $k_{E_2}$  and  $K_{M_2}$ :

$$\frac{dc_1}{dt} = D_C \frac{k_{E_2} c_2 - k_{E_1} c_1}{1 + \frac{c_2}{K_{M_2}} + \frac{c_1}{K_{M_1}}} \quad (3.28)$$

where:

$$k_{E_2} = \frac{k_1 k_2 k_3}{k_{-1} k_{-2} + k_{-1} k_3 + k_2 k_3} \quad (3.29)$$

$$k_{E_1} = \frac{k_{-1} k_{-2} k_{-3}}{k_{-1} k_{-2} + k_{-1} k_3 + k_2 k_3} \quad (3.30)$$

$$K_{M_2} = \frac{k_{-1} k_{-2} + k_{-1} k_3 + k_2 k_3}{(k_2 + k_{-2} + k_3) k_1} \quad (3.31)$$

$$K_{M_1} = \frac{k_{-1} k_{-2} + k_{-1} k_3 + k_2 k_3}{(k_{-1} + k_2 + k_{-2}) k_{-3}} \quad (3.32)$$

The rate equation scaled by the dosage is written as:

$$r_R = \frac{1}{D_C} \frac{dc_1}{dt} = \frac{k_{E_2} c_2 - k_{E_1} c_1}{1 + \frac{c_2}{K_{M_2}} + \frac{c_1}{K_{M_1}}} \quad (3.33)$$

Many enzymatic catalyzed reactions are favored to one direction of the equilibrium (Cornish-Bowden, 2012). This statement is also valid for racemization (Würges et al., 2009b).

Nevertheless, for simplification, both enantiomers are assumed to be converted at the same rate.

In this case, the parameters relative to each enantiomer must accept the same value:  $\frac{k_{E_2}}{k_{E_1}} = 1$

and  $\frac{K_{M_2}}{K_{M_1}} = 1$ . The racemization rate becomes the following:

$$r_R = \frac{k_{E_2}(c_2 - c_1)}{1 + \frac{c_1 + c_2}{K_{M_2}}} \quad (3.34)$$

Rearranging the parameters:

$$r_R = \frac{V_{max}(c_2 - c_1)}{K_M + c_1 + c_2} \quad (3.35)$$

where  $K_M = K_{M_2} = K_{M_1}$  and  $V_{max} = k_{E_2} K_M$ . This equation is related to the typical Michaelis-Menten expression shown in equation 3.12. Figure 3.9 illustrates concentration profiles modelled for both kinetic mechanisms using similar values of parameters  $V_{max}$  and  $K_M$ . The substrate can be fully converted to the product in the typical Michaelis-Menten mechanism, while for the reversible reaction an equilibrium plateau is achieved at equal concentrations of substrate and product (under assumption of isomerization reaction, in which the equilibrium is at the 50:50 mixture).

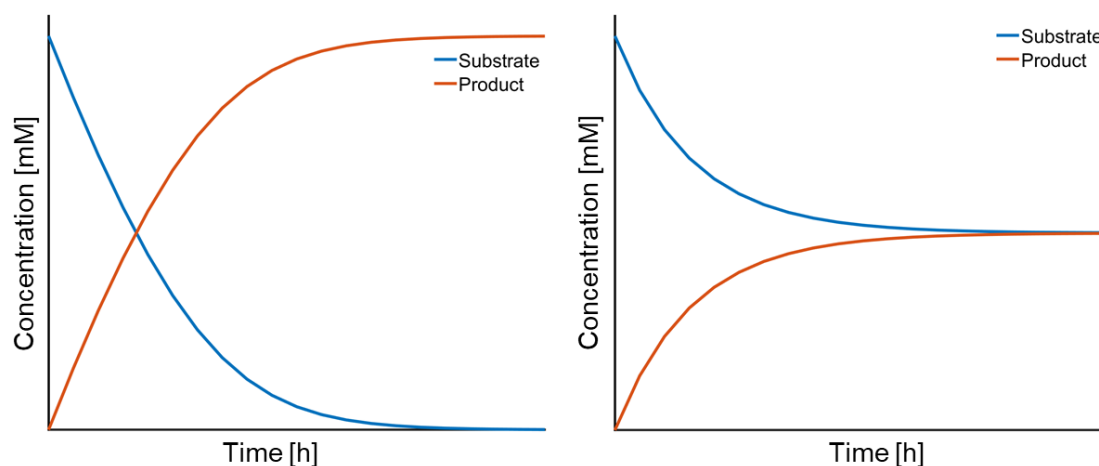


**Figure 3.9** Illustration of concentration profiles of enzyme catalyzed reactions with (left panel) irreversible and (right panel) reversible-3-step Michaelis-Menten mechanism (equations 3.12 and 3.35, respectively).

The irreversible reaction expressed in equation 3.12 becomes an appropriate simplification of equation 3.35 assuming very small concentrations of product ( $c_2 \gg c_1$ ). This approximation is useful to calculate the initial velocity, i.e. before concentration of target enantiomer  $c_1$  increases to a significant level, applied to estimate the kinetic parameters.

### 3.3.2 Inhibition effects

The enzyme kinetics may suffer inhibition effects that change the kinetic behavior of the biocatalyst. Substrate inhibition is a case of uncompetitive inhibition occurring in circa 20% of all known enzymes (Chaplin & Bucke, 1990). At high concentrations of substrate, more than one reactant molecule may bind to the biocatalyst, causing the complex to be reversibly inactive, decreasing the number of free enzyme molecules available. The kinetic parameter  $K_I$  must be introduced to the modelling of the enzymatic action.

$$r_R = \frac{V_{max}(c_2 - c_1)}{K_M + c_1 + c_2 + \frac{c_2(c_1 + c_2)}{K_I}} \quad (3.36)$$

The determination of the enzymatic parameters must be performed at initial reaction rate conditions, when the concentration of the product enantiomer is low and the reverse reaction is negligible. So, assuming the counter enantiomer as the substrate being consumed, equation 3.36 can be approximated as:

$$r_R = \frac{V_{max}c_2}{K_M + c_2 + \frac{c_2^2}{K_I}} \quad (3.37)$$

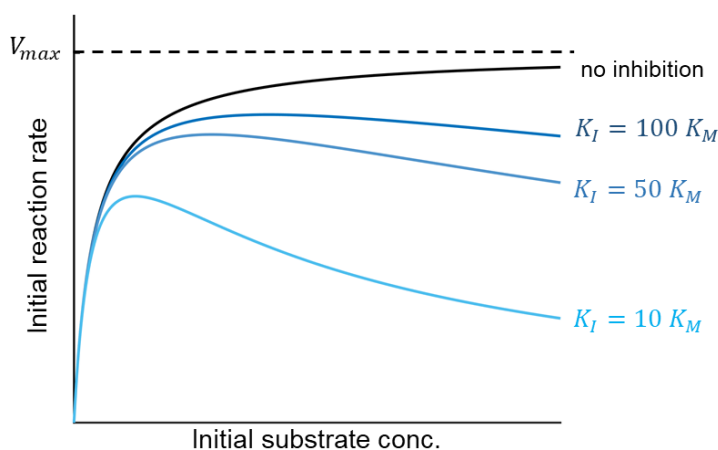


**Figure 3.10** Influence of substrate inhibition on the profile of initial reaction rate (equation 3.37). In all curves  $V_{max}$  and  $K_M$  are the same and the inhibition parameter  $K_I$  changes relative to  $K_M$ .

The parameter  $K_I$  represents the affinity of the enzyme to form the inhibition complex. Low values of  $K_I$  characterize significant influence of inhibition. High values of this parameter lead to kinetic behaviors more similar to the absence of inhibition. The relation between  $K_M$  and  $K_I$  accounts for the impact of the inhibition effects (Chaplin & Bucke, 1990). That influence can be seen in Figure 3.10, which depicts kinetic profiles without (in black) and with inhibition

in a range of  $K_I$  values (in blue). Higher  $K_I$  relative to the value of  $K_M$  results in alleviation of inhibition effects. The minimum value the ratio  $K_I/K_M$  can assume is the unit.

### 3.4 Types of enzymatic batch reactor

#### 3.4.1 Stirred tank reactor

The main characteristic of an ideal stirred tank batch reactor (BR) is the perfect mixing. This generates homogeneous concentration, so that at a fixed moment in time the reaction rate is independent from the position in the vessel (Figure 3.11). The BR operates in a non-stationary manner. In enzymatic reactions, a BR can be employed with both homogeneous and heterogenous catalysis. The general mass balance is given as:

$$\frac{dc_i}{dt} = \nu_i D_C r_R \quad i = 1,2 \quad (3.38)$$

The variable  $\nu_i$  is the stoichiometric coefficient of enantiomer  $i$ . For a racemization reaction,  $\nu_i$  corresponds to  $-1$  or  $1$  for reactant (being consumed) or product (being formed), respectively. The reaction rate  $r_R$  is the kinetic behavior particular to a pair enzyme-substrate under specific reaction conditions (e.g. temperature, solvent system). For a racemase,  $r_R$  can be described for instance by equations 3.35 or 3.36. The catalyst dosage  $D_C$  is the enzyme concentration, defined by the mass of free enzyme or immobilisate present in the reaction volume  $V_R$ :

$$D_C = \frac{m_{catalyst}}{V_R} \quad (3.39)$$

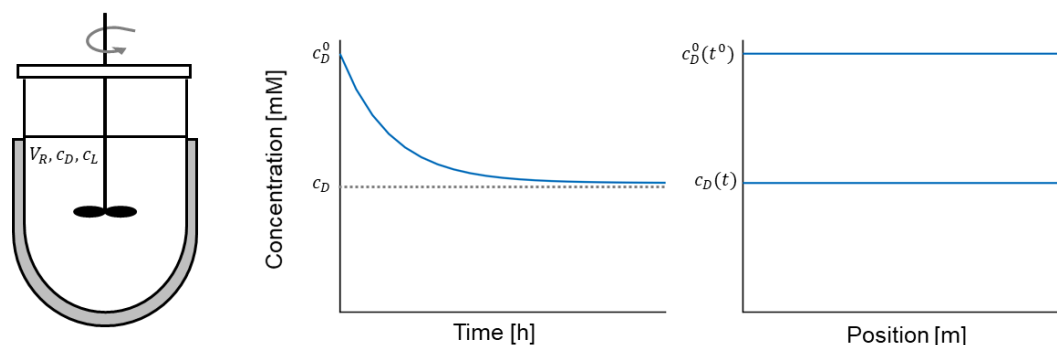


Figure 3.11 Schematic batch reactor and reactant concentration profile (adapted from (Rao et al., 2006)).

### 3.4.2 Packed bed reactor

Packed bed reactor is a classification from a flow reactor operating a heterogeneous reaction. In the case of enzymatic reactions, the column is packed with immobilized enzyme. Under steady-state conditions, the concentration in the reactor varies along its length (Figure 3.12). The amount of substrate decreases slowly over the size of the reactor. The general mass balance for a PBR can be written as:

$$u \frac{dc_i}{dz} = v_i D_C r_R \quad i = 1,2 \quad (3.40)$$

The variable  $u$  is the fluid velocity,  $z$  is the length of the reactor,  $v_i$  is the stoichiometric coefficient of enantiomer  $i$  and  $D_C$  is the biocatalyst dosage (concentration). The velocity  $u$  can be calculated as the volumetric flow rate  $\dot{V}$  over the reactor cross-sectional area  $A$ :

$$u = \frac{\dot{V}}{A} \quad (3.41)$$

For a constant area  $A$ , the differential reactor element volume is  $dV_R = Adz$ . Thus, equation 3.40 is rearranged as:

$$\dot{V} \frac{dc_i}{dV_R} = v_i D_C r_R \quad i = 1,2 \quad (3.42)$$

and further to:

$$\frac{dc_i}{d\tau} = v_i D_C r_R \quad i = 1,2 \quad (3.43)$$

where  $\tau = V_R/\dot{V}$  is the residence time. The mass balance for a PBR showed in equation 3.43 is analogous to that of a batch reactor described in equation 3.38.

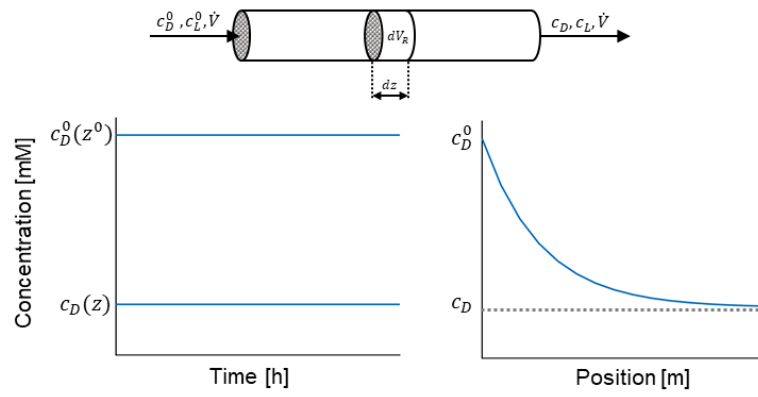


**Figure 3.12** Schematic packed bed reactor and reactant concentration profile at steady state conditions (adapted from (Rao et al., 2006)).

## 4 Experimental Section

In this chapter, the materials, analytical methods and experimental systems employed in the enzymatic investigations and in the validation of the shortcut model are described. The first part is dedicated to the introduction of the model system and their main physical and chemical properties: asparagine monohydrate as the model compound and the amino acid racemase as the model enzyme. Then, the materials and buffer solutions used are briefly summarized. The largest core of the present chapter contains detailed information about the methods, setups and analytics applied during experimental investigations. Most of the protocols described here are also reported in (Carneiro et al., 2019) and (Carneiro et al., 2020).

### 4.1 Model system

#### 4.1.1 Asparagine monohydrate

Asparagine (Asn) is a nonessential amino acid, as it occurs naturally in the human body. It plays an important role in the biosynthesis of proteins and muscle tissue, in the balance of the nervous system and in the eliminations of ammonia from the body (National Center for Biotechnology Information, n.d.). The asparagine molecule consists of an amino group, a carboxylic acid group and a carboxamide bound to the alpha carbon (Figure 4.1). It was the first amino acid to be isolated from a natural source: it was purified from asparagus juice, hence the compounds name. Asparagine is found naturally in in other foods, such as cheese, cocoa, potato, wheat, rye and corn. It is produced in the industry by means of direct fermentation and by purification as a by-product from potato starch production. It is used in supplementation and dietary imbalance, and it has been investigated in the treatment of leukemia (Chadwick, 1988).

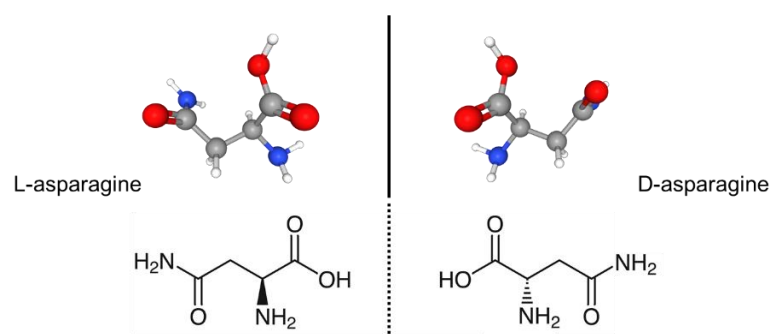


**Figure 4.1** Structure of asparagine enantiomers.

Asparagine is an optically active substance. Only the L-configuration participates in the human metabolism. The main interesting feature of this substance for the present study is that it crystallizes as a conglomerate. In the water, both enantiomers form stable white crystals which are monohydrated. There are no known polymorphs. Solubility data for the system asparagine monohydrate in water is found in literature. Petruševska-Seebach and coworkers reported solubility measurements for asparagine monohydrate in the range from 15 to 45 °C at several enantiomeric ratios (Petruševska-Seebach et al., 2009). The experimental data was later fitted to a polynomial expression as a function of temperature and concentration of the opposite enantiomer (Temmel et al., 2018):

$$w_{sat,k} = K_0 + K_1T + K_2T^2 + K_3 \frac{w_q}{1 - w_k - w_q} \quad k, q = L \text{ or } D - \text{Asn} \cdot \text{H}_2\text{O}; \quad k \neq q \quad (4.1)$$

$$K_0 = 0.0104; \quad K_1 = 1.0584 \times 10^{-4}; \quad K_2 = 2.4432 \times 10^{-5}; \quad K_3 = 0.0312$$

The parameters were determined with concentrations in mass fraction (g/g) and the temperature in degree Celsius. The equation parameters are identical for both stereoisomers due to the enantiomeric symmetry. The solubility curves of pure enantiomer and the racemic mixture based on equation 4.1 are depicted in Figure 4.2.

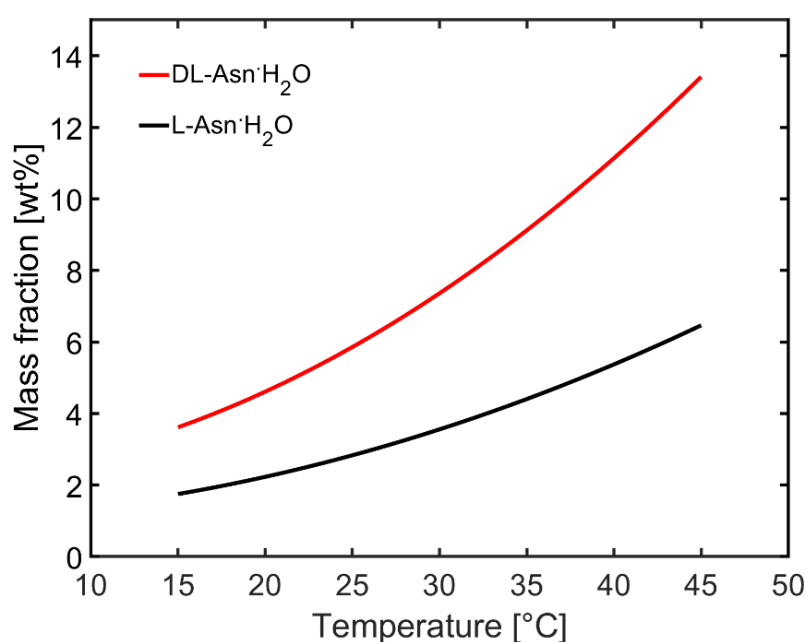


**Figure 4.2** Solubility of asparagine monohydrate in water. Plots from polynomial function (equation 4.1) from (Temmel et al., 2018).

Asparagine monohydrate presents solubility behavior nearly ideal, meaning that the solubility of the racemic mixture is practically double of that of pure enantiomer. As a

consequence, the solubility isotherms at different D/L compositions have similar slope and are parallel straight lines. In the temperature range showed in Figure 4.2, the solubility ratio (equation 2.4) of asparagine monohydrate is  $w_{ratio} = 2.07$ . This value was used to plot the solubility isotherm in the ternary phase diagram. That allowed the calculation of the driving force for PC from the crystallization temperature and the liquid phase composition. This methodology was employed in the shortcut model developed to simulate PC, as described in Chapter 6.

The solution density  $\rho_L$  of asparagine monohydrate in water is determined by the following empirical relation (Petruševska-Seebach, 2012):

$$\rho_L = \rho_{water} + 0.3572 w_{rac} \quad (4.2)$$

$$\rho_{water} = \frac{1}{0.9999 + 4.911 \times 10^{-6}(T - 273.15)^2}$$

where  $w_{rac}$  is the mass fraction of DL-asparagine in g/g,  $T$  is the temperature in K, and  $\rho_{water}$  is the density of water in g/cm<sup>3</sup>, which is used as reference.

#### 4.1.2 Amino acid racemase

The model enzyme used in the present investigations was an amino acid racemase (AAR). The Enzyme Commission Number of this biocatalyst is EC 5.1.1.10. It is naturally occurring in the microorganism *Pseudomonas putida* KT2440 (Radkov & Moe, 2013). The enzyme is encoded into the plasmid system pET-22b(+), so it can be overexpressed in *Escherichia coli* BL21 (DE3) under the control of the inducer isopropyl- $\beta$ -D-thiogalactopyranosid (IPTG) (Würges et al., 2009b). The racemase grows well in the LB cultivation medium, which is a complex medium, with components such as yeast hydrolysates enriched with glucose for energy sources. The racemase is secreted within the cell, therefore it requires cell harvesting and lysis to be used.

The AAR has a broad substrate specificity and it uses PLP (pyridoxal 5-phosphate) as a cofactor to express its catalytic properties (Schnell et al., 2003). It is a dimeric protein, each monomer having a molecular weight of circa 44 kDa (Würges et al., 2009b). It presents the strongest reaction rates for the enantiomers of the amino acid lysine (Lim et al., 1993; Radkov & Moe, 2013; Wuerges, 2011). With asparagine monohydrate as substrate, the enzyme has been reported to be active from at least 20 to 50 °C, with temperature optimum at 47.5 °C

(Petruševska-Seebach et al., 2009). Above 50 °C the activity presents a strong decrease, likely due to denaturation. The thermostability of the AAR also varies. The half life of this racemase at 20 °C is approximately 20 days, and between 30 and 40°C is approximately a week. The optimum pH-value is towards the basic side, between 8.6 and 9.7 (Wuerges, 2011).

Prior to the experiments reported here, a C-terminal polyhistidine-tag was added to the model enzyme to facilitate purification. The construction was performed by Dr. Katja Bettenbrock, from the ARB Group at the Max Planck Institute in Magdeburg. The PCR-based protocol was described in ref (Carneiro et al., 2020).

## 4.2 Materials

### 4.2.1 Reagents and immobilization supports

Racemic DL-asparagine monohydrate (purity  $\geq 99\%$ ) used for preferential crystallization experiments was purchased from Sigma-Aldrich Chemie GmbH. L-asparagine monohydrate (purity  $\geq 99\%$ ) used to prepare seeds for the crystallization experiments was supplied from Acros Organics (Thermo Fisher Scientific). Substrates used for enzymatic were D-asparagine monohydrate (purity  $\geq 99\%$ ) purchased from Alfa Aesar (Thermo Fisher Scientific) and the above-mentioned L-asparagine monohydrate. The same asparagine reagents were used for calibration of analytic methods.

Isopropyl-beta-D-thiogalactopyranoside (IPTG) used for protein induction was obtained from Carl Roth GmbH and Co. KG. The protease inhibitor cocktail set VII from Calbiochem used prior to cell lysis was purchased from Merck KGaA. The racemase cofactor pyridoxal 5'-phosphate monohydrate (PLP) was purchased from Sigma-Aldrich.

The carrier materials from Lifetech ECR were kindly donated by SpinChem AB and Purolite®. The enzyme support Eupergit® CM was purchased from Sigma-Aldrich. The suppliers from affinity carriers A, B and C was omitted due to conflict of interest.

The water used as solvent during all experiments was purified by Milli-Q gradient system from Millipore Corporation.

### 4.2.2 Buffers

The buffer solutions were prepared according to the needs of molarity, pH and ionic strength of each application. The buffers used along the experimental investigations of this work are listed below.

**Table 4.1** List of buffers used in enzyme purification and immobilization.

Buffer	Composition	pH	Application
B1	20 mM phosphate ( $\text{Na}_2\text{HPO}_4/\text{NaH}_2\text{PO}_4$ ) 500 mM NaCl	7.4	Cell lysis, equilibration of purification column and immobilization
B2	20 mM phosphate ( $\text{Na}_2\text{HPO}_4/\text{NaH}_2\text{PO}_4$ ) 500 mM NaCl 15 mM imidazole	7.4	Washing of nonspecific binding proteins during purification
B3	20 mM phosphate ( $\text{Na}_2\text{HPO}_4/\text{NaH}_2\text{PO}_4$ ) 500 mM NaCl 300 mM imidazole	7.4	Elution of protein during purification
B4	20 mM phosphate ( $\text{Na}_2\text{HPO}_4/\text{NaH}_2\text{PO}_4$ ) 500 mM NaCl	8.0	Immobilization
B5	1.0 M phosphate ( $\text{K}_2\text{HPO}_4/\text{KH}_2\text{PO}_4$ )	7.4	Immobilization
B6	0.5 M phosphate ( $\text{Na}_2\text{HPO}_4/\text{NaH}_2\text{PO}_4$ )	7.4	Immobilization

### 4.3 Preferential Crystallization setup and procedures

The experimental setup for preferential crystallization consisted of a 0.2 L double jacketed stirred tank equipped with a Pt-100 sensor for temperature control. A constant stirring rate of 280 rpm was set using an overhead stirrer (Heidolph RZR 1, Heidolph Instruments GmbH & CO. KG) with a three-blade impeller (Heidolph PR 30). An illustration of the experimental system is given in Figure 4.3. An important part of the procedure is monitoring the crystallization process. Following the changes in optical rotation is an adequate and simple method to continuously track the progress of preferential crystallization. Each enantiomer of a pair has a specific magnitude of optical rotation but of opposite signs. The net signal measured is proportional to the difference in concentration between both molecules. PC starts at the racemic mixture, where the enantiomers have the same concentration and the net optical rotation is zero. During the process, the signal changes, reaches a maximum and, if let to reach equilibrium conditions, attains zero again. During the experiments the solution was monitored by pumping crystal free solution to a polarimeter (MCP 500 Modular Circular Polarimeter, Anton Paar; cuvette of 100 mm length and 2.0 ml volume) and analyzed at wavelength 365 nm

(see Figure 4.3). The flowrate was set to 20 ml/min (peristaltic pump, Heidolph PD 5201 SP Quick). Sintered glass filters were used to avoid transport of solids. Both the stream and the polarimeter were thermostated above the saturation temperature to avoid nucleation and crystal growth. The polarimeter was calibrated before the procedures.

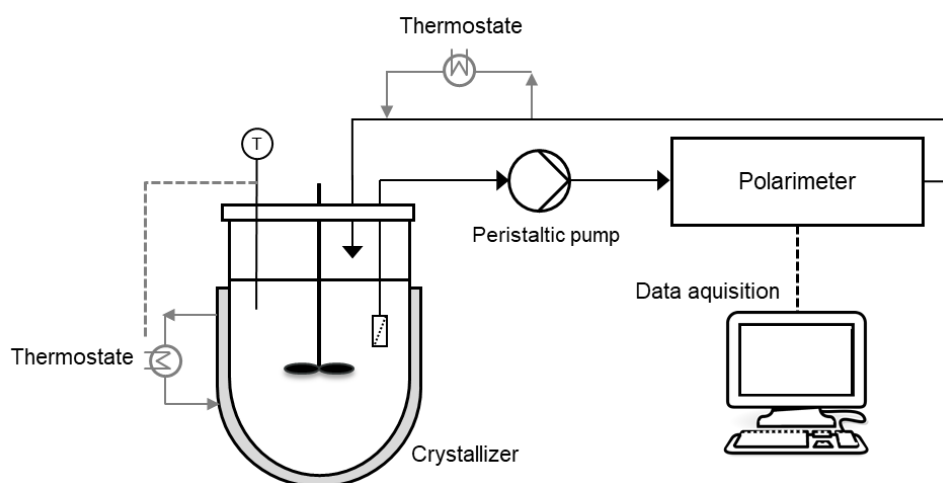


**Figure 4.3** Scheme of experimental setup used during preferential crystallization investigations.

Prior to each experiment the racemic asparagine solution was prepared outside the crystallizer, kept at the saturation temperature ( $T_{sat}$ ) and filtrated to assure complete dissolution of solids. The mother liquor was then transferred to the crystallization vessel and cooled down to the crystallization temperature. When achieving  $T_{cryst}$ , the solution was seeded with 0.2 g of L-asparagine monohydrate sieved to the fraction 90 – 125  $\mu\text{m}$ , prepared with the Sieve shaker AS 200 digit (Retsch). The conditions particular to each experiment are specified in the experimental evaluation of the shortcut model (Chapter 6, Table 6.1).

#### 4.4 Overexpression of amino acid racemase

The His-tagged amino acid racemase was overexpressed in *Escherichia coli* BL21 (DE3) in 12 L batch fermentation. An illustration of the steps necessary for AAR overexpression is given in Figure 4.4. Two pre-cultures were performed before the main cultivation. First, a single cell colony is grown in 5 mL LB medium with 0.1 g/L ampicillin at 37 °C for 8 h. From that solution, 2 mL were transferred to grow in 200 mL of the same medium enriched with 2 g/L glucose and 2.5 mM  $\text{CaCl}_2$  at 37 °C for 16 h. Finally, the last pre-culture was used to inoculate the medium in 12 L stainless steel bioreactor Biostat C (B. Braun Biotech) equipped with PCS7 control system from Siemens. The starting  $\text{OD}_{650\text{nm}}$  was 0.065. The culture grew at 30 °C in LB medium enriched with 0.1 g/L ampicillin, 10 g/L glucose, 2.5 mM  $\text{CaCl}_2$ .

To induce the expression of the AAR, 0.1 mM isopropyl-b-D-thiogalactopyranoside (IPTG) was added at optical density  $OD_{650nm} \approx 1.0$ . The temperature was set to 22 °C and the cells grew until  $OD_{650nm} \approx 2.8$ . The cell suspension was then fractionated, harvested by centrifugation (5000 g, 50 min, 4 °C) and stored at -20 °C. When needed, the frozen cell pellets were resuspended in the desired purification or immobilization buffer. Protease inhibitor (0.1 ml/g-wet pellet) and DNase I were added to avoid protein breakdown and reduced viscosity caused by chromosomal DNA, respectively. The cells were disrupted either by sonication (Ultrasonic cell disruptor 450d, Branson; amplitude 65%, cycles of 0.5 s and 12 s break, 3 min pulse time) followed by centrifugation at 17000 g (4 °C, 30 min), or by high-pressure homogenization (EmulsiFlex-C5, Avestin Inc.) over maximum pressure drop of 2500 psi, followed by centrifugation at 25000 g (4 °C, 20 min). All disruption procedures were made on ice. Finally, AAR cofactor pyridoxal 5'-phosphate (PLP) was added to achieve a concentration of 50  $\mu$ M. The supernatant of the crude extract (CE) was stored at 4°C. CE was the starting material for purification and immobilization procedures with affinity carriers.

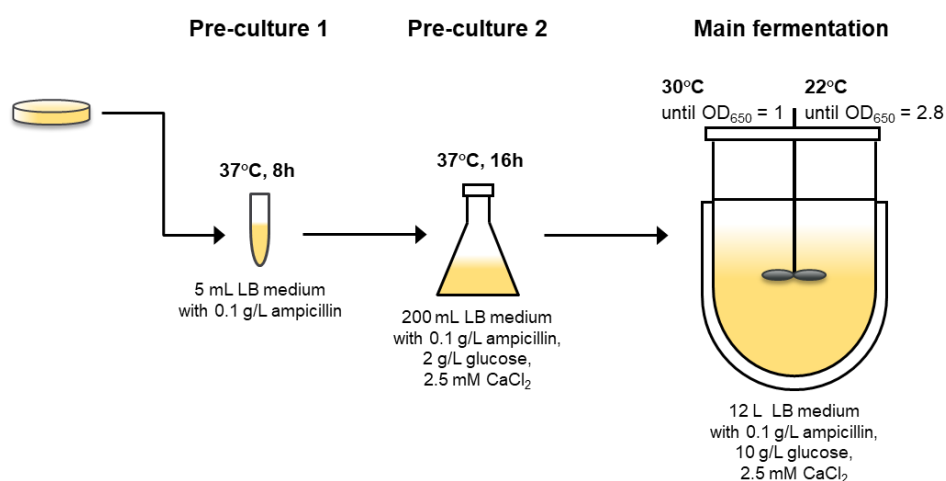


**Figure 4.4** Steps for amino acid racemase overexpression.

The temporal growth of biomass in the 12 L fermentation is shown in Figure 4.5. The time necessary for fermentation to achieve the desired final cell density was about 8 hours. The total time required for pre-cultures and main fermentation and cell harvesting is 2 days. Two extra days are needed for preparation and cleaning. The AAR overexpression yielded ca. 4.5 g of wet pellet (cell biomass) per liter of cultivation medium. The pellets resulted in approximately 69 mg of total protein per gram of pellet.

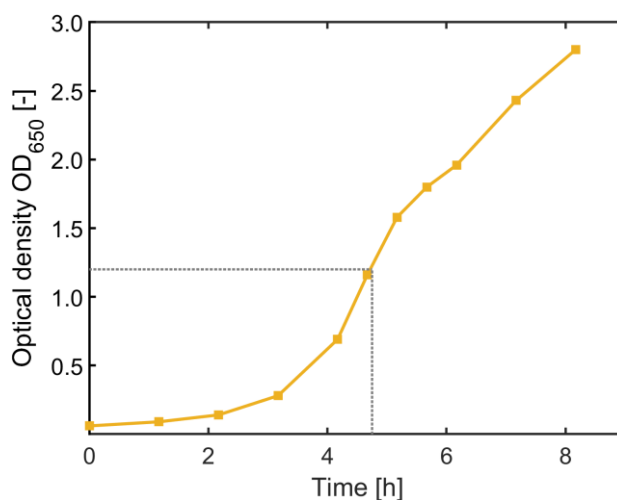


**Figure 4.5** Progress of biomass during main fermentation for production of the amino acid racemase. Symbols are measured data, solid lines are guides to the eye. Dotted line marks the addition of IPTG for induction of protein overexpression.

## 4.5 Purification of amino acid racemase

The recombinant amino acid racemase was purified by metal ion affinity chromatography (IMAC). Purification was carried out at 4°C in a Ni-NTA 5 mL chromatography column (HisTrap FF crude, GE Healthcare) connected to an Äkta system (Purifier 25, GE Healthcare).

The cells were previously disrupted in buffer B1 (see Table 4.1) following the protocols mentioned above. The affinity column was first equilibrated with 5 column volumes (CV) of buffer B1 at 3 ml/min. After loading the CE solution at 1.0 ml/min, the column was washed with 11 CV of buffer B2 at 1.5 ml/min to wash away the non-bound proteins. The AAR was recovered by stepwise gradient elution at 1.0 ml/min with buffers B1 and B3: 2 CV from 0 to 65% B3, followed by 2 CV at 65% B3 and 2 CV from 65 to 100% B3. The purified fractions were evaluated by SDS-PAGE analysis. Protein concentrations were determined using Bradford method as described in section 4.11.

The purification yielded in average 4.1 mg of AAR per g pellet disrupted. The analytical data for the purification steps is summarized in Table 4.2. The amount of protein is calculated from the solution volume and protein concentration. The activity is measured experimentally, and together with protein concentration gives the specific activity values. The purification factor represents how many times the specific activity increased compared to that of the starting material. The specific activity increased significantly after purification.

**Table 4.2** Summary of purification of the amino acid racemase. The activity was measured with 167 mM D-Asn at 30 °C. The purification factor is the change in specific activity relative to cell extract.

Step	Volume [ml]	Protein conc. [mg/ml]	Amount total protein [mg]	Activity [ $\mu\text{mol}/\text{min}/\text{L}$ ]	Specific activity [ $\mu\text{mol}/\text{min}/\text{mg}$ ]	Purification factor
Cell extract	84	14	1201	167	0.8	
IMAC	15	4.5	68	558	20	25
Buffer exchange	4.1	11	43	570	16	20

## 4.6 Immobilization of amino acid racemase

Prior to immobilization on covalent binding supports, the purified AAR solution was concentrated using Vivaspin 15 (Sartorius AG) and the buffer was exchanged to a suitable immobilization buffer using Zeba™ Spin desalting columns of 5 mL with 7K MWCO (Thermo Fischer Scientific). Buffer exchange is a necessary step because it eliminates imidazole present in the elution buffer B3 used during purification. In this procedure, the enzyme solution is also concentrated to achieve the suitable conditions of enzyme load for immobilization. Results regarding the step of buffer exchange are given in Table 4.2. Only a fraction of the purified solution was used. The buffer exchange and concentration resulted in 18% and 20% loss in amount of enzyme and specific activity, respectively.

Six immobilization supports were studied for the immobilization of the AAR: three affinity-binding supports, in which the immobilization was performed directly from the CE, and three supports providing covalent binding, in which purified protein solution was used. Table 4.3 summarizes the properties of the investigated adsorbents.

**Table 4.3** Summary of the immobilization support used with AAR and their physical characteristics.

Immobilization support	Type of binding	Binding group	Particle size [ $\mu\text{m}$ ]	Pre-activation	AAR solution
A <sup>a</sup>	affinity	chelated Fe <sup>3+</sup>	75 – 125	no	crude extract
B <sup>a</sup>	affinity	chelated Fe <sup>3+</sup>	75 – 125	no	crude extract
C <sup>a</sup>	affinity	chelated Fe <sup>3+</sup>	75 – 125	no	crude extract
Eupergit CM	covalent	epoxy	50 – 300	no	purified
Purolite ECR 8204	covalent	epoxy	150 – 300	no	purified
Purolite ECR 8309	covalent	amino	F: 150 – 300 M: 300 – 710	yes	purified

<sup>a</sup>The official names and manufacturers were omitted.

The enzyme immobilization strategy was investigated using porous carriers of affinity and covalent binding. Table 4.3 summarizes the properties of the investigated adsorbents for AAR immobilization. Changes in color of the solution were observed during successful immobilization procedures. Concentrated solutions of the racemase are of a bright yellow color due to the presence of the cofactor PLP bound to the active site of the AAR. Upon effective immobilization, the supports acquired a light yellow color and the remaining solution became colorless (see Figure 4.6).

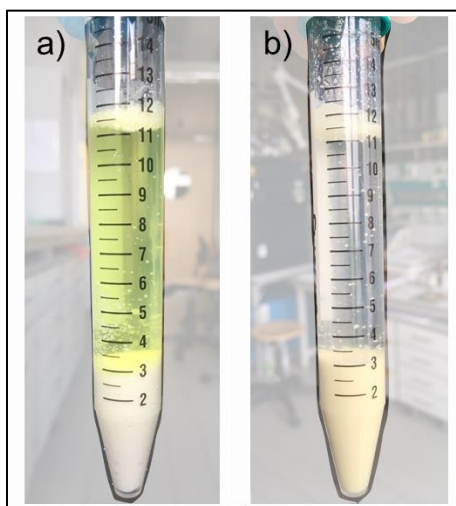


**Figure 4.6** Changes in color during AAR immobilization. Liquid phase is the purified enzyme solution and solid phase is the immobilization support (a) before and (b) after incubation time.

Immobilization of the amino acid racemase was evaluated by the specific activity (see section 4.7) and immobilization yield  $Y_{im}$ . The immobilization yield was calculated based on measurements of protein quantification (details of analytics in section 4.11). The amount of protein bound to the immobilization support ( $m_{protein}^{bound}$ ) was determined as the difference between the amount of protein in the initial AAR solution and residual protein in supernatant and washing solutions after immobilization. The yield was calculated as the ratio between the mass of protein bound to the support and the initial mass in solution ( $m_{protein}^0$ ) before immobilization (equation 4.3). In addition, immobilization was evaluated qualitatively with SDS-PAGE analysis.

$$Y_{im} [\%] = \frac{m_{protein}^{bound}}{m_{protein}^0} \times 100 \quad (4.3)$$

### Immobilization on affinity supports

Cell pellets were disrupted in buffer B1 or B4 (see Table 4.1) by ultrasonication according to the procedure described in section 4.4. CE solution with a total protein concentration 16 – 18 mg/mL was added to 0.25 mg of support to generate a specific incubation load. The immobilization was performed at room temperature for 30 min in a rotating mixer and for 15 min standing without mixing. After that, the supernatant was removed by pipetting. The support with immobilized protein was washed in vacuum filtration with the same buffer used for cell lysis. Both the supernatant and the washing solution were collected for protein quantification.

All three carriers were tested in buffer B4 (pH 8.0) and an incubation load of 250 mg-protein/g-support. The influence of pH (7.4 and 8.0, respectively buffers B1 and B4) and incubation load (250 and 667 mg-protein/g-support) on carrier B were evaluated.

### Immobilization on Eupergit CM

Purified AAR solution of concentration 1 mg/mL in buffer B5 was added to dry support for protein load of 27 and 37 mg-protein/g-support. The slurry was incubated at room temperature for 72 h in a rotating mixer. The support with immobilized enzyme was filtrated and the filtrate was collected for analysis of enzyme concentration. The support with immobilized enzyme was washed with 10 mM potassium phosphate buffer pH 7.4 and the uncoupled binding sites were blocked in a solution of 50 mM glycine for 1 h.

### Immobilization on Purolite ECR 8204

The support was first washed with buffer B1 for equilibration and then filtered with vacuum filtration. After, 1 mL of purified AAR in buffer B6 was incubated with 0.25 g of wet support at protein load of 25 and 35 mg-protein/g-support. The slurry was put in a rotating mixer for 18 h at room temperature and subsequently left without mixing for 20 h. The liquid phase was filtrated and collected for analysis. The immobilized AAR support was washed with buffer B1. The supernatant and washing solution were collected for analysis.

### Immobilization on Purolite ECR 8309

The support was equilibrated with buffer B1 and filtered. Resin activation was carried out by adding buffer B1 containing 2% (w/v) glutaraldehyde at a resin/buffer ratio of 1/4 (w/v) for 1.5 h in a rotating mixer. After filtration, 0.25 g of wet activated support was incubated with 1 mL of purified AAR solution in buffer B1 for 18 h at room temperature. The following

incubation loads were tested: 4.2, 25, 35 and 50 mg-protein/g-support for ECR 8309F and 4.2 mg-protein/g-support for ECR 8309M. If needed, the initial protein solution was diluted in buffer B1 to achieve the desired load and resin/buffer ratio of 1/4 (w/v). After incubation, the AAR immobilisate was filtrated and washed with buffer B1. The filtrate and washing solution were analyzed to determine the remaining protein content.

The same immobilization procedure was followed using 2.2 g support at incubation load of 35 mg-protein/g-support. Part of the immobilisate was applied to pack the flow reactor column and another part was used for analysis.

## **4.7 Enzyme activity**

### **4.7.1 Activity assay of free protein**

#### **4.7.1.1 Polarimetric method**

AAR activity was determined by mixing the typically 50 – 100  $\mu$ L of protein solution with 3 g of substrate solution and rapidly injecting it into a polarimetric cell (MCP 500 Modular Circular Polarimeter, Anton Paar). Standard measurements were taken at 30 °C with D-asparagine monohydrate 2.5 wt% (167 mM) as substrate. The racemization was tracked by monitoring the changes in optical rotation at wavelength 365 nm. For quantification, a calibration curve was determined for asparagine monohydrate prior to the experiments.

#### **4.7.1.2 Chromatographic method**

The effect of enzyme dosage on racemization was measured by chromatography instead of polarimetry. High enzyme concentrations interfere with the optical rotation, making the signal deviate from its linear profile. In the HPLC method, the reactions were performed in Eppendorf vials placed in a Eppendorf Thermomixer (Eppendorf AG) at 30°C and 1000 rpm by adding purified enzyme solution to 1 mL of substrate (2.5 wt% D-Asn·H<sub>2</sub>O). The AAR concentrations investigated were 20, 100 and 400 mg-protein/L. The reaction was terminated at varying times (until 20 minutes) by diluting the reaction media in perchloric acid pH 1.0 at ratio 1:9. The reaction compositions were analyzed by HPLC analysis described in section 4.11.2.

### 4.7.2 Kinetics of free AAR

Kinetic constants of purified enzyme were measured via polarimetric method (section 4.7.1.1) at 30, 35 and 40°C by adding AAR solution at the dosage 30 mg-protein/L to 3 g of substrate solution of varying concentrations (0.11 and 5.0 wt% D-Asn monohydrate, equivalent to 7.6 - 333 mM). All measurements were repeated twice and the kinetic parameters were estimated by nonlinear regression using OriginLab 2019.

The effect of enantiomeric excess in the enzymatic activity was investigated by adding free AAR at 20 mg-protein/L to 3 g of substrate solution at 30, 35 and 40°C. D-asparagine solution was prepared at concentrations close to the solubility limit at each respective temperature: 3.2, 4.4 and 5.3 wt%. L-asparagine monohydrate was added to create the desired enantiomeric excesses ( $ee = 5, 10, 20\%$ ).

### 4.7.3 Activity assay of immobilized AAR

Activity of immobilized AAR was determined by adding 20 mg of enzyme immobilisate (40 mg in case of Eupergit CM) to 1 mL of D-Asn·H<sub>2</sub>O solution 2.5 wt% (167 mM) in 2 mL Eppendorf vials. The suspension was placed in an Eppendorf Thermomixer (Eppendorf AG) at 30 °C and 1000 rpm for 2, 4, 6 and 8 min. The reaction was terminated by filtration of the reaction media with Rotilabo PET-membrane syringe filters of pore size 0.45 μm and diameter 25 mm (Carl Roth GmbH + Co. KG). All measurements were repeated twice. The solution compositions were analyzed by HPLC (see protocol in section 4.11.1).

## 4.8 Recycling of immobilized AAR

The reusability test was performed with immobilized AAR to estimate the binding stability during prolonged use. The procedure was similar to the activity test, but repeated for 6 cycles. The amount of 40 mg of immobilized protein reacted with 1 mL of D-Asn monohydrate solution 2.5 wt% at 30°C for 30 minutes. Afterwards, the suspension was allowed to sediment for some seconds and the liquid phase was carefully removed with a syringe connected to a Rotilabo PES filter (Carl Roth GmbH + Co. KG). Subsequent cycles were performed using the same immobilized support and reaction vial, following the same protocol. After each cycle the optical rotation of the resulting solution was measured in the polarimeter and the final solution composition and the conversion were calculated.

## 4.9 Kinetics of immobilized AAR in batch reactor

The kinetics of immobilized enzyme were assayed at a larger scale than the standard activity test described in section 4.7.2. The investigation was carried out at 40°C in 50 mL double jacket reactor (Double Sidearm Celstir Spinner Flask with screw caps 54x147 mm, Wheaton, DWK Life Sciences Inc.) equipped with overhead magnetic stirrer at 300 rpm. The amount of 0.4 g of wet support (ECR 8309F, 35 mg-protein/mg-support) was added to 50 mL D-asparagine solution in a range of concentrations (0.11 – 5.0 wt%, equivalent to 7.6 – 333 mM). Online monitoring of the reaction was obtained by pumping the solution (Heidolph PD 5201 SP Quick, Heidolph Instruments GmbH & CO. KG) at 8 mL/min through a polarimeter. The pipeline was insulated to avoid heat exchange. Sintered glass filters were used to prevent removal of carrier material from the reactor. Between the batches, the immobilized enzyme was carefully washed with distilled water and filtered. Each measurement was repeated twice. The kinetic parameters were estimated by nonlinear regression using OriginLab 2019.

## 4.10 Steady-state racemization in packed bed reactor

A Tricorn column 5/100 (GE Healthcare) was packed with immobilized AAR (carrier ECR 8309F, 35 mg-enzyme/g-support). The resulting packing conditions are summarized in Table 4.4. The column porosity was estimated by injection of an inactive sample (20  $\mu$ L of ethanol and water 50:50 (v/v)) at 1.0 ml/min in the presence and in the absence of the column. The peaks were recorded with UV/Vis detector at wavelength 210 nm. The measurements were performed in duplicate. The porosity was calculated by  $\varepsilon = t_{dead}\dot{V}/V_{bed}$ , where  $\varepsilon$  is the porosity,  $t_{dead}$  is the difference between retention times in the presence and absence of the packed reactor,  $\dot{V}$  is the volumetric flow rate and  $V_{bed}$  is the volume of the bed.

**Table 4.4** Summary of the AAR packing conditions and column limits.

Parameter	Value	Unit
Bed height	10.8	cm
Bed volume	2.12	ml
Bed sectional area	0.196	cm <sup>2</sup>
Mass of immobilized AAR	1.84	g-support
Dosage	0.87	g-support/ml
Porosity	0.86	-
Pressure limit	100	bar

The reactor performance was investigated under steady-state conditions. The PBR was connected to an Agilent Technologies 1100 HPLC system with a column oven set at 40°C (see Figure 4.7a). The substrate solutions were pumped continuously through the reactor at varying flow rates ranging from 0.1 – 3.5 mL/min until equilibrium was reached. The steady-state was verified by the formation of a plateau in the signal of UV/Vis detector. The experimental set up is illustrated in Figure 4.7b. Outlet flow samples of the were collected and analyzed by chiral chromatography as described in section 4.11.1. The feed solutions were 2.5 wt% of pure D-Asn monohydrate and of DL-Asn mixture with 5% enantiomeric excess.

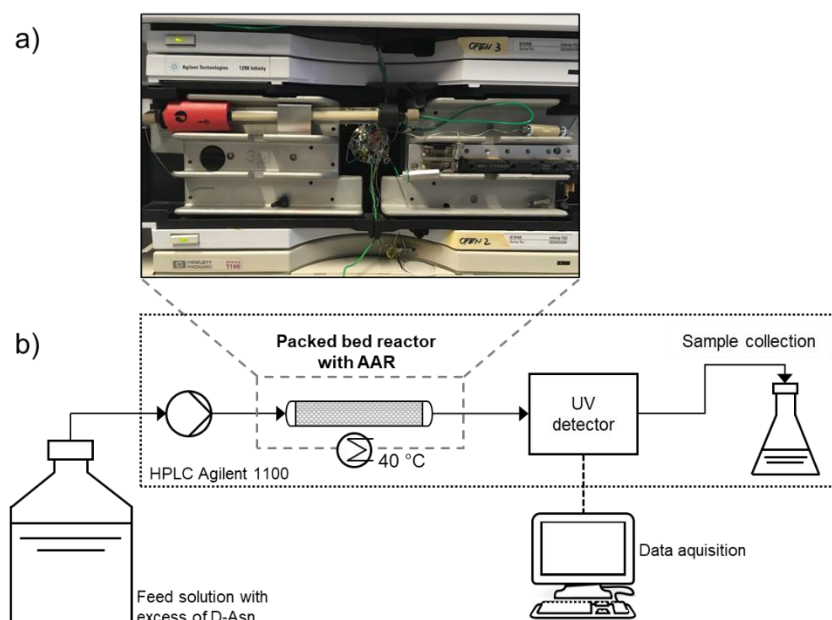


**Figure 4.7** a) Flow reactor packed with AAR attached to the HPLC system. b) Schematic experimental setup for PBR experiments. Feed with excess of D-asparagine converted into L-asparagine by the immobilized racemase.

## 4.11 Analytics

### 4.11.1 Chromatography analysis

To determine asparagine concentration and composition from crystallization or enzymatic reactions, solutions were analyzed in a Dionex UltiMate 3000 HPLC system (Thermo Fischer Scientific Inc.) equipped with Crownpak CR (+) column (150×4.0 mm; Daicel corporation, Chiral Technologies Europe SAS). The chiral separation was performed at 5°C. The mobile phase was perchloric acid pH 1.0, pumped at a flow rate 0.4 mL/min. The sample injections were of 1 µL measured with UV/Vis detection at 200 nm.

#### **4.11.2 Protein quantification**

Protein concentration from cell extract, fractions of the purification and immobilization process was measured by the Bradford method (Bradford, 1976). Bovine serum albumin (BSA) was used as reference standard. Typical linear calibration curves were constructed with BSA concentration ranging from 0 to 500 mg/L. Measurements were performed by mixing 20  $\mu$ L of sample with 1.0 mL of Bradford reagent and analyzed in UV/Vis-spectrophotometer (Ultrospec 3000, Pharmacia Biotech) at 595 nm.

## 5 Characterization and Application of an Enzymatic Reactor

The majority of the results discussed in this chapter were published in the journal *Engineering in Life Sciences* (2020, 20(12), 550–561) under the title “*Immobilization of an amino acid racemase for application in crystallization-based chiral resolutions of asparagine monohydrate*” (Carneiro et al., 2020). The immobilized racemase reported in this work was also studied for its use on temperature cycling induced deracemization, in a collaboration with Kritsada Intaraboonrod and Prof. Adrian Flood from the Vidyasirimedhi Institute of Science and Technology in Thailand. A brief summary of the results obtained during their study is mentioned at the last section of the present chapter. More details can be found on *Crystal Growth and Design* (2020, 21(1), 306–313), “*Temperature Cycling Induced Deracemization of dl-Asparagine Monohydrate with Immobilized Amino Acid Racemase*” (Intaraboonrod et al., 2020).

The results of the experimental study conducted with the enzyme and its application in a bioreactor are described here. Details on production and purification of the C-terminal histidine-tagged amino acid racemase EC 5.1.1.10 from *P. putida* KT2440 are given in sections 4.4 and 4.5. In the present chapter, the kinetic results and the characterization of the racemase regarding temperature, dosage and enantiomeric excess are presented. Then, the investigation of immobilization conditions and type of support with focus on catalyst activity and stability is showed. To evaluate the use of the racemase for the desired coupling, the AAR behavior was studied under conditions observed during PC experiments (showed in Chapter 6). The behavior of the immobilized amino acid racemase in fixed bed reactor under unfavorable driving forces conditions are quantified using experiments and modeling. A final outlook of the coupling of PC and racemization contains important insights and prospects of process configuration and applications.

### 5.1 Kinetics of free enzyme

The velocity of an enzyme-catalyzed reaction depends upon the substrate concentration. The rate of racemization is described by a reversible three-step Michaelis-Menten kinetics. Details on the mechanism and the rate equations were discussed in Chapter 3. The model reactant was asparagine in water, the same system used for experimental validation of the

shortcut model (Chapter 6). The initial reaction rates of pure free AAR were determined at different initial concentration of pure D-Asn ranging from 8 to 330 mM measured at 30, 35 and 40 °C and constant dosage  $D_C = 30$  mg/L. The results are showed in Figure 5.1.

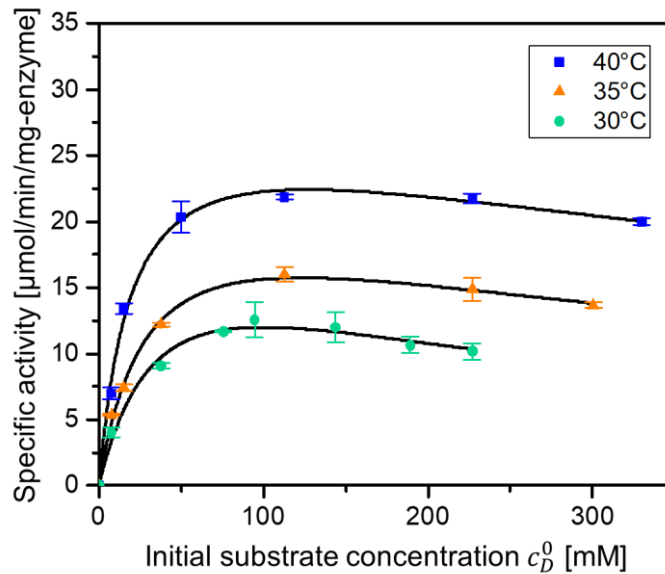


**Figure 5.1** Reaction kinetics of purified free AAR at different temperatures. Symbols are experimental data and solid curves are the respective kinetic function (equation 3.36) with the estimated parameters (see Table 5.1). All experiments were performed in duplicate.

The three kinetic profiles showed similar a trend, in which the initial rate values reach a maximum before dropping at higher concentrations of reactant. This behavior suggests an inhibition effect, described by equation 3.36. The parameters of maximum velocity  $V_{max}$ , the Michaelis constant  $K_M$  and the inhibition constant  $K_I$  were estimated for each temperature by non-linear regression and the results are presented in Table 5.1. The respective model curves are shown in Figure 5.1. The free AAR kinetic behavior was well described by the rate equation accounting for substrate inhibition. The overall specific activity increases at higher temperatures. This is expected for all catalytic reactions in case there is no denaturation or degradation caused by temperature. All individual rate constants that contribute to the mechanism (that is,  $k_1$ ,  $k_{-1}$ ,  $k_2$ ,  $k_{-2}$ ,  $k_3$ ,  $k_{-3}$  in equation 3.13) vary independently with temperature, resulting in changes in the kinetic parameters (Chaplin & Bucke, 1990). The improvement in activity at higher temperatures is expressed by the increase of  $V_{max}$  values. The values of  $K_M$  dropped approximately 50% from 30°C to 40°C. This suggests that at higher temperatures there are higher chances of the complex enzyme-substrate to be formed. The parameter  $K_I$  increased with temperature and this behavior was also observed for the ratio

$K_I/K_M$ . These trends indicate a lower influence of the inhibition effects at higher temperatures (Chaplin & Bucke, 1990), as described in Figure 3.10.

**Table 5.1** Kinetic parameters estimated for purified free AAR at different temperatures (equation 3.36).

T [°C]	$V_{max}$ [ $\mu\text{mol min}^{-1}\text{mg-enzyme}^{-1}$ ]	$K_M$ [mM]	$K_I$ [mM]	$K_I/K_M$ [mM]
30	$22 \pm 4.3$	$42 \pm 15$	$238 \pm 101$	5.7
35	$24 \pm 2.0$	$31 \pm 5.0$	$496 \pm 129$	16
40	$30 \pm 2.1$	$20 \pm 3.3$	$794 \pm 234$	39

In the work reported by Würges and coworkers (Würges et al., 2009b), the kinetics parameter of the same racemase were estimated at a similar temperature range. The results showed a typical Michaelis-Menten kinetics and no effect of substrate inhibition was observed. Comparing the kinetic parameters found in the present work, the relation between  $K_M$  and temperature was reversed and the  $K_M$  values increased for higher temperatures. Despite the substrate inhibition, there was a substantial improvement in the specific activity of the AAR using the production and purification protocols proposed here. The values of  $V_{max}$  were 7 to 12-fold higher, and the values of  $K_M$  were 1.5 to 5.1-fold lower, depending on the temperature.

### 5.1.1 Influence of reaction parameters

Besides temperature, other reaction parameters can influence an enzyme-catalyzed reaction. The impact of enzyme dosage and of the initial enantiomeric excess are relevant for the coupling with preferential crystallization and their effect on the rate of racemization were investigated.

The influence of dosage on the activity was evaluated at  $D_C = 20, 100$  and  $400$  mg-enzyme/L. The progress of the concentration during the reactions at each respective dosage and showed in Figure 5.2. The dark and light colors denote the substrate and the product, respectively, and each symbol represents a different dosage. A direct relation between the amount of enzyme and the rate of reaction was observed. At the enzyme concentration, the system reached the racemic mixture after 15 min of reaction. By increasing the dosage 5 and 20-fold, the initial rate increased linearly in the same way. Although uncommon, some enzymes can observe a nonlinear effect between activity and dosage (Eisenthal & Danson, 2002). Hence, the influence of catalytic dosage on the AAR needed to be confirmed experimentally. This is an important finding since high amounts of enzyme are necessary for the process integration with preferential crystallization. Furthermore, catalyst dosage is a key parameter when

designing chiral resolutions. A dynamic kinetic resolution process for production of amino acids has been developed with the enzymatic tandem N-succinyl-amino acid racemase and L-N-carbamoylase (Soriano-Maldonado et al., 2015). Because racemization was the limiting step, catalyst dosage and immobilization loading were optimized to regulate the ratio between the enzymes and improve process performance. For a DKR enzyme coupling to be effective, racemization must be at least as fast as the enantioselective reaction (Faber, 2001).

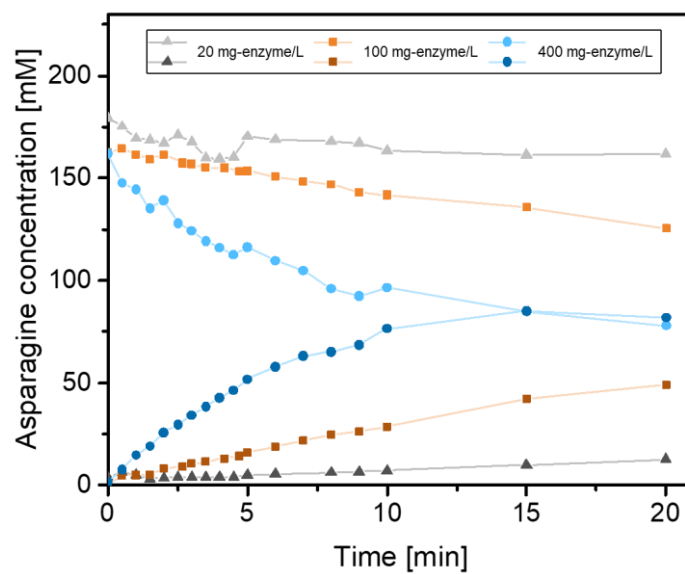


**Figure 5.2** Effect of AAR dosage on racemization. Concentration profiles of reactant (D-asparagine, being consumed) and product (L-asparagine, being produced) at dosages 20 (triangles), 100 (squares) and 400 (circles) mg-enzyme per liter of reaction. Symbols are experimental measurements. Lines are just guide to the eyes.

Another parameter relevant for the coupling with PC is the enantiomeric excess. The  $ee$  is expressed as a function of the concentrations of both enantiomers, as in equation 6.22. PC works as a resolution process by breaking the symmetry of the racemic concentration (see section 2.3). The enantiomeric excess generated in the liquid phase during PC is rather low, far away from the favorable reaction conditions of chiral purity. Therefore, the effect of  $ee$  on the reaction rate was investigated. The results are shown in Figure 5.3. For comparison, the values specific activity were calculated relative to the maximum at each temperature, that is, pure enantiomer. It is clear that the initial enantiomeric excess determines the driving force for the reaction and it has a strong impact on its velocity. The trends were similar for all temperatures tested. The operating window for the coupling with PC is located towards the lower left side of Figure 5.3. Hence, to effectively improve the chiral resolution, high catalyst dosage are necessary to compensate for the low driving forces for the reaction. Since enzyme production is expensive and time consuming, recyclability of the catalyst is crucial. Enzyme immobilization, discussed in the next section, brings the advantage of easy separation from

reaction media and re-use, in addition to the possibility of applying a high concentration of enzyme for the proposed application.

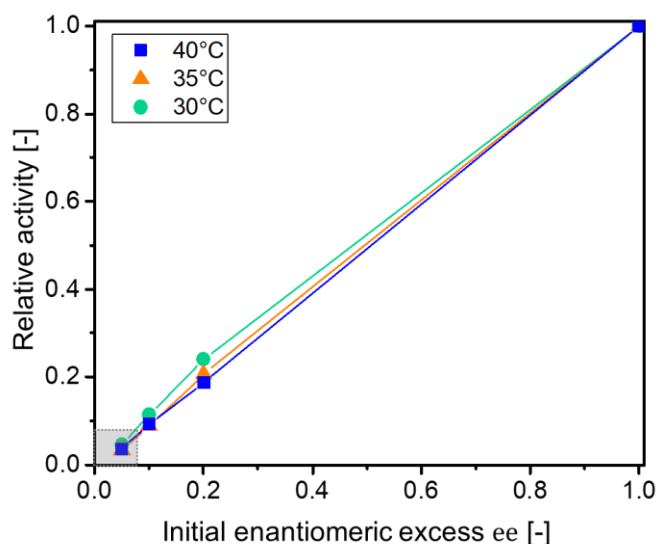


**Figure 5.3** Effect of initial enantiomeric excess in activity of free soluble AAR at different temperatures. Specific activity calculated relative to the maximum activity (pure enantiomer, at  $ee^0 = 1.0$ ) at each respective temperature. Symbols are experimental values, lines are guide to the eye. Gray area indicates the operating window for PC.

The formation of low enantiomeric excesses and consequently low driving force for racemization is a characteristic from preferential crystallization, but it is not necessary valid for all chiral separation processes. For instance, chromatographic resolution typically produces solutions highly enriched in the undesired enantiomer. Hence, lower dosages of catalyst are necessary for an effective process design. A membrane reactor with soluble free amino acid racemase has been employed in combination with SMB chromatography to resolve D/L-methionine (Fuereder et al., 2016). The authors reported the limiting coupling parameter was in fact the stability of the enzyme in organic solvents mixtures, essential mobile phase for the SBM process. Enzyme engineering has been reported to significantly improve solvent stability of the racemase (Femmer et al., 2020).

## 5.2 Immobilization of AAR

### 5.2.1 AAR immobilization from crude extract on affinity binding supports

Three types of affinity supports were tested. The surface of the beads are chelated with Fe(III). The presence of the chelating agent in those supports allows the target protein to be immobilized directly from the crude cell extract (CE) without prior purification. The carrier

differ in their surface properties: A has a hydrophilic surface, B has hydrophobic surface, and C has semi-hydrophobic surface.

Figure 5.4 depicts the results of immobilization on the affinity supports. The white bars show the specific activities found relative to the highest one, obtained for immobilization with carrier B. Immobilization on C resulted in the highest immobilization yield (equation 4.3), 19% of the total proteins incubated were bound to the support. Despite this result, the specific activity obtained with this support was 89% of that provided by carrier B. Qualitative SDS gel analysis of filtrate and wash from immobilization indicated that a higher amount of unspecific proteins from the crude cell extract were bound to carrier C. Hence, for the same immobilization conditions carrier B resulted in a better enrichment of the target protein. It is likely that the excess of bound proteins hindered the target racemase during reaction with immobilized enzyme on carrier C. Only 0.6% of total protein was immobilized on carrier A, which resulted in specific activity close to zero. This suggests that the high ionic strength of the immobilization buffer works in favor of protein adsorption on hydrophobic surfaces of carriers B and C.

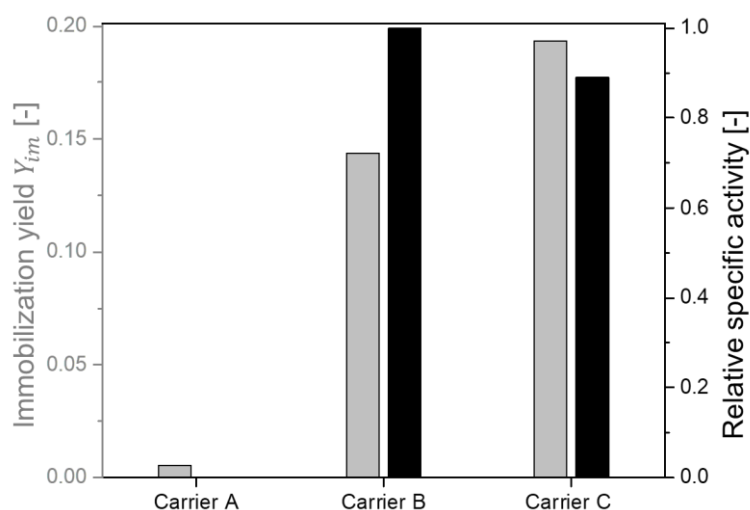


**Figure 5.4** Immobilization of AAR on affinity binding carriers. Grey bars: immobilization yield (equation 4.3); black bars: specific activity relative to the highest activity found (carrier B). Immobilization conditions: phosphate buffer pH 8.0 and incubation load 250 mg-protein/g-support.

Further immobilization conditions with varying pH and incubation load were investigated for carrier B. The results are presented in Figure 5.5. At pH 8.0 the immobilization yield was lower than at pH 7.4, but it resulted in higher specific activity, suggesting again a better enrichment of the target protein upon immobilization. This effect was observed in all immobilization results with carrier B: the highest specific activity was found for the lowest immobilization yield. The influence of incubation load was dependent on the pH. At pH 7.4,

the specific activity increased with the load, whereas the opposite effect was observed at pH 8.0. Improved results were obtained with pH 8.0 and incubation load of 250 mg-protein/g-support, with specific activity of 454 U/g-support. The low immobilization yield and high activity obtained at these conditions demonstrated a high selectivity of the binding provided by carrier B.

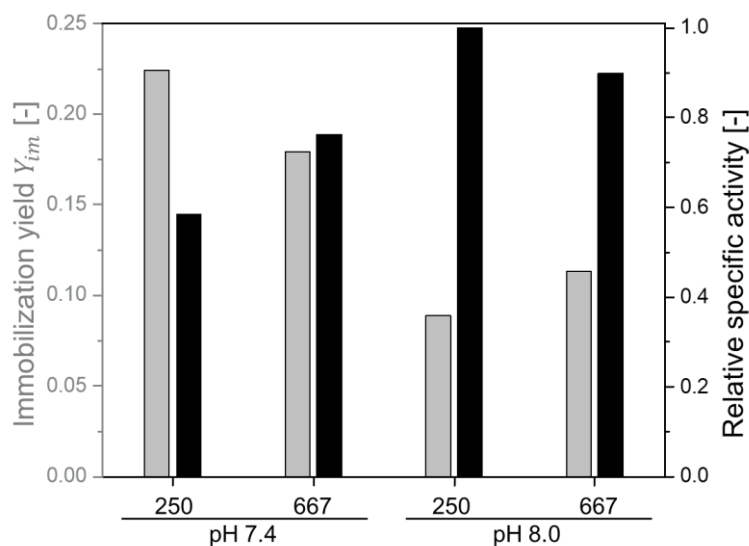


**Figure 5.5** Immobilization of AAR on carrier B under varying conditions of pH (7.4 and 8.0) and incubation load (250 and 667 mg-protein/g-support). Grey bars: immobilization yield (equation 4.3); black bars: specific activity relative to the highest one found (pH 8.0 and 250 mg-protein/g-support).

### 5.2.2 AAR immobilization from purified enzyme on covalent binding supports

Three covalent binding supports were tested for immobilization of the purified AAR: Eupergit CM, and Lifetech ECR 8204F and ECR 8309 (in particle size of grades F and M). The first two carriers are microporous, epoxy-activated acrylic supports. The immobilization reaction occurs via multipoint covalent binding between the epoxy groups on the acrylic polymer and functional groups of the protein. Lifetech ECR 8309 is an amino-activated support with ethylene spacer. This carrier must be pre-activated with glutaraldehyde before incubation with the protein. The immobilization process happens between the aldehyde and amino groups of the enzyme.

Eupergit CM was tested at incubation load of 27 and 37 mg-protein/g-support and the Purolite carriers were tested at incubation load of 25 and 35 mg-protein/g-support. The loading values were lower in comparison to the affinity binding carriers, because the immobilization was performed with purified enzyme instead of crude cell extract. The results are presented in Figure 5.6. All covalent-binding supports achieved immobilization yields higher than 97%. In

the above-mentioned load range, the carriers presented higher specific activity for the highest load. The best activity results were obtained with ECR 8309F. Then, the influence of the incubation load in this carrier was investigated for a broader range of 4.2 to 50 mg-protein/g-support (Figure 5.6). The immobilization yield with ECR 8309F was above 99% at all conditions tested. The highest specific activity was found with load of 35 mg-protein/g-support. Increasing the load to 50 mg-protein/g-support resulted in a lower reaction rate. The higher density of immobilized racemase likely caused steric hindrance of the enzyme. This effect can not only limit the accessibility to the active site of the enzyme, but also cause protein denaturation (Talbert & Goddard, 2012). The highest specific activity of 506 U/g-support was obtained for an incubation load of 35 mg-protein/g-support.

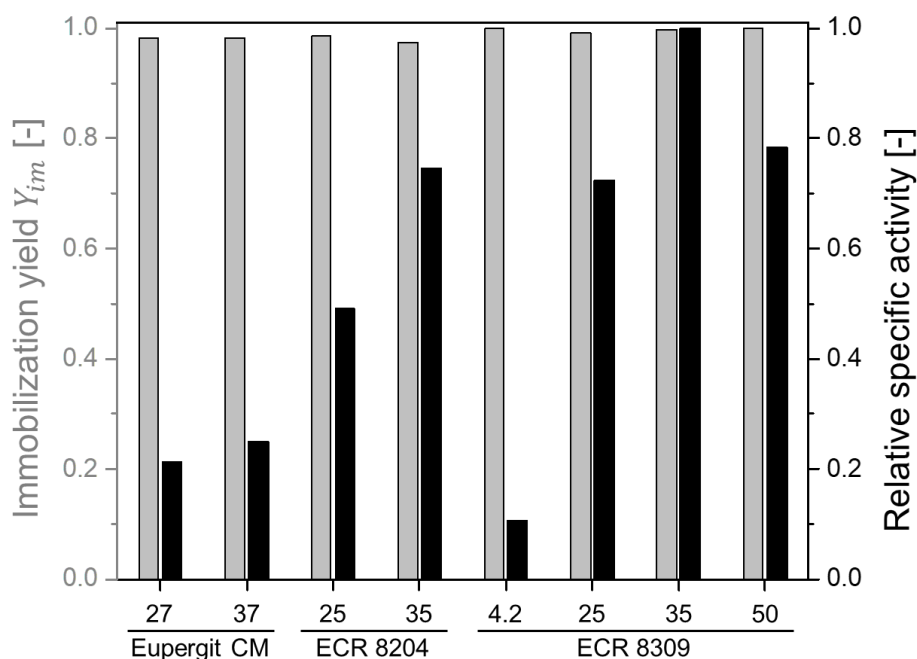


**Figure 5.6** Immobilization of purified AAR on covalent binding supports under varying incubation load conditions (4.2 to 50 mg-protein/g-support, indicated under the bars). Grey bars: immobilization yield (equation 4.3); black bars: specific activity relative to the highest one found (ECR 8309F with 35 mg-protein/g-support).

To evaluate the effect of particle size in the immobilization procedure, the carrier ECR 8309 with a higher range of particle size was tested (Figure 5.7, left). The immobilization was carried out at incubation load 4.2 mg-protein/g-support. The immobilization yield obtained was similar for both supports. The specific activity found with grade F was 22% higher than with grade M. This is a possible consequence of mass transfer limitations in the ECR 8309M or hindered accessibility to the enzyme active site. The influence of internal mass transfer is known to become more dominant with increasing particle size (Horn et al., 2008). However, further experiments would be needed to confirm this hypothesis.

Figure 5.7 (right side) shows the comparison of immobilization on ECR 8309F using the crude cell extract solution and purified AAR, both at incubation load 25 mg-protein/g-support. Prior to immobilization, the cell extract presented rather low specific activity, approximately 1.0 U/mg-protein. The activity improved after immobilization, but the immobilized purified enzyme was nevertheless 94% more active.

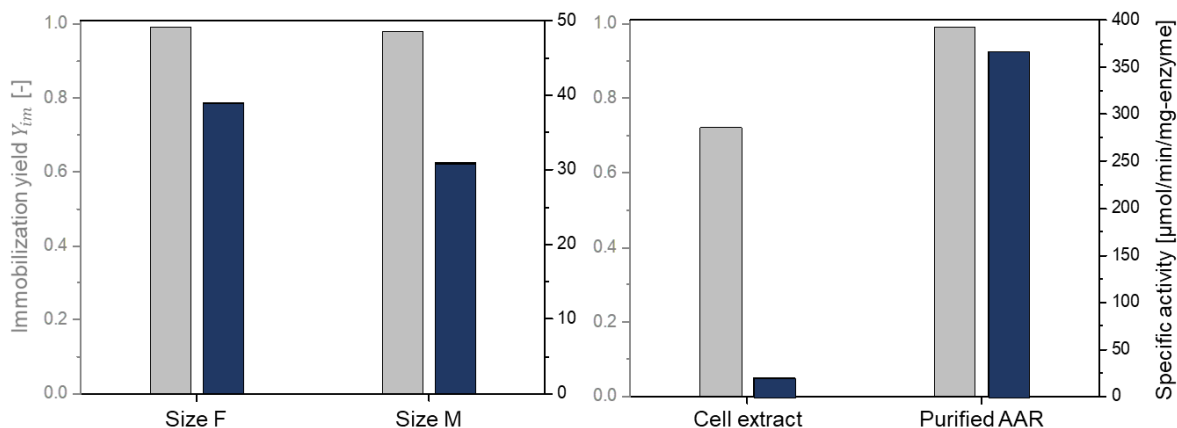


**Figure 5.7** Immobilization of AAR on ECR 8309 under varying conditions. Left: comparison carrier particle size (F: 150 – 300  $\mu\text{m}$ , M: 300 – 710  $\mu\text{m}$ ). Right: comparison of immobilized AAR solution. Grey axis and bars: immobilization yield (equation 4.3); blue axis and bars: specific activity.

### 5.3 Stability of immobilized AAR

Together with easy separation from reaction media, one of the main benefits of immobilizing enzymes is the possibility to recycle the biocatalyst. Hence the reusability of the two immobilized AAR preparations with the highest enzymatic activity was tested: affinity-binding carrier B and covalent-binding carrier ECR 8309F. After 30 minutes of reaction the final concentrations obtained at each cycle were measured and the conversions were calculated. A modified conversion expressed via changes in enantiomeric excess was calculated as:

$$X_{ee} = \frac{ee^0 - ee}{ee^0} = \frac{(c_2^0 - c_2) - (c_1^0 - c_1)}{c_2^0 - c_1^0} \quad (5.1)$$

where  $ee^0$  is the initial enantiomeric excess,  $c_i^0$  is the initial concentration of enantiomer  $i$  (1 = target enantiomer, 2 = counter enantiomer). The maximum value of conversion is 1.0, when the solution is racemic and the final enantiomeric excess is zero.

The results can be seen in Figure 5.8. In the case of ECR 8309F, high conversion was obtained for all cycles, with  $X_{ee}$  exceeding 0.987 every cycle. With carrier B, in the first use the conversion reached 0.868, and it dropped to 0.661 after the sixth cycle. The final enantiomeric excess was 13% and 34% after the first and last cycle, respectively. The difference in the stability upon reuse is probably due to the nature of the binding enzyme-support. The affinity carrier promotes complexation by metal-chelating binding between the chelate Fe(III) ions and the histidine chain of the AAR. This bond is weaker than covalent attachment to ECR surface, which may cause enzyme leaching and the drop in activity during subsequent cycles. Even though affinity carriers have been reported with a good recyclability under certain conditions, they are more likely to undergo loss in activity after reuse (Aßmann et al., 2017; Sheldon & Woodley, 2017; Thompson et al., 2019). In a comparative study between immobilization supports with affinity, adsorption and covalent attachment (Aßmann et al., 2017), the last bonding type was found to have better stability despite lower specific activity.

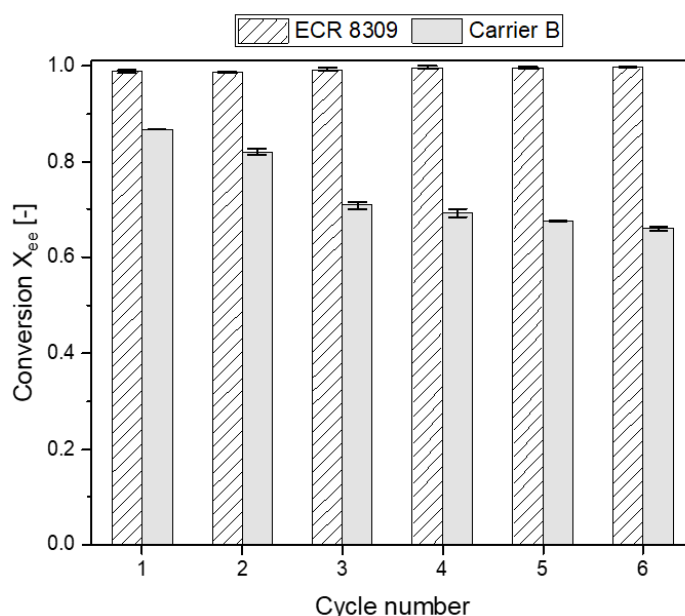


**Figure 5.8** Reusability test of AAR immobilized on ECR 8309F and carrier B. Final reaction conversion  $X_{ee}$  (equation 5.1) was calculated after each cycle. Reaction conditions:  $T = 30\text{ }^{\circ}\text{C}$ ,  $D_C = 40\text{ g-support/L}$ , 30 minutes reaction. All experiments were repeated three times. The error bars that cannot be seen are too short to appear.

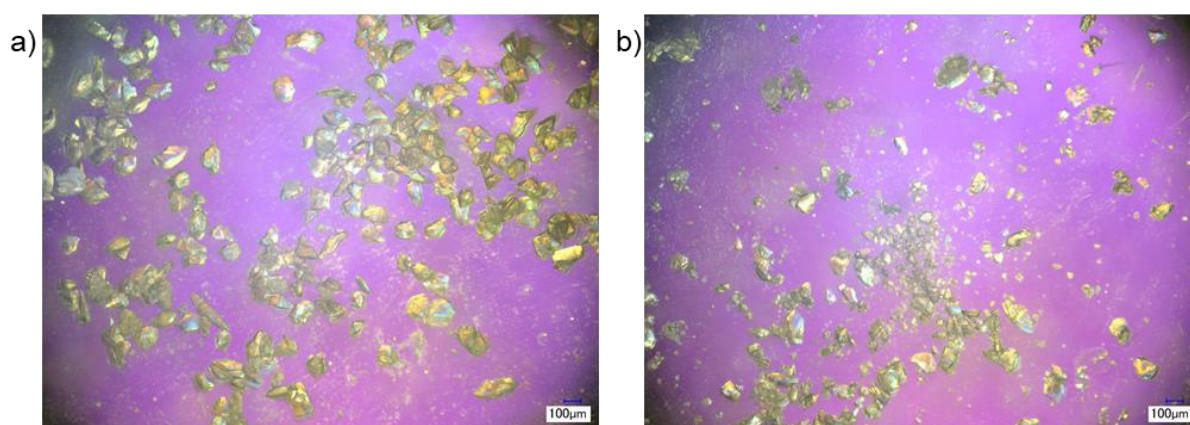
Table 5.2 shows a summary of the characteristics of AAR immobilization on ECR 8309F and carrier B. Each support demands a distinct immobilization procedure. Carrier B had the advantage of not requiring prior purification, which is a good economical advantage for the purification step being material and time consuming. The immobilization procedure required by the affinity carrier was also considerably shorter, and without the need of a pre-activation step.

**Table 5.2** Comparison of supports ECR 8309F and carrier B for AAR immobilization.

	<b>Lifetech ECR 8309F</b>	<b>Carrier B</b>
<b>AAR solution</b>	Purified AAR	Crude cell extract
<b>Conditions of Immobilization load</b>	35 mg-enzyme/g-support	250 mg-protein/g-support
<b>Incubation time</b>	18 h	45 min
<b>Resin activation</b>	Yes, 1.5 h	No
<b>Specific activity</b>	500 $\mu\text{mol}/\text{min}/\text{g}$ -support	450 $\mu\text{mol}/\text{min}/\text{g}$ -support
<b>Reusability test</b>	No loss in activity observed.	Loss in activity after 2 <sup>nd</sup> cycle. Conversion dropped 24% after 6 cycles.

Preliminary tests of enzymatic activity were performed with both carriers in a 50 ml stirred tank reactor with the immobilized enzyme in suspension, as the protocol described in section 4.9. No activity of carrier B could be detected in this setup. The beads were immediately crushed by the overhead stirrer. The particles we analyzed on the microscope before and after the reaction (Figure 5.9). The shear forces generated by the stirrer caused mechanical attrition, which leads to pulverization of the immobilized particles (Sheldon & Woodley, 2017). Besides affecting the activity, this contributes to difficult separation and reuse. The breakage of the beads was observed for ECR 8309F only after several hours of experiments. The enzymatic activity was not strongly affected, but the filtration time increased significantly. Polyacrylic supports such as ECR 8309F present better mechanic properties than porous glass (Garcia-Galan et al., 2011).

For AAR immobilization, ECR 8309F was therefore identified to be more stable for reuse in the conditions tested. As operational stability is of high importance for the intended integration with chiral resolution, the support ECR 8309F was chosen for further experiments.

**Figure 5.9** Light microscopy images of carrier B (a) before and (b) after reaction in a stirred tank reactor.

## 5.4 Kinetics of immobilized enzyme

The specific activity of the AAR on ECR 8309F (load 35 mg-protein/g-support) was investigated at a range of initial concentrations of pure D-asparagine. The reactions were performed in a batch reactor with the immobilized racemase in suspension. The estimated kinetic parameters of the reversible Michaelis-Menten equation are presented in Table 5.3. Figure 5.10 shows the experimental data and the respective model curve. For comparison, the kinetic results of the free enzyme at the same temperature are also depicted (same data presented in Figure 5.1). Unlike the results for free AAR, no effect of inhibition was detected in the kinetics of the immobilized racemase. The attenuation or overcoming of inhibition effects after immobilization has been previously reported (Mateo et al., 2007; Rodrigues et al., 2013). The mass transfer effects generated with the biocatalytic particles cause gradients in the substrate and product concentration, and they reduce from surface to particle core (Adamíková et al., 2019). This decrease could ease the effects of high concentrations in the reaction rates. Also, the kinetic constants  $V_{max}$  and  $K_M$  changed upon immobilization. This is caused by internal structural changes and restricted access of the reaction substrate to the enzyme's active site (Chaplin & Bucke, 1990). Because of the molecular diffusion effects in heterogeneous reaction, the parameters estimated experimentally might not represent the intrinsic values, but obtained from apparent reaction rates. The maximum velocity  $V_{max}$  of the immobilized AAR increased 26% relative to the value obtained with soluble enzyme (see Table 5.3). The value of  $K_M$  was almost 10 times higher than that of the free enzyme. This reflects a relatively lower affinity to the substrate.

**Table 5.3.** Comparison of kinetic parameters estimated for free and immobilized AAR. For the immobilized racemase, the parameter  $V_{max}$  in mg-enzyme was calculated from the respective immobilization load (35 mg/g-support).

AAR	T [°C]	$V_{max}$ [ $\mu\text{mol min}^{-1}$ mg-enzyme $^{-1}$ ]	$V_{max}$ [ $\mu\text{mol min}^{-1}$ g-support $^{-1}$ ]	$K_M$ [mM]	$K_I$ [mM]
Free	40	30 ± 2.1		20 ± 3.3	794 ± 234
Immobilized in ECR 8309F	40	37 ± 4.3	1309 ± 122	201 ± 36	-

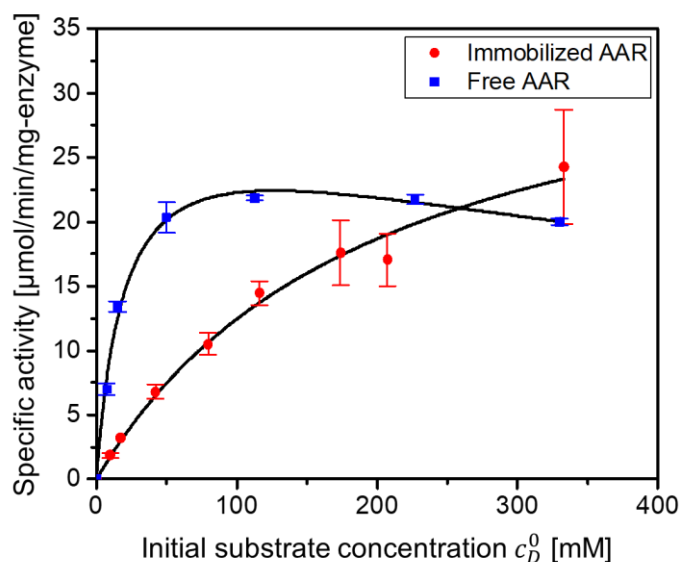


**Figure 5.10** Comparison of reaction kinetics of immobilized (red circles) and free (blue squares) racemase. Reaction temperature: 40 °C. Solid curves are the respective kinetic models (equations 3.35 and 3.36) with estimated parameters (Table 5.3). AAR immobilisate: ECR 8309F with load 35 mg-enzyme/g-carrier. ). All experiments were performed in duplicate.

As a consequence of the overcoming of inhibition effects, at high substrate concentrations the immobilized AAR presents a higher enzymatic activity compared to the free enzyme. For reactant concentrations above 257 mM (3.86 wt% of asparagine monohydrate), the rate of racemization achieved with immobilized AAR is more efficient than that with free enzyme.

## 5.5 Application in packed bed reactor

A column was packed with the immobilized AAR to investigate the efficiency of the packed bed reactor (PBR) for integration with PC. The packing conditions and column properties were described in Table 4.4 The mass balance equation of a PBR operating under steady state conditions was showed in Chapter 3, section 3.4.2. For the free enzyme, racemization reaction at 40 °C provided the highest activity. This condition was therefore set for the kinetics of enzyme immobilisate and the PBR experiments. It fits well, for instance, for the online coupling with PC performed at  $T_{cryst} = 30$  °C and  $T_{sat}$  between 30 and 40°C. The racemization reactor operating at temperature higher than the saturation helps to avoid the occurrence of nucleation outside the crystallizer. During the experiments of isothermal PC of asparagine monohydrate (see Figure 6.6), the maximum enantiomeric excess achieved was in the range from 4.6 to 5.2%. Hence, the racemase PBR was operated at feed concentrations with  $ee = 100\%$  and 4.5% (excess of D-Asn) under varying residence times (equation 3.43). The reaction conversions  $X_{ee}$  were calculated as described in equation 5.1. The maximum

equilibrium conversion is 1.0 independent on the initial enantiomeric excess. A conventional conversion expression in terms of substrate concentration can also be used, for instance  $X = \frac{c_2^0 - c_2}{c_2^0}$ . But in that case, the equilibrium value  $X^{eq}$  would vary relative to the initial enantiomeric excess. For example, for  $ee^0$  equal to 100% and 4.5%,  $X^{eq}$  would be 0.50 and 0.043, respectively.

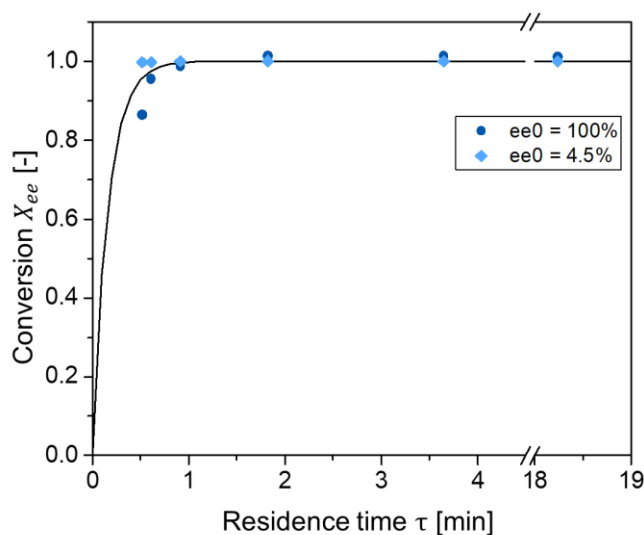


**Figure 5.11** Reaction conversion obtained with the racemase PBR operated at steady state conditions at feed solutions with  $ee^0 = 100\%$  (circles) and 4.5% (diamonds). Solid curve: PBR model equation with immobilized AAR kinetic data obtained in batch conditions.

The PBR results are shown in Figure 5.11 and reveal that reactions with  $ee^0$  of 4.5% achieved conversion values above 0.998 at the range residence time tested. For the enantiopure feed, the minimum conversion was 0.865 at the lowest residence time, that is 0.6 minute. After 1 minute, 0.990 conversion was achieved. For the reactions carried out at residence times longer than 2 minutes, the results showed negative values of final enantiomeric excess, from -0.4 to -1.5. This generated conversion values slightly above the unit. These results were associated with the sensitivity of the analytics towards very low enantiomeric excesses, for no racemization is known to progress beyond the racemic mixture.

The PBR operational stability was verified by repeating the first experiment ( $\tau = 0.6$  min and  $ee^0 = 100\%$ ) after two full days of use at 40°C and five days of storage at 4°C. The resulting conversion was 93% of the initial value, confirming the good biocatalytic stability observed in the reusability tests (Figure 5.8).

Figure 5.11 also shows the PBR simulation profile modeled with the kinetic parameters obtained in batch mode (Table 5.3). The theoretical results are in good agreement with the

experiments. Investigation of residence times below 0.6 minute, obtained with a flow rate of 3.5 ml/min, were not feasible because of back pressure limitations intrinsic to the system. A more detailed study of the conversion profile between  $\tau = 0.6$  and 1 minute was out of the scope of this thesis.

The results indicate that the application of the AAR packed bed reactor has the potential to improve PC. The high stability, easy reuse and rapid activity of the immobilized racemase are particularly attractive features for the complementary unit operation. The reactor is capable of achieving high conversions after only one minute residence time even at conditions of low enantiomeric excess. It can therefore potentially sustain the supersaturation levels of the target enantiomer during PC, delay or even avoid crystallization of the counter molecule, and, as a consequence, increase the overall process yield and productivity. In addition, the kinetic data found for the AAR in stirred tank experiments was successfully applied to simulate the fixed bed reactor. In the next chapter, the development of a shortcut model to describe preferential crystallization is presented. The kinetic model of the amino acid racemase is applied to the model to simulate the coupled units for the resolution of asparagine enantiomers. Hence, the investigation showed in the present chapter forms a valuable quantification basis for process design, which can be used to determine coupling parameters (e.g. enzyme dosage, reactor volume, flow rate of the recycling stream) and to estimate the performance of the coupling of preferential crystallization and enzymatic racemization.

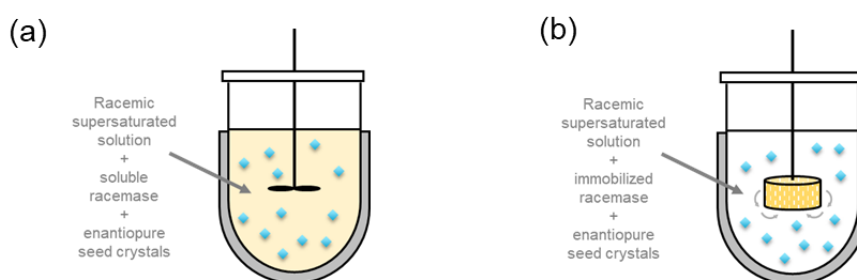
## 5.6 Outlook for the coupling of PC and racemization

Several setup configurations can be contemplated for the combination of preferential crystallization and racemization. The choice of the most appropriate scheme depends on process specifications, such as product purity, productivity and yield, and desired operating conditions, for instance, solvent, temperature range, etc. Figure 5.21 illustrates coupled preferential crystallization and enzymatic racemization in batch mode carried out in a single-unit process (panels a and b), in two-unit configuration with online integration (panels c and d) and stepwise coupling (panel e).

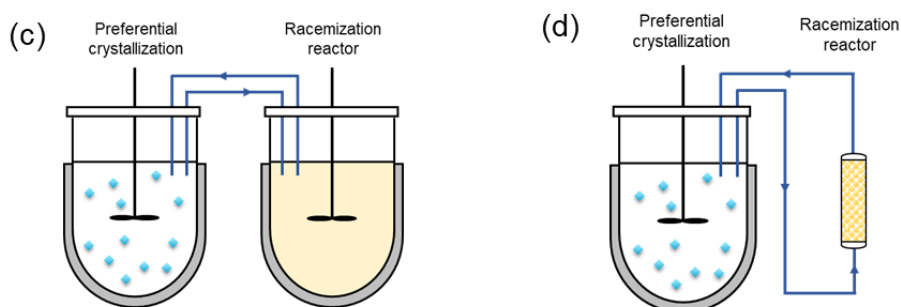
The simplest possible setup is the direct coupling in which both process are held simultaneously in a single unit (Figure 5.12 a and b). In contrast to a two-unit configuration, there is no delay between the PC and racemization units due to bypass flows. However, in a one-unit setup, both processes must be carried out at similar operating conditions of solvent, temperature and reactor volume. In addition, the possible effects of soluble enzyme or

immobilized particles on the nucleation and crystallization kinetics of the enantiomers must be acknowledge. Despite the increase in complexity, the use of two separate units provide more flexibility for process optimization. Similar operating conditions in terms of solvent are highly advantageous. The exchange in liquid phase allows better control of supersaturation and enantiomeric excess therefore offering more possibilities for process intensification, situation resembling application of PC in coupled crystallizers (Elsner et al., 2011). The optimization of reactor size, residence time and operating temperature is possible for each individual process. One of the strongest constraints is temperature of the enzymatic reactor. This unit (and also the bypass streams) must be operated at a higher temperature than the saturation of the solution ( $T_{sat}$ ) to avoid crystallization outside of the crystallizer. Appropriate filters are also necessary to keep the streams crystal-free and catalyst-free.

#### Direct coupling: single-unit configurations



#### Direct coupling: two-unit configurations



#### Indirect coupling: stepwise process

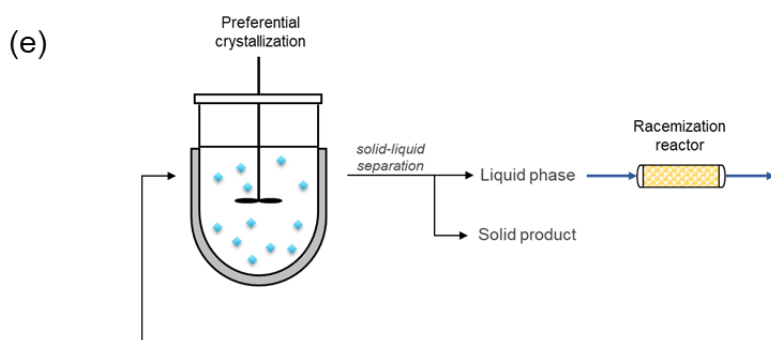


**Figure 5.12** Schematic configurations of the coupling of PC and enzymatic racemization in batch mode.

Another foreseen configuration is the step-wise or repetitive process (Figure 5.12 e), where racemization is executed after stopping PC and harvesting the solid product. This is an interesting configuration when the crystallization and racemization require incompatible conditions. The sequence can be repeated a certain number of times to maximize the recycle of the unwanted enantiomer. After each cycle, the final racemic solution is at a lower total concentration than the previous inlet feed. As a consequence, the saturation temperature is lower than in the previous cycle, resulting in reduced supersaturation levels and driving force for crystallization. The conditions of the following sequence can be adapted accordingly. One option is to add fresh feed solution to adjust concentration of the mother liquor. A second alternative is to keep the level of supersaturation constant by operating at a lower crystallization temperature. The main advantage of this configuration is the control of the minimum initial enantiomeric excess to operate the enzymatic reactor. As it became clear over the course of this work, the execution of preferential crystallization close to the racemic composition is a great limitation for the performance of the racemization reaction. The step-wise setup also provides the possibility to use different solvents or solvent composition, or to include other intermediate steps. The implementation of this configuration is likely more time and cost demanding. In addition, a compromise must be found between the increase in yield and possible drop in productivity generated by the increase in the number of cycles, i.e. longer process time.

It became evident during this study the advantages of using immobilized enzyme in opposition to soluble preparation. If to use free enzyme in the coupling with PC, an application with *in situ* racemization (Figure 5.12 a) or via online integration using for instance stirred tank (Figure 5.12 c) or membrane reactor (Bechtold et al., 2007; Fuereder et al., 2016) could be foreseen. Nevertheless, despite the possibility to use microfiltration for enzyme recovery, the separation from reaction media and reuse is largely facilitated upon immobilization. It is true that mass transfer effects could eventually restrict the application of the immobilisate, but particularly for the AAR the reaction rates were higher with immobilized preparation than the soluble enzyme at high substrate concentrations (see section 5.5). As demonstrated, the immobilized AAR can be successfully used in stirred tank reactor or in packed bed reactor. The PBR eliminates risks of grinding of immobilized biocatalyst, but it has intrinsic back pressure limitations. A third option is the application of a rotating bed reactor (RBR), which is an adaptation of the STR (Pithani et al., 2019). An schematic representation of such reactor is given in Figure 5.12 b. The immobilized enzyme is loaded in a compartmented rotating cell that acts as the stirrer and holds the catalyst in solution by filter walls. This setup would be particularly interesting for highly viscous solutions or immiscible liquids (Kara & Liese, 2019). In general,

the use of RBR could for instance facilitate screening of reaction and immobilization conditions for enzyme supports that are unstable under shear stress, caused by standard STR, or that are restricted by back pressure in packed columns.

Despite the driving force limitations, the coupling of PC and racemization can be in fact beneficial for enzymes that suffer from inhibition effects such as the free amino acid racemase (see Figure 5.1). The product concentration is depleted due to crystallization of the target enantiomer. This may result in an apparent shift in the reaction equilibrium, reducing the impact of inhibition effects. Crystallization is applied biocatalytic process as a tool for process intensification in a process integration known as *in situ* product crystallization (ISPC) (Hülsewede et al., 2019). This coupling also allows reducing concentration of intermediates and simplify downstream processing.

The main application of the coupling of PC with racemization discussed in this work is the resolution of racemic mixtures. The L-asparagine was used as the target molecule to be crystallized, with D-asparagine being the reactant of the enzymatic reactions. Nevertheless, the process can as well be applied on the production of pure D-amino acids, which are often significantly more expensive than its chiral pair. In fact, if the L-amino acid is available via chiral synthesis, the coupling concept can be used for the production of valuable D-enantiomers starting from pure L, as showed in Figure 5.13. One of the main adaptations is that the feed must undergo racemization before the seeding of the crystallization unit.

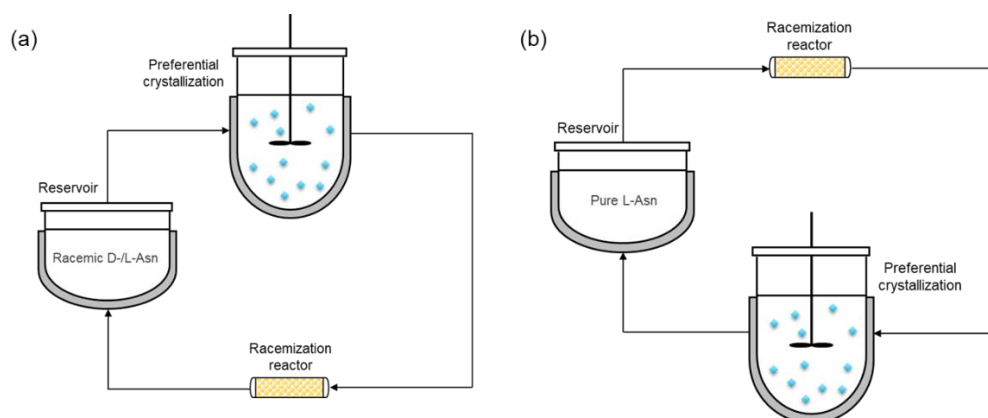


**Figure 5.13** Application of the coupling of preferential crystallization and racemization on the production of pure D-enantiomers starting from (a) racemic mixture and (b) the available L-enantiomer.

Other chiral resolution processes can benefit from the biocatalyst developed in this work. A performance comparison between two different process combinations, that is racemization integrated with PC and with chromatography, was established using the immobilized AAR as

the coupling system for the crystallization process (Harriehausen, 2017). The potential of the AAR packed bed reactor to improve chromatographic resolution of several amino acids has also been investigated (Bollmann, 2020; Harriehausen et al., 2021).

Furthermore, the high stability, high activity and easy separation from media of the immobilized AAR make it an attractive tool for deracemization techniques. The AAR immobilisate has been successfully implemented in *temperature cycling induced deracemization* (TCID) of asparagine enantiomers. Similarly to PC, TCID is a technique for direct resolution of racemates of conglomerate-forming systems (Suwannasang et al., 2013; Viedma & Cintas, 2011). The solid phase deracemization occurs in a racemic liquid phase and it is entrained by temperature fluctuations in the presence of a racemizing agent (see Figure 2.6 c). The study reported by (Intaraboonrod et al., 2020) demonstrated for the first time the application of a racemase in TCID of amino acids. The process was investigated at 10 mL scale with *in situ* immobilized AAR in cycles varying between 30 and 35 °C over a range of enzyme dosage. Compared to chemo-catalysis, the AAR enzymatic reaction allowed the use of lower temperatures, reducing the risk of decomposition of the chiral molecules. The immobilized amino acid racemase promoted efficient deracemization even at low dosage of 5 mg-support/mL and could be easily separated from reaction media. The deracemization process reported was not yet fully optimized, but the results showed the potential of the biocatalyst developed in this work and its capability to be a viable choice for further applications.

The study reported in the present chapter form a valuable resource for future design of process strategies, configurations and performance. The application of immobilized enzymes have a so far underexplored potential to improve performance of preferential crystallization and other techniques in the production of optically pure enantiomers. A limitation regarding the application of the coupling is clearly the existence of a racemase that can convert the desired chiral pair, and the laborious development of a biocatalyst unit. Therefore, intensive research is needed in efficient assessment of improved racemases and in enzyme engineering. Another interesting subject for future studies is an economical analysis for comparison between competing processes. The application of a bioreactor can potentially increase production costs, which could be compensated by the added value achieved by the racemization step. Fine chemicals and pharmaceuticals often carry higher costs due to smaller markets and higher process complexity (Tufvesson et al., 2011). The coupling with immobilized enzymatic racemization has the potential to not only increase yield and productivity, but also improve the process robustness.

## 6 Development and Application of a Shortcut Model for Preferential Crystallization

The work described in this chapter was developed in collaboration with the fellow doctoral researcher Shashank Bhandari at the Max Planck Institute in Magdeburg. The mathematical framework, implementation strategy and experimental assessment were published in *Crystal Growth and Design* (2019, 19(9), 5189–5203) under the title “*Shortcut model for describing isothermal batch preferential crystallization of conglomerates and estimating the productivity*” (Carneiro et al., 2019). A manuscript describing the extension of the model to predict coupled preferential crystallization and enzymatic racemization is currently in preparation (Bhandari et al., n.d.).

Obtaining a comprehensive description of preferential crystallization using population balance equations (PBEs) is effective (Elsner et al., 2005; Ramkrishna & Singh, 2014), however it tends to be a rather complex task. As described in Chapter 2, PBEs require the parametrization of kinetic semi-empiric models for crystal growth, primary and secondary nucleation and the application of reduction techniques such as the method of moments to solve the density functions. Thus, PBEs often require expensive and time-consuming experimental and computational demands. Several studies have been dedicated to simplify the quantification of growth and nucleation kinetics (Besenhard et al., 2015; Nagy et al., 2013; Temmel et al., 2016). Nevertheless, the full prediction of crystal size distribution might not be necessary for all process evaluations. There is a lack of simplified approaches for a quick overview during initial process design. This fact motivated the development of a reduced model to describe PC requiring less coding, simulation, and experimental time. In the present chapter, a shortcut model to evaluate the performance of preferential crystallization is introduced. The model requires a minimum number of three PC experiments and allows gaining important information about the outcome of the process.

In the following, first the assumptions required to derive the method are presented. Next, the model equations are described, illustrated and strategy to apply the model is proposed. An experimental validation using asparagine monohydrate as model compound is presented. Finally, the model is extended to predict performance of the coupling with racemization. Simulation results of productivity and yield using reaction kinetics of the amino acid racemase are discussed.

## 6.1 Model assumptions

The shortcut model (SCM) was developed for the simulation of batch isothermal preferential crystallization of conglomerate-forming systems. The main approach adopted was the simulation of PC focusing on the general performance rather than on detailed crystal size distribution or particle properties. The access to key performance indicators (KPIs) such as productivity, purity, and yield allow a general analysis of the process and its comparison with competing methods. The assumptions underlying the mathematical model are the following:

- All crystals of one enantiomer are spheres of identical increasing size.
- Very small particles of the counter enantiomer below a contamination threshold are assumed to be initially present, along with seeds of the preferred enantiomer.
- A stop time for the process ( $t_{stop}$ ) is introduced to activate growth of the particles of the counter enantiomer. This is the start of solid phase contamination.
- The total number of crystals in the beginning of the process is equal to the number of crystals at the end of the process.
- Simple power rate laws are used to describe the mass exchange between the phases.
- Driving forces respect metastable solubility limits in the three-phase region of the ternary phase diagram.
- No aggregation and breakage take place.
- There is no epitaxy between the crystals of the opposite enantiomer.

To achieve the desired simplification and to still be able to capture essential process characteristics, the shortcut model exploits the principal of *total mass transfer* between phases. The increase in the mass of solid phase generated by crystallization results in the decrease in solute mass in the liquid phase. For both target and counter enantiomers, the mass depletion in the continuous phase is assumed to be caused by crystal growth only. This overall growth kinetics is a well known assumption from the diffusion-reaction theories (Nernst, 1904; Noyes & Whitney, 1897) (see Chapter 2). In the SCM, no distinction was made between the steps of transport to the crystal surface and surface integration. This last step is assumed to be the limiting one. Therefore, crystal growth is strongly dependent on supersaturation, which is reflected in simplified model equations. Nucleation and growth rates are lumped and jointly cause liquid phase mass depletion and solid phase mass build up.

Figure 6.1 (a) shows a schematic description of the shortcut model and its assumptions. The system depicted is composed of three entities in the liquid phase, that is, the two

enantiomers and a solvent, and two entities in the solid phase, which are the crystals of each enantiomer. Isothermal PC takes place at the crystallization temperature  $T_{cryst}$  with initial supersaturation  $S^0$ . The crystal population of both target and counter compounds are monodispersed spheres. This is clearly a strong assumption, especially for the substances crystallizing in particular shapes, such as needles. The counter enantiomer is considered to be present since the beginning of the process (orange particles in Figure 6.1), but it stays inactive until the stop time is reached. Only the target enantiomer grows, which results in a depletion in supersaturation of that enantiomer. After the  $t_{stop}$ , the particles of the counter enantiomer become active and start growing. This accounts for the arising of primary nucleation, which compromises purity of the solid product.

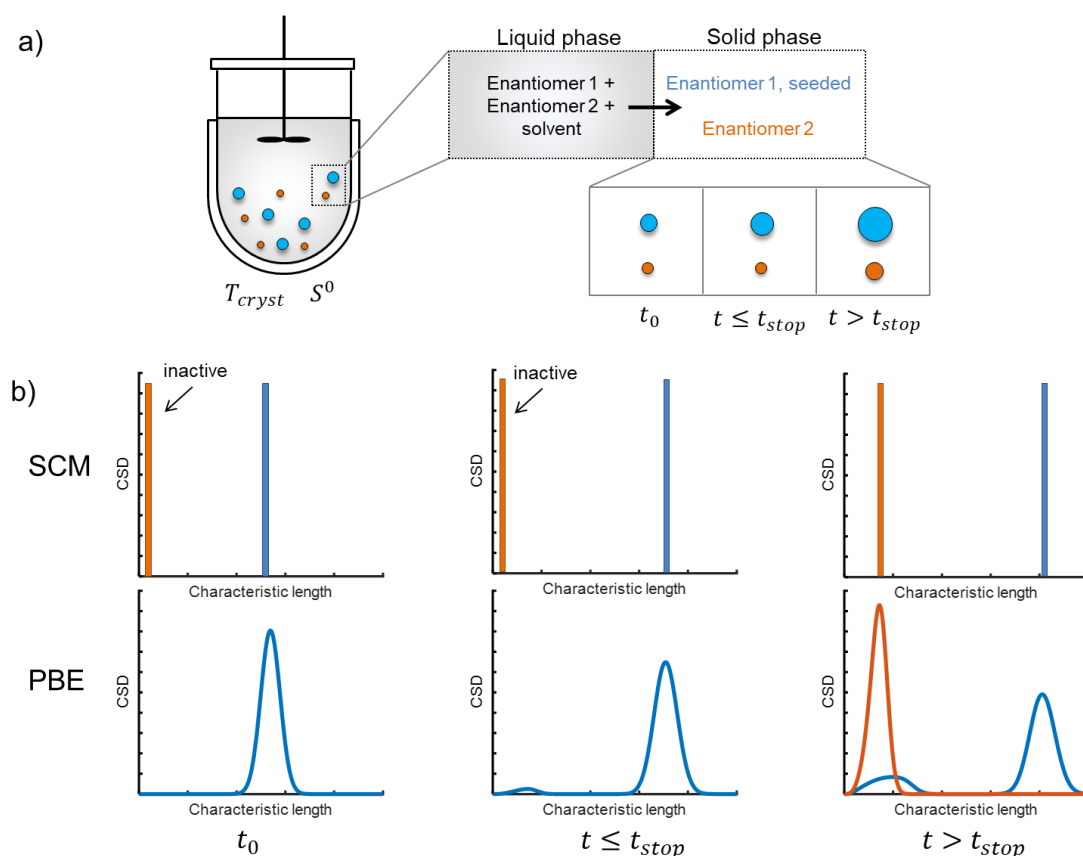


**Figure 6.1** Illustration of assumptions of the shortcut model (SCM) to describe batch isothermal preferential crystallization: (a) schematic description of the SCM, (b) comparison between crystal size distributions in PC described with the SCM and with population balance equations (PBE).

Figure 6.1 (panel b) shows a comparison between the particulate population in the SCM and a distribution described by population balance equations (PBE). In the SCM, all crystal distributions are monodispersed, whereas in PBE the seed population of the target enantiomer is normally distributed (at initial time  $t_0$ ). Secondary nucleation of enantiomer 1 may occur,

resulting in the appearance of a small size particles. The crystals of the counter enantiomer originate from primary nucleation.

## 6.2 Formulation of mass balances and initial conditions

The above-mentioned assumptions comprise the basis for the formulation of the shortcut model. The system studied is composed of preferred and counter enantiomers and a solvent, indicated with index 1, 2 and 3 respectively. For each enantiomer  $i$ , an overall effective mass transfer rate  $\overline{GB}_i^{eff}$  is expressed to quantify the accumulation of mass in the solid phase  $m_{S_i}$  due to growth and nucleation:

$$\frac{dm_{S_i}}{dt} = \overline{GB}_i^{eff} \quad i = 1, 2 \quad (6.1)$$

From the total mass balance, the depletion of mass in the liquid phase  $m_i$  is generated solely by the transfer of material to the solid phase. Therefore:

$$\frac{dm_i}{dt} = -\overline{GB}_i^{eff} \quad i = 1, 2 \quad (6.2)$$

The overall effective mass transfer rate was defined as a combination of three main effects: a rate of crystallization, an expression to characterize the increase in size of crystals, and a term representing the driving forces:

$$\overline{GB}_i^{eff} = k^{eff} 4\pi N_i R_i^2 (S_i - 1)^{n^{eff}} \quad i = 1, 2 \quad (6.3)$$

The right-hand side of equation 6.3 contains, at first, the effective mass transfer or effective crystallization rate constant  $k^{eff}$ . It lumps all crystallization mechanisms and must be determined experimentally. Subsequently, the equation is composed of the total surface area of all crystals ( $4\pi N_i R_i^2$ ), where  $N_i$  and  $R_i$  are the total number of particles and the radius, respectively. At last, there is the supersaturation term with exponent  $n^{eff}$  to account for non-linear dependence of growth on the driving force. The supersaturation is defined as a ratio of mass fractions (equation 2.1).

Assuming the density of the solid phase  $\rho_S$  to be constant, the changes in solid mass over time can be written as a function of the solid volume  $V_{S_i}$ :

$$\frac{dm_{S_i}}{dt} = \rho_S \frac{dV_{S_i}}{dt} \quad i = 1, 2 \quad (6.4)$$

If the  $N_i$  particles of enantiomer  $i$  are perfect spheres of uniform size, the total volume of solid phase is:

$$V_{S_i} = \frac{4}{3} \pi R_i^3 N_i \quad i = 1, 2 \quad (6.5)$$

and, hence, the rate of change in solid mass becomes:

$$\frac{dm_{S_i}}{dt} = \rho_S \frac{d\left(\frac{4}{3} \pi R_i^3 N_i\right)}{dt} = \rho_S 4\pi R_i^2 N_i \frac{dR_i}{dt} \quad i = 1, 2 \quad (6.6)$$

Therefore, the mass balance of the solid phase described by equations 6.1 and 6.3 can be rearranged in terms of the radius:

$$\frac{dR_i}{dt} = \frac{k^{eff}}{\rho_S} (S_i - 1)^{n^{eff}} \quad i = 1, 2 \quad (6.7)$$

The combination of equations 6.2, 6.3 and 6.7 builds the system of ordinary differential equations (ODEs) that compose the shortcut model. For the target enantiomer, the following equations hold:

$$\frac{dm_1}{dt} = -k^{eff} 4\pi N_1 R_1^2 (S_1 - 1)^{n^{eff}} \quad (6.8)$$

$$\frac{dR_1}{dt} = \frac{k^{eff}}{\rho_S} (S_1 - 1)^{n^{eff}} \quad (6.9)$$

The SCM proposed in this work pursues the description of processes with strict product purity specifications of 100% of target compound. To avoid contamination of the solid product, PC should be stopped before the crystallization of the antipode. Nevertheless, the representation of the counter enantiomer is helpful to illustrate how the process trends continue. In similarity to the equations for target molecule and assuming the parameters  $k^{eff}$  and  $n^{eff}$  are equal for both enantiomers, the balances in liquid and solid phase of unwanted compound can be written as:

$$\frac{dm_2}{dt} = -F_2 k^{eff} 4\pi N_2 R_2^2 (S_2 - 1)^{n^{eff}} \quad (6.10)$$

$$\frac{dR_2}{dt} = F_2 \frac{k^{eff}}{\rho_S} (S_2 - 1)^{n^{eff}} \quad (6.11)$$

$$F_2 = \begin{cases} 0, & t < t_{stop} \\ 1, & t \geq t_{stop} \end{cases} \quad (6.12)$$

The term  $F_2$  is the contamination factor. It introduces the stop time  $t_{stop}$  to the model, which activates the growth of the existing “nuclei” of the counter enantiomer.  $F_2$  is the “switch” parameter for equations 6.10 and 6.11, adding two extra ODEs to the system of equations of the SCM.

In case the studied conglomerate forms a hydrate or a solvate in the solid phase, the mass balance for the solvent (index 3) must be introduced:

$$\frac{dm_3}{dt} = - \left( \frac{dm_1}{dt} + \frac{dm_2}{dt} \right) \left( \frac{M_S}{M_i} - 1 \right) \quad (6.13)$$

$$\frac{dm_3}{dt} = - \left( k^{eff} 4\pi N_1 R_1^2 (S_1 - 1)^{n^{eff}} + F_2 k^{eff} 4\pi N_2 R_2^2 (S_2 - 1)^{n^{eff}} \right) \left( \frac{M_S}{M_i} - 1 \right) \quad (6.14)$$

The equations describe the depletion in solvent concentration due to the crystallization of both enantiomers. The general mass balance equation for the solvent (equation 6.13) is similar to the solvent mass balance written for the PBE (equation 2.20). Equation 6.14 is specific to the SCM. The right-hand side term is dependent on the ratio between the molar mass of the solid phase  $M_S$  and that of the single enantiomer  $M_i$  (nonsolvate). The relation between these two molar masses relies on the stoichiometric number of molecules of solvent that are incorporated in the crystal lattice.

In order to solve the ODE system formed by equations 6.8 to 6.11 and 6.14, initial conditions for all components (1 = target enantiomer, 2 = counter enantiomer and 3 = solvent) in the two phases are needed.

$$m_1(t = 0) = m_1^0, \quad m_2(t = 0) = m_2^0, \quad m_3(t = 0) = m_3^0 \quad (6.15)$$

The initial conditions of the liquid phase  $m_i^0$  are defined by the solid-liquid equilibria of the initial solution at the saturation concentration. In the solid phase, all particles of one

enantiomer are assumed to be spheres of identical size. The initial radius of crystals of the target enantiomer is:

$$R_1(t = 0) = R_1^0 \quad (6.16)$$

The value of  $R_1^0$  can be calculated from the mean value of the seed particle size distribution determined experimentally. The same is true to the initial mass of the solid phase, which is the seed mass  $m_{seeds}$  used during experiments:

$$m_{S_1}(t = 0) = m_{S_1}^0 = m_{seeds} \quad (6.17)$$

The total number of particles is calculated from the mass of seeds divided by the mass of one spherical particle:

$$N_1(t = 0) = N_1^0 = \frac{m_{seeds}}{\rho_S \frac{4}{3} \pi (R_1^0)^3} \quad (6.18)$$

It is assumed in the SCM that the number of particles of one enantiomer stays constant throughout the process, therefore:

$$N_1(t) = N_1^0 \quad (6.19)$$

The solid phase of the counter enantiomer is virtually present in the system from the start of the process. Therefore, further assumptions should be made to implement the initial conditions of this component. However, these assumptions do not affect the SCM predictions since they are only introduced after the process reaches the stop time. The total number of particles  $N_2$  was set as a constant equal to the total number of particles of the target molecule:

$$N_2(t) = N_1^0 \quad (6.20)$$

The initial radius  $R_2^0$  must be a very small quantity. A value in the range of nanometers was chosen, which is approximately in the size range of covalent bonds, and it is therefore below the unit cell dimension (Boyle, 2005).

### 6.3 Calculation of driving forces

The dynamic behavior of supersaturation is a key issue when quantifying PC. As the process evolves, the changes in supersaturation drive the depletion in concentration in the liquid

phase. In the SCM the saturation mass fractions  $w_{sat,i}$ , which are necessary to calculate supersaturation  $S_i$ , were determined using the ternary phase diagram. This method was explained in detail in Chapter 2. To facilitate the calculations, the concentration values are converted to the XY-orthogonal plane (Cartesian coordinates). The equations to transform between the two coordinate systems are presented in section 2.3 (equations 2.7 to 2.10) and demonstrated in Appendix A.1. In the TPD, the enantiomers might be represented at the triangle vertex or placed along the triangle sides, in case there is formation of a hydrate or a solvate.

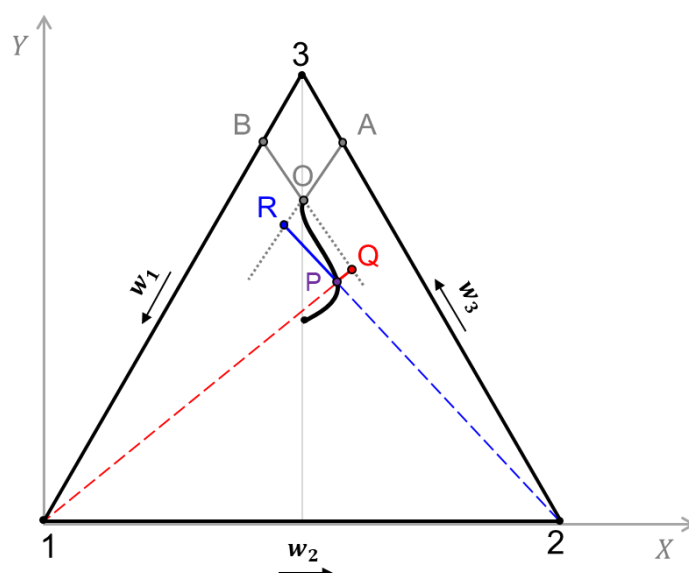


**Figure 6.2** Calculations of saturation mass fractions in the TPD applied in the SCM. The point P represents a “current state” condition, the points Q and R are the correspondent saturation mass fractions of enantiomers 1 and 2, respectively. Component 3 is the solvent. Dotted gray lines are the extension of the solubility isotherms AO and BO.

The steps to implement the driving force calculations are described in the following and illustrated in Figure 6.2:

- 1) Calculate of the current state concentrations  $w_1(t)$ ,  $w_2(t)$  and  $w_3(t)$ .
- 2) Convert mass fractions  $w_i$  to Cartesian coordinates  $[X_P(t), Y_P(t)]$  (equations 2.7 and 2.8).
- 3) Calculate the characteristics (that is, slope and intercept) of the lines 1-P and 2-P connecting pure enantiomers 1 and 2 and the current state point P  $[X_P(t), Y_P(t)]$ .
- 4) Calculate the intersection point Q between the line 1-P and the extension of the solubility curve AO (point Q  $[X_Q, Y_Q]$ ).
- 5) Calculate the intersection point R between the line 2-P and the extension of the solubility curve BO (point R  $[X_R, Y_R]$ ).

- 6) Convert Cartesian coordinates at points Q and R to mass fractions  $w_{sat,1}(t)$  and  $w_{sat,2}(t)$ , respectively (equations 2.9 and 2.10).
- 7) Calculate supersaturations  $S_1(w_{sat,1})$  and  $S_2(w_{sat,2})$ .

In order to perform any mathematical modeling, prior information on the solid-liquid equilibria at the potential operating saturation and crystallization temperatures and on the metastable zone width are required. The solubility equation at the crystallization temperature (curves AO and BO in Figure 6.2) must be converted to Cartesian coordinates to execute steps 4 and 5 listed above. Solubility isotherms can be determined by calculations, when thermodynamic data is available, or by experimental measurements. The last option is usually the most common and reliable (Mullin, 2001).

## 6.4 Experimental assessment of the SCM

Experimental data is required in order to estimate the model parameters and to evaluate the process performance. The observation of several process variables, for instance, solution density, concentration and particle size distribution, is unquestionably useful. However, one of the primary concerns during the development of the shortcut model was its simply design and analytics, that including the acquisition of experimental data. The dynamic behavior of PC was monitored by online measurement of the optical rotation angle in the liquid phase, which was captured by a polarimeter. In this analysis the solution passes through a sample cell, which measures the angle of rotation of the polarized light deviated by the chiral solution. More details of the experimental setup are given in Chapter 4.

The use of a polarimeter can be easily implemented in the SCM. Prior to PC experiments, the equipment must be calibrated with the relation:

$$\alpha = \frac{w_2 - w_1}{k_{pol}} \quad (6.21)$$

The quantity  $\alpha$  is the optical rotation angle and  $k_{pol}$  is the parameter to be determined upon calibration. This last parameter is constant for a fixed temperature, length of measurement cell and wavelength of the polarized light. The polarimetric signal is proportional to the exceeding concentration of one of the enantiomers in a mixture, which quantified by the *enantiomeric excess ee*. This quantity defined as a function of mass fractions is given by:

$$ee = \frac{|w_2 - w_1|}{w_2 + w_1} \quad (6.22)$$

For a racemic mixture,  $w_2 = w_1$  and the enantiomeric excess is zero. The maximum value of  $ee$  is the unit (or 100%), when the solution consists of a pure enantiomer. Combining equations 6.21 and 6.22, the polarimetric signal is formulated as a function of the enantiomeric excess of the liquid phase  $ee_L$ :

$$\alpha = ee_L \frac{(w_2 - w_1)}{k_{pol}} \quad (6.23)$$

The calibration parameter  $k_{pol}$  can be applied in the model to simulate the temporal profiles of optical rotation. These profiles can be compared to the experiments in order to evaluate the model parameters.

## 6.5 Performance criteria for process evaluation

Productivity is the main key performance indicator used in the SCM to evaluate isothermal batch PC. This parameter presents valuable information about the process performance. It can be used as a tool for designing the process and comparing PC with other process alternatives. The productivity was defined as:

$$Pr = \frac{m_{S_1}(t_{stop}) - m_{seeds}}{(t_{stop} + t_{dead}) V_L} \quad (6.24)$$

The expression represents the mass of solid product obtained per batch time per unit volume. The dead time  $t_{dead}$  is the additional time necessary for preparation and cleaning of the equipment and it was assumed in this work to equal to 1.0 hour.  $V_L$  is the total liquid phase volume. The productivity is formulated in the SCM with the solid mass of the target enantiomer only. Since the process is evaluated until the stop time, it is assumed that no contamination is present and the product is enantiopure.

Another important performance criteria to evaluate preferential crystallization is the process yield, which can be calculated as follows:

$$Y = \frac{m_{S_1}(t_{stop}) - m_{seeds}}{m_{Smax}} * 100\% \quad (6.25)$$

$$m_{S_{max}} = \left( w_{rac}(T_{sat}) - w_{rac}(T_{cryst}) \right) m_{tot}^0 \quad (6.26)$$

The yield  $Y$  was defined as the mass of product crystallized (final mass of solid target enantiomer  $m_{S_1}$  deducting the mass of seeds  $m_{seeds}$ ) relative to  $m_{S_{max}}$ , which is the maximum solid product that can theoretically crystallize at the desired temperature range. This quantity is calculated by the difference in racemic mixture in thermodynamic equilibrium at the saturation and crystallization temperatures (equation 6.26).

Purity requirements are also an important design parameter. This quantity can be calculated according to the expression:

$$Pu = \frac{m_{S_1}(t_{stop})}{m_{S_1}(t_{stop}) + m_{S_2}(t_{stop})} * 100\% \quad (6.27)$$

The product purity was defined as the mass of solid target enantiomer over the total solid product in a batch time. In the simulations using the shortcut model simulations the batch time  $t_{stop}$  was set in order to secure strict purity specifications of  $Pu = 100\%$ .

## 6.6 Illustration of the potential of the SCM

The solution to the set of ODEs of the shortcut model (equations 6.8 to 6.11 and 6.14) generate temporal progress of masses in the liquid phase and of particle radii in solid phase. This data can be subsequently used to calculate, for instance, solute concentration in the liquid phase and total mass in the solid phase. Figure 6.3 depicts illustrative results of the shortcut model. Panel (a) shows the concentration profiles in the liquid phase. As it is intrinsic to preferential crystallization, the mass fraction of the target enantiomer depletes since the beginning of the process due to the presence of the seeds. At first there is no crystallization of the counter enantiomer. The concentration of this compound increases slightly, due to decrease in the total mass of the liquid phase caused by crystallization of the target molecule. When the stop time is reached, the inactive “nuclei” are activated and the material transfer of counter enantiomer to the solid phase starts. When the system reaches equilibrium, the profiles of both enantiomers achieve a plateau.

Panel (b) depicts the progress curves regarding the solid phase. The initial solid mass of the target compound is given by the seeds. For the counter enantiomer, the initial mass is close to zero, as a result of the small radius of the inactive “nuclei”. They start growing only beyond

the stop time. At equilibrium, the different in height between the two plateaus is equal to the mass of seeds.

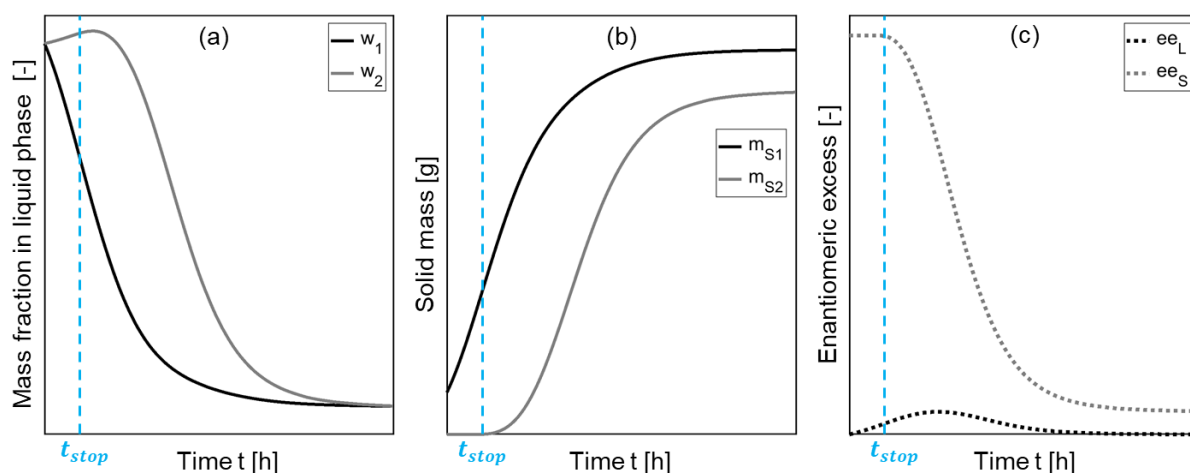


**Figure 6.3** Illustrative simulation of preferential crystallization using the shortcut model. Progress of (a) liquid phase mass fractions of enantiomers 1 and 2, (b) solid mass of each enantiomer and (c) enantiomeric excess in liquid and solid phases.

Figure 6.3 also shows in panel (c) the evolution of the enantiomeric excesses in liquid and solid phases ( $ee_L$  and  $ee_S$ , respectively). This quantity indicates the difference in concentration between the two enantiomers. During PC, the enantiomeric excess in the liquid phase begins at zero, since the solution is a racemate.  $ee_L$  then reaches a maximum and decreases until equilibrium, when the solution becomes again racemic. For the solid phase, the enantiomeric excess starts at 100%, because of the chiral pure seeds of target compound, and depletes due to crystallization of the unwanted enantiomer.

## 6.7 General strategy to implement the SCM

In order to implement the shortcut model and estimate the free parameters, experimental data is required. First and foremost, solid/liquid equilibria and metastable zone width must be known at the potential temperature range of application. This data can be found in literature, if available, or it can be measured (Mullin, 2001). Then, preferential crystallization experiments must be successfully performed.

As showed in the model formulation (section 6.2), the SCM has three main parameters to be estimated: stop time  $t_{stop}$ , effective crystallization rate  $k^{eff}$  and effective order of

crystallization  $n^{eff}$ . The value of initial supersaturation  $S^0$  was chosen to correlate the parameters with experimental data. From equation 2.1,  $S^0$  is defined as:

$$S_i^0 = \frac{w_i^0}{w_{sat,i}^0} \quad i = 1,2 \quad (6.28)$$

The concentration of the initial solution is racemic, therefore the value of initial supersaturation is equal for both enantiomers:

$$S_1^0 = S_2^0 = S^0 \quad (6.29)$$

A minimum of three PC experiments with different initial supersaturation is required. They can be performed by keeping a constant crystallization temperature and applying a different saturation temperature at each experiment. For a first model evaluation, only one parameter should change. Other process conditions, e.g. mass and average size of the seeds, must be kept constant. Doing so, as it will be demonstrated later, the parameters  $t_{stop}$  and  $k^{eff}$  are functions of the initial supersaturation, and  $n^{eff}$  can be approximated as a constant. To further increase the range of applicability of the model, additional experiments with for instance different initial solid phase areas or different crystallization temperatures could be performed.

The application of an appropriate strategy serves to apply and parametrize the model in an simple and efficient manner. In this work, the PC experiments were performed by measuring the progress of the optical rotation angle in the liquid phase using a polarimeter. Based on that, the following strategy to estimate the SCM free parameters is proposed:

- 1) Calibrate a polarimeter to determine  $k_{pol}(T)$  (equation 6.21).
- 2) Perform experiments I, II and III for three different initial supersaturations  $S_I^0$ ,  $S_{II}^0$  and  $S_{III}^0$  at the same  $T_{cryst}$  and record the profiles of optical rotation angle  $\alpha_I(t)$ ,  $\alpha_{II}(t)$  and  $\alpha_{III}(t)$ .
- 3) Determine  $t_{stop}$  for each of the three experiments (see section 6.7.1.1).
- 4) Apply the SCM (equations 6.8, 6.9 and 6.14) to simulate the three experiments until the stop time, generating  $\alpha_{I,sim}[0, t_{stop_I}]$ ,  $\alpha_{II,sim}[0, t_{stop_{II}}]$  and  $\alpha_{III,sim}[0, t_{stop_{III}}]$ .
- 5) Estimate  $n^{eff}$  and the value of  $k^{eff}$  for each experiment ( $k_I^{eff}(S_I^0)$ ,  $k_{II}^{eff}(S_{II}^0)$  and  $k_{III}^{eff}(S_{III}^0)$ ) by minimizing the error between simulation and experiments (see section 6.7.1.2).

- 6) Correlate the three determined  $t_{stop}$  values with the initial supersaturation values  $S^0$  (equation 6.31).
- 7) Correlate the three determined  $k^{eff}$  values with the initial supersaturation values  $S^0$  (equation 6.34).

To help establishing the experimental conditions, step 2 can be divided into two stages. The first experiment is performed at one initial supersaturation and, depending on its results and on process specifications, higher or lower values of initial supersaturation can be chosen for the next procedures.

## 6.7.1 Calculation of SCM parameters

### 6.7.1.1 Stop time

The stop time  $t_{stop}$  delimits the duration to perform batch preferential crystallization without compromising product purity. As declared earlier, the aim of the shortcut model is to describe and predict this period only. After  $t_{stop}$ , the crystallization of the counter enantiomer is activated. This is implemented in the model equations by the discrete term  $F_2$ , called contamination factor (equation 6.12).

In a PC process, it is difficult to identify the exact time-point when nucleation of the counter enantiomer first occurs. In the liquid phase, the contamination of the solid product is perceived by a change in direction on the profile of optical rotation. This phenomenon indicates a depletion in the enantiomeric excess in solution, showing that the counter enantiomer is crystallizing and the solution concentration is advancing towards the racemic mixture. Therefore, the stop time is estimated relative to the maximum value of optical rotation  $\alpha_{max}$ . The  $t_{stop}$  must be in within the time interval to reach that maximum, that is  $[0, t(\alpha_{max})]$ , as indicated in Figure 6.4. To guarantee product purity, and at the same time maximize productivity, the stop time is characterized in this work by the time to achieve 90% of the maximum polarimetric signal.

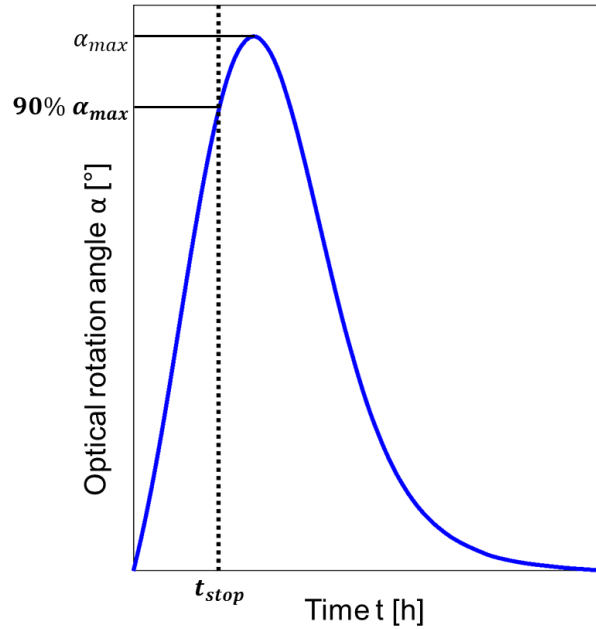


**Figure 6.4** Method to determine the stop time  $t_{stop}$  from a profile of optical rotation angle obtained during PC. The timespan for determination of  $t_{stop}$  is the interval  $[0, t(\alpha_{max})]$ . To avoid product contamination, the  $t_{stop}$  is selected as the time required to reach 90% of the maximum optical rotation  $\alpha_{max}$ .

The stop time is strongly affected by the initial supersaturation of the process. As predicted by nucleation theory, higher degrees of supersaturation are likely to induce earlier nucleation. Hence, the limiting conditions for the relation between these variables can be written:

$$t_{stop} = \begin{cases} 0 & S^0 \rightarrow \infty \\ \infty & S^0 = 1 \end{cases} \quad (6.30)$$

Based on these conditions, the following equation is proposed to predict the stop time for a given initial supersaturation:

$$t_{stop}(S^0) = \frac{a_t}{(S^0 - 1)^{b_t}} \quad (6.31)$$

where  $a_t$  and  $b_t$  are the correlation parameters. They can be determined by fitting the empirical equation to experimental data via least squares method.

Besides the dependency on supersaturation,  $t_{stop}$  is also influenced by the process setup. Hence, it is interesting to perform the PC experiments in the scale intended for production. In case that is not possible, the simulation results should be considered with care.

### 6.7.1.2 Effective crystallization rate constant and order of crystallization

The kinetic parameters of the SCM are the effective crystallization rate constant and the effective order of crystallization. The effective crystallization rate constant  $k^{eff}$  is the model parameter accounting for the overall mass transfer rate from the liquid phase to the solid phase. This constant integrates the effects of all mechanisms involved, comprehending both growth and nucleation. The  $k^{eff}$  is clearly influenced by the initial supersaturation. The rate of crystallization will be higher for processes initializing with higher supersaturation.

The effective order of crystallization  $n^{eff}$  is the exponent of the driving force term. It accounts for the nonlinear dependence of the mass transfer effects on supersaturation. The  $n^{eff}$  is approximated as a constant for a given crystallizing system (that is, pair of enantiomers and solvent) and a specific experimental setup. Therefore, it is assumed independent on the value of initial supersaturation.

These two parameters,  $k^{eff}$  and  $n^{eff}$ , compose the mass transfer equations in the SCM (equations 6.8 to 6.11 and 6.13). They must be determined experimentally. A well-known strategy to estimate equation parameters is the least squares method. This regression analysis is applied by minimizing the square of the differences between simulations and experimental data. Given a set of  $J$  measurements  $y_{exp}(t)$ , which are to be fitted to a curve  $y_{sim}(t)$ , the best set of parameters  $p$  are determined according to the following general objective function  $OF$ :

$$OF(p) = \min_p \sum_{j=1}^J (y_{exp} - y_{sim})^2 \quad (6.32)$$

For the set of three PC experiments proposed in the SCM (namely I, II and III), four variables need to be estimated:  $n^{eff}$ ,  $k_I^{eff}$ ,  $k_{II}^{eff}$  and  $k_{III}^{eff}$ . To optimize all parameters simultaneously, one of the possible solutions is to adopt a loop of minimizations. The experimental data  $\alpha_n(t)$ , consisting of  $J_n$  data points, where  $n \in I, II, III$ , contains the dynamic profiles of optical rotation angle until the respective stop time  $t_{stop_n}$ . The objective function to be minimized can be written as:

$$\begin{aligned}
OF(n^{eff}, k_I^{eff}, k_{II}^{eff}, k_{III}^{eff}) \\
= \min_{n^{eff}} \left[ \min_{k_I^{eff}} \sum_{j=1}^{J_I} (\alpha_I - \alpha_{I_{sim}})^2 + \min_{k_{II}^{eff}} \sum_{j=1}^{J_{II}} (\alpha_{II} - \alpha_{II_{sim}})^2 \right. \\
\left. + \min_{k_{III}^{eff}} \sum_{j=1}^{J_{III}} (\alpha_{III} - \alpha_{III_{sim}})^2 \right] \quad (6.33)
\end{aligned}$$

The simulated data  $\alpha_{n_{sim}}$  is calculated from the model equations for the target enantiomer (equations 6.8 and 6.9).

After estimating the values of effective rate constant, the next step is to correlate this parameter with the initial value of supersaturation. The set of experiments proposed to evaluate the model are performed at the same crystallization temperature. Therefore, the values of  $k^{eff}$  can be assumed to be dependent only on the initial supersaturation. In contrast to the stop time, which has a clear trend for changes in the initial supersaturation, the effective rate constant may vary with  $S_0$  in different manners. For sake of simplification,  $k^{eff}$  is assumed to be an overall rate constant, lumping several effects that generate the transfer in mass between liquid and solid phases. As a result, the empirical model to predict this parameter needs to be flexible enough to account for different effects that may occur. The following log-logistic distribution (Singh et al., 1993) is proposed:

$$k^{eff}(S^0) = a_k \frac{\left(\frac{b_k}{c_k}\right) \left(\frac{S^0 - 1}{c_k}\right)^{b_k - 1}}{\left(1 + \left(\frac{S^0 - 1}{c_k}\right)^{b_k}\right)^2} \quad (6.34)$$

where  $a_k$ ,  $b_k$  and  $c_k$  are the correlation parameters. They must be evaluated using the minimum of three experiments proposed to parametrize the SCM. Each initial supersaturation condition  $S_n^0$ ,  $n \in I, II, III$ , is associated with a value of  $k_n^{eff}$  determined with the objective function (equation 6.33).

The impact of temperature on the effective crystallization rate constant can be introduced to the correlation considering an Arrhenius approach:

$$k^{eff}(S^0, T) = k_0^{eff} e^{-\left(\frac{E^{eff}}{RT}\right)} \quad (6.35)$$

where  $E^{eff}$  is the activation energy,  $R_g$  is the universal gas constant and  $k_0^{eff}$  is the preexponential term, which is defined as:

$$k_0^{eff}(S^0, T) = a_{kT} \frac{\left(\frac{b_{kT}}{c_{kT}}\right) \left(\frac{S^0 - 1}{c_{kT}}\right)^{b_{kT}-1}}{\left(1 + \left(\frac{S^0 - 1}{c_{kT}}\right)^{b_{kT}}\right)^2} \quad (6.36)$$

The parameters  $a_{kT}$ ,  $b_{kT}$  and  $c_{kT}$  from equation 6.36 are different from  $a_k$ ,  $b_k$  and  $c_k$  of equation 6.34. The dependency of  $k^{eff}$  on temperature can only be evaluated if the set of experiments is realized in different crystallization temperatures.

## 6.8 Experimental evaluation

In this section, experimental data and theoretical results from the SCM are investigated to validate the model. The strategy described in section 6.7 was carried out to apply SCM and estimate the free parameters.

The model system studied was D-/L-asparagine monohydrate in water. Solubility data and metastable zone width found in literature (Petruševska-Seebach et al., 2009; Temmel et al., 2018) were showed in section 4.1. The L-enantiomer was selected as the target molecule. The solid phase forms a hydrate, thus the application of a solvent mass balance is necessary (equation 6.14). This characteristic of the solid phase must also be taken into consideration when calculating the saturation concentrations using the ternary phase diagram, as described in section 6.3.

Three experiments were performed with different initial supersaturations. Details on the experimental setup and procedures were provided in Chapter 4, section 4.3. The experimental conditions are given in Table 6.1. The results of experiments I to III were used to estimate the model free parameters  $t_{stop}$ ,  $n^{eff}$  and  $k^{eff}$ . The crystallization temperature was similar for these runs, but the saturation temperature varied. This created different starting conditions  $w_1^0$  and hence different driving forces at each experiment. The fourth experiment was performed at a different crystallization temperature to investigate the effect of temperature in the SCM parameters.

**Table 6.1** Summary of experimental conditions of preferential crystallization. Experiments I to III were used for parameter estimation. Experiment IV was applied to study the influence of temperature in SCM parameters. The initial solution was racemic ( $w_1^0 = w_{12}(T_{sat})/2$ );  $m_{seeds} = 0.2$  g, particle size 90-125 microns

( $R_1^0 = 53.7$  microns),  $V_L = 0.2$  l.  $w_1^0$  = initial conc. of target enantiomer (solubility at  $T_{sat}$ );  $w_{sat,1}^0$  was calculated from the TPD using  $w_{ratio}$ .

Experiment	$w_1^0$	$w_{sat,1}^0$	$S^0$	$T_{cryst}$	$T_{sat}$
	[10 <sup>2</sup> g g <sup>-1</sup> ]	[10 <sup>2</sup> g g <sup>-1</sup> ]	[-]	[°C]	[°C]
I	4.56	3.68	1.24	30	35
II	4.95	3.68	1.34	30	37
III	5.57	3.68	1.51	30	40
IV	3.68	2.93	1.26	25	30

The SCM equations were solved using MATLAB R2019b. In particular, the solver ode15 was applied to solve the ODE system and generate the simulations. The variables employed during simulations are listed in Appendix A.2. The table includes initial conditions for prediction of each experiment, as well as physical properties of the model system, such as molar mass and solid density.

### 6.8.1 Determination of model parameters

The SCM parameters estimated with the set of experiments I to III are indicated in Table 6.2. Figure 6.5 depicts the results of the respective correlations for  $t_{stop}$  and  $k^{eff}$  (equations 6.31 and 6.34). Represented in red are the experiments (symbols) and simulated results (solid curve) of the stop time over the initial supersaturation of the process. There is a good fit between experimental data and the empirical correlation. The values of the stop time decreased with increasing values of initial supersaturation. This is expected, since a stronger driving force for crystallization triggers earlier nucleation of the counter enantiomer.

The behavior of the effective crystallization rate constant over the initial supersaturation is shown in black in Figure 6.5. The values of estimated  $k^{eff}$  were significantly lower in the experiments starting with higher levels of supersaturation. The dotted lines show extrapolation of the correlation function outside of the  $S^0$  range of the experiments. The full empirical profile has a more complex shape than the one provided by the three experiments. This indicating the capability of the model to account for different crystallization kinetics. For instance, in the case of linear dependency on supersaturation, the values of effective rate constant would increase proportionally to those of the  $S^0$ . This scenario would be described by the left side of the curve  $k^{eff}(S^0)$ , before the maximum of the function. In this case, it is foreseen that the effective order of crystallization  $n^{eff}$  could be approximated to the unit. In fact, this case was observed and predicted by the SCM for the model system D-/L-threonine in water (Carneiro et al., 2019).

Crystallization of asparagine monohydrate promotes kinetic results away from linearity in the range of  $S^0$  tested. The determined value of  $n^{eff}$  was 6.10 (see Table 6.2). The values of the parameters  $n^{eff}$ ,  $k_I^{eff}$ ,  $k_{II}^{eff}$  and  $k_{III}^{eff}$  were fitted all together satisfying the objective function in equation 6.33.

**Table 6.2** Parameters of the shortcut model estimated with experimental data. The three sections indicate: calibration parameter (equations 6.21), ODE parameters and correlation parameters (equations 6.31 and 6.34).

Parameter	Experiment	Value	Unit
$k_{pol}$		0.048	$\text{g g}^{-1}$
$t_{stop}$	I	3.14	h
	II	1.37	h
	III	0.48	h
$n^{eff}$		6.10	—
$k^{eff}$	I	62.3	$\text{g h}^{-1} \text{cm}^{-2}$
	II	13.4	$\text{g h}^{-1} \text{cm}^{-2}$
	III	1.97	$\text{g h}^{-1} \text{cm}^{-2}$
$a_t$		0.095	h
$b_t$		2.46	—
$a_k$		20.8	$\text{g h}^{-1} \text{cm}^{-2}$
$b_k$		4.41	—
$c_k$		0.17	—

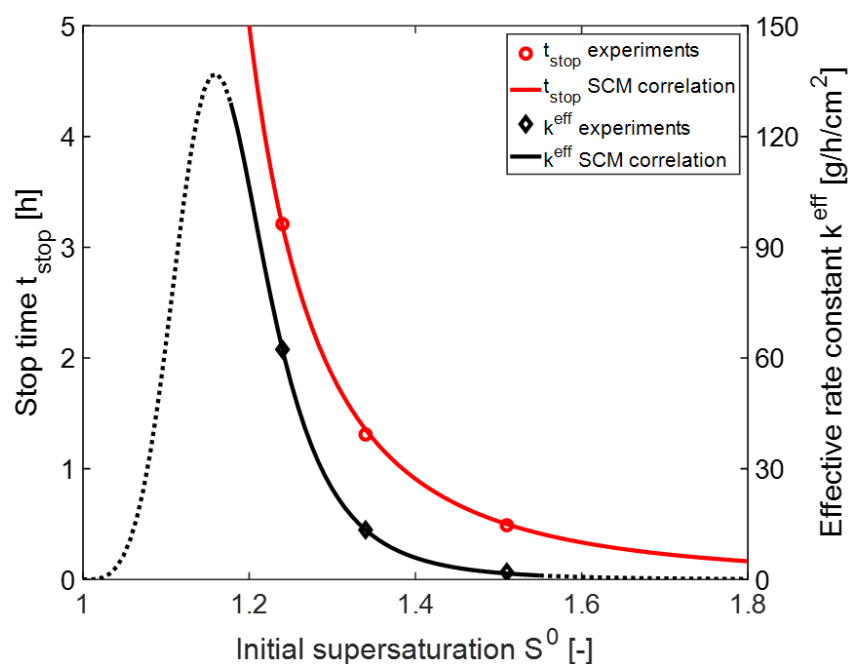


**Figure 6.5** SCM parameters as a function of initial supersaturation. In red:  $t_{stop}$ , in black:  $k^{eff}$ . Symbols are experimental points, curves are the correlation functions. Dotted lines are outside the experimental range of the correlation.

### 6.8.2 Model validation

The profiles of experimental investigation and SCM simulations are shown in Figure 6.6. The experiments are depicted in red. Each panel shows the output of a respective experimental condition:  $S_I^0 = 1.24$ ,  $S_{II}^0 = 1.34$  and  $S_{III}^0 = 1.51$ . The maximum optical rotation achieved, representing the maximum enantiomeric excess (see equation 6.23), increased for higher levels of initial supersaturation. This indicates that a greater amount of target enantiomer had crystallized. In batch PC, this also implies a shorter operating window for the process, as a consequence of the rapid arising of the counter enantiomer. The stop time was estimated relative to each maximum value of polarimetric signal (see scheme in Figure 6.4). It marks the beginning of contamination of the solid product in the SCM.

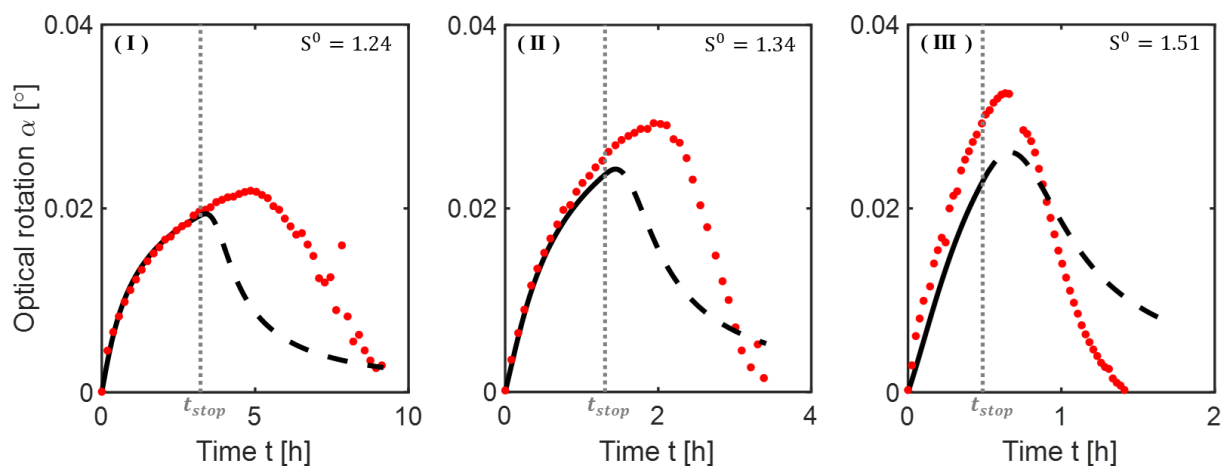


**Figure 6.6** Preferential crystallization, profiles of optical rotation angle over time. Experiments I, II and III (red dots) and SCM simulations (black curve) initiated with different initial supersaturation. Extrapolation of the SCM profile beyond stop time (dashed) is depicted for illustration and does not intend to fit the data.

During the period of interest, that is, until  $t_{stop}$ , the SCM results are in good agreement with the experiments. The dashed curves represent the simulations beyond that range, where the SCM profiles show large deviations from the experiments. This is expected, since only the data until  $t_{stop}$  was applied to estimate model parameters. The accuracy of the fitting was slightly different for the three profiles, and the results for the lower value of supersaturation (Figure 6.6 panel (I)) presented the best match between SCM simulations and experimental data. The different fittings is partially a consequence of the simultaneous optimization of the parameters  $k_I^{eff}$ ,  $k_{II}^{eff}$ ,  $k_{III}^{eff}$  and  $n^{eff}$ . For higher values of initial supersaturation, a more conservative prediction of the time profile was observed. This indicates a slight underestimation of productivity, which is a positive aspect in process design.

### 6.8.3 Influence of crystallization temperature on SCM parameters

The three experiments proposed to implement the SCM and presented in the previous section were performed at similar crystallization temperature. This was the strategy chosen to allow for simplification of the model. In this way, the empirical functions applied to describe the stop time and the effective crystallization rate were dependent only on initial supersaturation. When experiments are executed at different  $T_{cryst}$ , both  $t_{stop}$  and  $k^{eff}$  become also temperature dependent.

An additional PC experiment was performed to investigate the impact of crystallization temperature on the shortcut model parameters. Experiment IV (Table 6.1) was performed at  $T_{cryst} = 25^\circ\text{C}$  with saturation temperature of  $30^\circ\text{C}$ , generating a  $\Delta T = T_{sat} - T_{cryst} = 5\text{K}$ , which is similar to that of experiment I. The two experiments were consequently performed under comparable values of initial supersaturation, that is,  $S_I^0 = 1.24$  and  $S_{IV}^0 = 1.26$ . In this way, the effects of  $S^0$  can be neglected and the influence of temperature on the parameters can be analyzed.

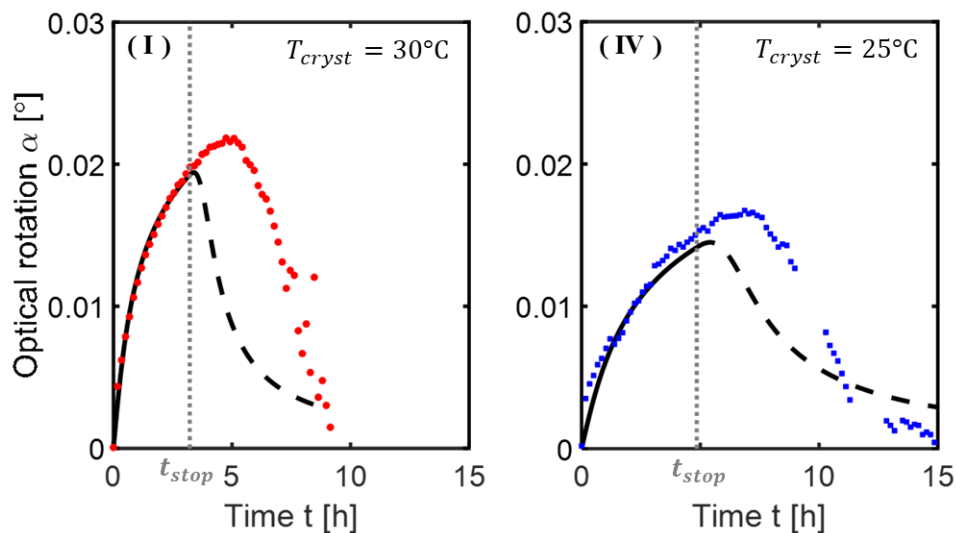


**Figure 6.7** Effect of crystallization temperature in the SCM parameters. Comparison between PC profiles of optical rotation angle over time from experiments I (in red,  $S_I^0 = 1.24$ ,  $T_{cryst} = 30^\circ\text{C}$ ) and IV (in blue,  $S_{IV}^0 = 1.26$ ,  $T_{cryst} = 25^\circ\text{C}$ ). Symbols are experimental data, solid curves are SCM simulated results and dashed curves are extrapolations of these predictions beyond stop time.

Figure 6.7 shows the results of experimental data and SCM simulations of runs I and IV. The left panel represents experiment I and the curves are identical to the ones presented in Figure 6.6 (a). Experiment IV is depicted in in blue in righthand side panel. The respective stop time was estimated as described in section 6.7.1.1. The effective crystallization rate from

experiment IV was determined by fitting the SCM to the experimental data using MATLAB least squares minimization tool `fmincon`. The value of effective order of crystallization was kept the same as the one previously estimated (Table 6.2). The parameters determined for both experiments can be compared in Table 6.3.

**Table 6.3** Comparison between stop time (Figure 6.4) and effective crystallization rate (equations 6.34 and 6.35) estimated at different conditions of crystallization temperature.  $T_{cryst} = 30$  and  $25^\circ\text{C}$  for experiments I and IV, respectively.

Parameter	Experiment	Value	Unit
$t_{stop}$	I	3.14	h
	IV	4.85	h
$k^{eff}$	I	62.3	$\text{g h}^{-1} \text{cm}^{-2}$
	IV	16.3	$\text{g h}^{-1} \text{cm}^{-2}$
$E^{eff}$		201	$\text{kJ mol}^{-1}$
$k_0^{eff}$		$3.27 \times 10^{36}$	$\text{g h}^{-1} \text{cm}^{-2}$

The process I with higher crystallization temperature achieved higher values of optical rotation angle, or corresponding to the enantiomeric excess in solution (equation 6.23). This resulted in an earlier stop time. Even though the initial supersaturation in both experiments was similar, the experiment IV performed at lower  $T_{cryst}$  presented a lower crystallization rate. This temperature effect is likely a consequence of the level of agitation and collision of the molecules (Jacques et al., 1994). This can be for instance described by the Arrhenius approach, as suggested in equation 6.35. The values of activation energy  $E^{eff}$  and preexponential factor  $k_0^{eff}$  were estimated from experimental data I and IV and are shown in Table 6.2. The results give an indication of the magnitude of the effect of temperature on the SCM parameters. For a detailed qualitative study, a minimum of three experiments in different  $T_{cryst}$  would be necessary. This discussion will not be treated in this thesis.

#### 6.8.4 Process performance: evaluation of productivity

To demonstrate the potential of the SCM in process design, productivity for production of pure L-asparagine was estimated at a range of initial supersaturations. The productivity was calculated using equation 6.24. The dead time  $t_{dead}$  was stipulated at 1 h. The total liquid phase volume  $V_L$  was 200 ml, same scale of the crystallizer used during experiments. Figure 6.8 shows the results of the effect of mass of seeds on process productivity. In order to have comparable estimations, the seed mass (equation 6.17) was normalized by the maximum theoretical L-asparagine solid product that can be achieved, namely  $m_{S_{max,1}}$ . This quantity was calculated by

$m_{S_{max,1}} = m_{S_{max}}/2$ , where  $m_{S_{max}}$  is the thermodynamic maximum amount of racemic solid that can be crystallized (see equation 6.26). The maximum target solid product  $m_{S_{max,1}}$  was determined for each discrete initial supersaturation ( $S^0 = w_1^0/w_{sat,1}^0$ ). The initial saturation composition was calculated from extended solubility at crystallization temperature using the TPD, as described in section 6.3. The values of seed mass were chosen in the range from 1% to 10% of the maximum product  $m_{S_{max,1}}$ , which is an acceptable range applied in the industry.

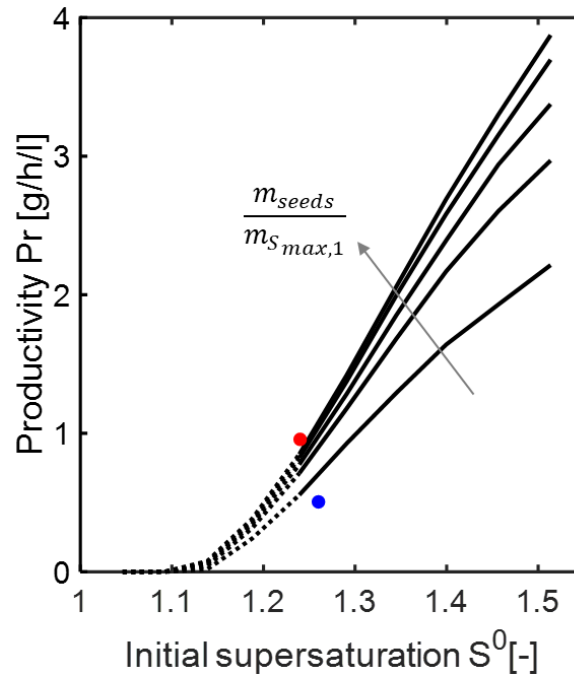


**Figure 6.8** Productivity estimated using SCM and evaluation of impact of seed mass. Each curve represents a ratio  $m_{seeds}/m_{S_{max,1}}$ : 0.01, 0.03, 0.05, 0.08 and 0.10, corresponding to mass of seeds in the range of 1 to 10% of the maximum solid product.  $T_{cryst} = 30^\circ\text{C}$ . Red and blue circles indicate the productivity estimated for experiments I and IV, respectively.

The simulation results showed that lower values of  $S^0$ , that is when the driving forces for crystallization are rather low, lead to productivity close to zero (see Figure 6.8). By increasing the levels of initial supersaturation, there is a significant increase in productivity. For  $T_{cryst} = 30^\circ\text{C}$  and initial supersaturation above 1.2, the productivity of isothermal batch preferential crystallization predicted with the SCM for resolving D-/L-asparagine lies between 0.5 to 4.0 g/h/L. The results are in accordance with values reported in literature (Chaaban et al., 2013). All productivity curves showed in Figure 6.8 were generated with the parameters estimated by the process transients I to III. To evaluate PC at a different temperatures of crystallization, the productivity of experiments I and IV are indicated in Figure 6.8 in red and blue symbols, respectively. The correspondent results are  $Pr_I = 0.96 \text{ g/h/L}$  and  $Pr_{IV} = 0.50 \text{ g/h/L}$ . As expected,

conducting the enantioselective crystallization under similar  $\Delta T$  but lower  $T_{cryst}$  had a significant impact on process productivity.

The results reveal that carrying out the process at higher crystallization temperature culminates in improved productivity. Conditions of high supersaturation are, however, difficult to perform experimentally. Due to the proximity to the limits of the metastable zone, the process becomes unstable and undesired primary nucleation can occur. For asparagine monohydrate, the MSZ width at  $T_{cryst}$  of 30°C is approximately at  $S^0 = 1.5$ . This value changes according to the compound and process conditions.

The results depicted in Figure 6.8 also show that higher productivity values can be achieved with higher amount of seeds. Increasing the seed mass corresponds to higher crystal surface area during crystallization. This effect tends to accelerate the process and result in higher productivities (Alvarez Rodrigo et al., 2004). A similar result can be expected when changing the average size of crystals (Elsner et al., 2011). A consequence of the rapid crystallization is the higher probability of nucleation of the counter enantiomer. The design of a cost-effective preferential crystallization process must undergo the compromise between investment in seed mass, improvement in productivity and drop in robustness.

To estimate the productivity, the stop time was assumed to be independent from the seed mass. This hypothesis might only be valid in a limited range outside the reference experiments. The model application can be broadened if additional experiments are performed in range of size and mass of seeds.

## 6.9 Coupling Preferential Crystallization and enzymatic racemization

Coupling preferential crystallization with racemization has the potential to improve performance of the production of pure enantiomers. In the present section, an extension of the shortcut model to account for this process integration and allow for evaluation of key performance indicators is discussed. Various possible configurations for the coupling of batch PC and enzymatic racemization were considered in section 5.6. Two of the process schemes are investigated in the following: one-unit and two-unit configurations. Figure 6.9 illustrates the two process variants.

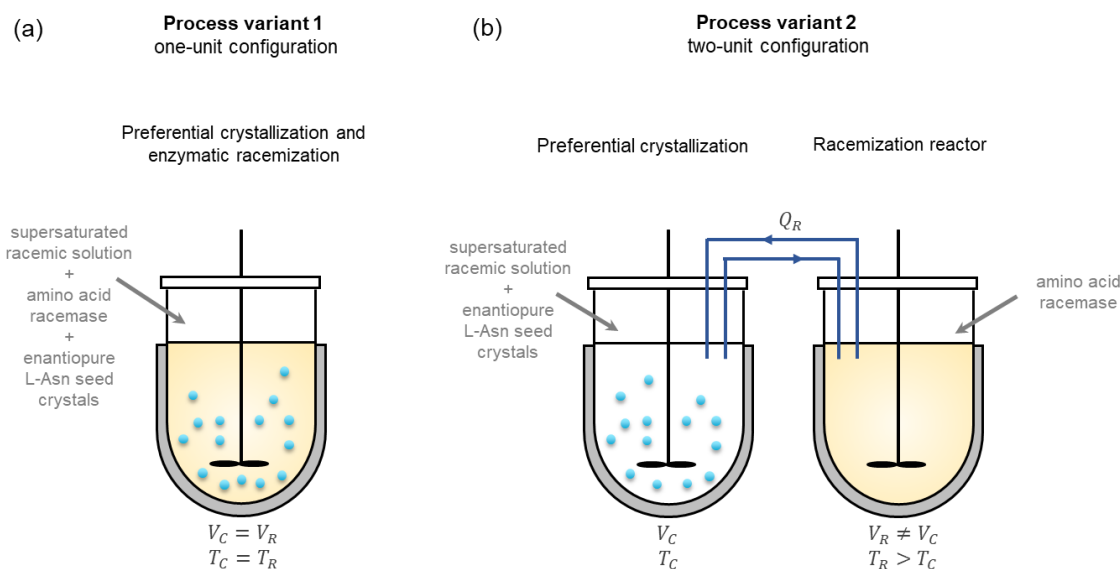


**Figure 6.9** Scheme of the two process variants of preferential crystallization integrated with enzymatic racemization investigated with the shortcut model.

### 6.9.1 Process variant 1: one-unit configuration

In the first process configuration, crystallization and racemization take place in the same vessel (Figure 6.9 a). The stirred tank is initially filled with supersaturated racemic mother liquor and the enzyme preparation is added to the solution. The reaction is in equilibrium with the solution since there is no difference in concentration between the enantiomers. After seeding with enantiopure crystals, crystallization of the target enantiomer takes place and the catalyst converts the excess of counter enantiomer created in solution into the target molecule.

The changes of mass in the liquid phase  $m_i$  are generated by the transfer of material to the solid phase, expressed by the overall mass transfer rate  $\overline{GB}_i^{eff}$  (equation 6.3), and the rate of racemization reaction  $r_R$  (equation 3.35). The resultant equations for the target and counter molecules are given:

$$\frac{dm_1}{dt} = -\overline{GB}_1^{eff} + \nu_1 V_R D_C r_R \quad (6.37)$$

$$\frac{dm_2}{dt} = -\overline{GB}_2^{eff} + \nu_2 V_R D_C r_R \quad (6.38)$$

The variable  $\nu_i$  is the stoichiometric coefficient of each stereoisomer. Since the target enantiomer is the product of the reaction and the counter enantiomer is the reaction substrate,  $\nu_1 = 1$ , and  $\nu_2 = -1$ . The quantity  $V_R$  is the reaction volume, which in the described one-pot

process configuration is equal to the total liquid phase volume  $V_L$ . The product between the catalyst dosage  $D_C$  (defined in equation 3.39) and the rate  $r_R$  gives the reaction velocity in grams per hour per volume at which the racemization takes place. The rate of mass transfer in the liquid phase given by equations 6.37 and 6.38 can be rearranged using the expression for  $\overline{GB}_i^{eff}$  (equation 6.3) as the following:

$$\frac{dm_1}{dt} = -k^{eff} 4\pi N_1 R_1^2 (S_1 - 1)^{n^{eff}} + V_R D_C r_R \quad (6.39)$$

$$\frac{dm_2}{dt} = -F_2 k^{eff} 4\pi N_2 R_2^2 (S_2 - 1)^{n^{eff}} - V_R D_C r_R \quad (6.40)$$

The reaction is assumed to have no effect on the growing particles. So, the mass balance for the solid phase remains as described for the process without racemization (equations 6.9 and 6.11). The same is valid for the rate of changes in the mass of solvent (equation 6.14). Hence, the system of ODEs formulated with the SCM to describe the coupling of PC and racemization in the spatially integrated configuration is composed by the equations 6.39, 6.40, 6.9, 6.11 and 6.14.

The kinetic model for enzymatic racemization is described by the reversible Michaelis-Menten mechanism, as discussed in section 3.3. Since the crystallization is evaluated in the SCM in terms of mass fractions, the reaction rate must be calculated accordingly. The enzyme kinetics can be rearranged using molar mass of substrate and solution density. The racemization rate as a function of mass fractions is given by:

$$r_R = \frac{V_{max} \rho_L (w_2 - w_1)}{K_M + \rho_L (w_1 + w_2)} \quad (6.41)$$

Similarly, the modified reaction rate accounting for substrate inhibition effects is given by:

$$r_R = \frac{V_{max} \rho_L (w_2 - w_1)}{K_M + \rho_L (w_1 + w_2) + \frac{\rho_L^2 w_2 (w_1 + w_2)}{K_I}} \quad (6.42)$$

In equations 6.41 and 6.42,  $r_R$  is given in g/h/L, the maximum velocity  $V_{max}$  is in g/h/L, the kinetic parameters  $K_M$  and  $K_I$  are in g/L and the density of the liquid phase  $\rho_L$  is in g/L.

### 6.9.2 Process variant 2: two-unit configuration

In the second studied coupling scheme, preferential crystallization and racemization take place in separated units (Figure 6.9 b). Each vessel is of stirred tank type. The reactor can be model as a single unit or a cascade of tanks containing either free enzyme in solution or in immobilized form. The processes are integrated in batch mode with an online bypass of fixed flow rate. Crystal-free and enzyme-free solution is pumped between the units. The outlet stream of the crystallizer is the inlet of racemization tank and vice-versa. The racemization reactor is assumed to operate at a higher temperature than the saturation temperature to avoid crystallization. It is assumed that no crystallization occurs outside the crystallizer.

The material transport between the units must be accounted for both enantiomers (index 1 = target enantiomer and 2 = counter enantiomer) and the solvent (index 3). For each component, there are two sets of mass balance equations: one for the crystallization unit (subscript C) and one for the racemization unit (subscript R). The rate of mass changes in the crystallizer are calculated from the depletion in mass caused by preferential crystallization and the changes due to transport of material in and out of the unit:

$$\frac{dm_{1C}}{dt} = -k^{eff} 4\pi N_1 R_1^2 (S_1 - 1)^{n^{eff}} + Q_R (w_{1R} - w_{1C}) \quad (6.43)$$

$$\frac{dm_{2C}}{dt} = -F_2 k^{eff} 4\pi N_2 R_2^2 (S_2 - 1)^{n^{eff}} + Q_R (w_{2R} - w_{2C}) \quad (6.44)$$

$$\frac{dm_{3C}}{dt} = - \left( \begin{array}{c} k^{eff} 4\pi N_1 R_1^2 (S_1 - 1)^{n^{eff}} \\ + \\ F_2 k^{eff} 4\pi N_2 R_2^2 (S_2 - 1)^{n^{eff}} \end{array} \right) \left( \frac{M_S}{M_i} - 1 \right) + Q_R (w_{3R} - w_{3C}) \quad (6.45)$$

The mass flow rate  $Q_R$  is given in grams per hour. The mass fractions  $w_{iC}$  and  $w_{iR}$  ( $i \in \{1,2,3\}$ ) are the outlet compositions of component  $i$  leaving the crystallizer and the racemization reactor, respectively.

The set of component mass balance equations for the racemization unit accounts for the racemization and the bypass streams:

$$\frac{dm_{1R}}{dt} = V_R D_C r_R - Q_R (w_{1R} - w_{1C}) \quad (6.46)$$

$$\frac{dm_{2R}}{dt} = -V_R D_C r_R - Q_R (w_{2R} - w_{2C}) \quad (6.47)$$

$$\frac{dm_{3R}}{dt} = -Q_R (w_{3R} - w_{3C}) \quad (6.48)$$

The reaction rate  $r_R$  is as described above in equation 6.41 (or equation 6.42, if inhibition effects are present). Similarly to process variant 1, the mass balance for the solid phase remains as described for the process without racemization (equations 6.9 and 6.11). The SCM system of equations to describe the two-unit coupling of preferential crystallization and racemization (Figure 6.9) is given by the equations 6.43 to 6.48, 6.9, and 6.11.

## 6.10 Results of performance assessment of coupled process

The performance of coupled preferential crystallization and enzymatic racemization for the production of pure L-asparagine was estimated using the extended shortcut model. Productivity and yield were assessed for the two process variants (Figure 6.9) in different coupling scenarios. The main results are discussed in the following. A detailed description of results, trends, and influence of coupling parameters are provided by (Bhandari et al., n.d.).

The enantiomeric resolution was simulated under the same conditions of PC experiment I, as given in Table 6.1. The corresponding estimated parameters of the SCM were showed in Table 6.2. The density of DL-asparagine solution was calculated by equation 4.2 using the liquid phase composition and crystallization temperature. Kinetic data of the amino acid racemase in both free and immobilized form were previously determined from experiments (see Chapter 5). The concentration and time units of the kinetic parameters were converted to stay consistent with mass balances of the shortcut model. Table 6.4 gives the values of the AAR kinetic parameters employed in the SCM simulations. The catalyst dosage was fixed at 30 mg-enzyme per ml of reaction. For an immobilization load of 35 mg-enzyme/g-support, that is equivalent to 0.9 g-support of immobilized amino acid racemase per ml of reaction.

**Table 6.4** Kinetic parameters of the amino acid racemase applied in the shortcut model simulations (parameters of equations 6.41 and 6.42). The units of parameters showed in Tables 5.1 and 5.3 were converted from moles per minute to grams per hour.

AAR	T [°C]	$V_{max}$ [10 <sup>2</sup> g h <sup>-1</sup> mg-enzyme <sup>-1</sup> ]	$V_{max}$ [10 <sup>2</sup> g h <sup>-1</sup> g-support <sup>-1</sup> ]	$K_M$ [10 <sup>2</sup> g ml <sup>-1</sup> ]	$K_I$ [10 <sup>2</sup> g ml <sup>-1</sup> ]
Free	30	18		0.6	3.1
Free	40	24		0.3	6.6
Immobilized	40	30	1038	2.6	-

Table 6.5 summarizes the predicted productivity (equation 6.24) and yield (equation 6.25) of the following process configurations: single PC (named process variant 0), coupled PC and racemization in one vessel (process variant 1, Figure 6.9), coupled PC and racemization in separate units (process variant 2, Figure 6.9). The SCM system of differential equations for all process variants was solved using MATLAB.

**Table 6.5** Performance results of preferential crystallization simulated with the SCM. PC conditions were similar to Experiment I, Table 6.1.  $T_{cryst} = 30$  °C,  $V_L = 0.2$  l,  $D_C = 30$  mg-enzyme/ml or 0.9 g-support/ml (immobilization load 35 g-support/mg-enzyme). Process variant 0: single PC. Process variant 1: coupled process, single unit;  $V_R = V_L$ ,  $T_R = T_{cryst}$ . Process variant 2: coupled process, separated units;  $T_R = 40$  °C,  $V_R = 2$  ml,  $Q_R = 3.5$  ml/min.

Simulation	Process variant	AAR preparation	$t_{stop}$ [h]	Purity $Pu$ [%]	Yield $Y$ [%]	Productivity $Pr$ [g/h/L]
1	0	none	3.14	100	22	0.96
2	1	free	3.14	100	28	1.18
3	2	free	3.14	100	26	1.11
4	2	immobilized	3.14	100	30	1.27
5	0	none	1.10	100	15	1.24
6	2	immobilized	1.50	100	19	1.39
7	2	immobilized	13.5	95	51	0.39

Simulation 1 is the reference case chosen to evaluate the resolution of D/L-asparagine enantiomers. It corresponds to the performance results of single PC (process variant 0). The productivity and yield were predicted at  $t_{stop} = 3.14$  h, which was found based on experimental data (see section 6.7.1). This process time was determined to assure 100% product purity. The single PC resulted in productivity of 0.96 g/h/L and 22% yield. As expected, the coupled processes (variants 1 and 2) simulated over the same process time, i.e. same  $t_{stop}$ , resulted in higher productivities in comparison to the reference case. The presence of *in situ* racemization carried out with the free soluble enzyme (simulation 2, Table 6.5) produced an increase in 23% in productivity and 27% in yield. In this coupling configuration, both processes are held at the same temperature and reactor volume. The coupled preferential crystallization and racemization in separated configuration (variant 2) gives the possibility of operating each vessel under distinct conditions. This process scheme is more suitable for process intensification. On the other hand, the exchange of the fluid phase may delay the reaction in comparison to the one-vessel process and hinder the performance of the chiral resolution.

The impact of free and immobilized racemase was investigated in the separated units configuration (simulations 3 and 4 in Table 6.5). Similar conditions of reactor volume, exchange flow rate, temperature, and enzyme dosage were chosen for both cases. The values were selected based on experimental conditions performed with the AAR packed bed reactor (see Table 4.4).

A complete investigation of the optimum coupling conditions regarding each enzyme preparation was out of the scope of this thesis. The immobilized amino acid racemase was simulated in a cascade of three stirred tank reactors as an approximation to the behavior of the packed bed configuration. Productivity values of 1.27 and 1.11 g/h/L were predicted for the enantiomeric resolution coupled with immobilized and free racemase, respectively. The simulated yield resulted in 30% with the immobilized preparation and 26% with the free racemase. The coupled preferential crystallization using immobilized amino acid racemase outperformed the one with free enzyme. The results of simulations 1 and 4 indicate that the coupling of PC with the immobilized AAR results circa 32% and 36% increase in productivity and yield, respectively, in comparison to single PC. The kinetics of free soluble AAR suffered from inhibition effects at high concentrations of asparagine (see Chapter 5), resulting in lower reaction rates under the simulated process conditions. The inhibited kinetics was overcome upon immobilization of the racemase.

Performance of preferential crystallization can be improved by optimization of the process duration. The productivity and yield estimated in simulations 1 to 4 were calculated using the stop time suitable for the PC without racemization. By coupling the processes, the actual time window to produce enantiopure solids is larger, for the racemization contributes to the depletion in supersaturation of the counter enantiomer and delays its nucleation and growth. Hence, the yield estimations calculated by simulations 1 to 4 are rather conservative values. Higher yields may be achieved if the stop time is revised according to the coupled process. The same trend is not to be expected for productivity. An evaluation of the impact of the stop time allowed to predict an optimum operating condition to maximize productivity. The results obtained with the SCM suggest that optimizing the operating time of single PC ( $Pr = 1.24$  g/h/L) has an analogous impact on the process productivity as the coupled PC and racemization calculated over the previously determined stop time ( $Pr = 1.27$  g/h/L). An optimum operating time also exists for the integrated process. The coupled PC and racemization simulated over a period of 1.5 h resulted in productivity of 1.39 g/h/L (simulation 6). Clearly, the improve in productivity comes at the expense of accepting yield loss from 30% to 19%.

The specification of product purity also plays an important role in the performance of the process. The simulations 1 to 6 were performed to obtain L-asparagine with 100% purity. If the purity requirements are relaxed to 95%, the results reveal an overall rise in yield of approximately 130% when comparing PC coupled with immobilized AAR (simulation 7) and

the reference case (simulation 1). By specifying a lower purity value, the process is extended for a much longer period, that is 13.5 h. This results in a significant drop in productivity.

## 6.11 Summary and outlook

Preferential crystallization is a powerful unit operation for separation and purification of chiral molecules. It allows the direct crystallization of a single conglomerate-forming enantiomer starting from a racemic solution. A quantitative description of PC requires considering thermodynamic features, fluid and particle mechanics and a detailed understanding of kinetics of crystallization. Despite the intricacy, preferential crystallization is ultimately a mass transfer process. The shortcut model described in this chapter was developed based on that characteristic. This novel rather simple and user-friendly model aims at predicting KPIs of PC in a simplified manner, based on overall mass transport rates between the two phases and the discrete activation of “nuclei” particles of the antipode to mimic contamination of the solid product.

The capability of the SCM in assessing productivity of batch isothermal preferential crystallization of conglomerates was demonstrated successfully for asparagine monohydrate enantiomers. The model assumptions, formulation, implementation strategy and experimental evaluation were discussed in detail. It could be showed that a minimum of three successful PC experiments are required to implement the three model parameters: stop time, effective crystallization rate and order of crystallization. The empirical functions describing the  $t_{stop}$  and  $k^{eff}$  were designed to be dependent only on the initial supersaturation. The SCM was evaluated with PC experiments performed at similar crystallization temperature. The simulation results showed good agreement with the experimental data applied for model estimation until the stop time. In that period, only three equations of the SCM are required: mass balance of the target enantiomer in liquid and solid phases and the mass balance for the solvent, since asparagine forms a monohydrate in the solid phase. This is the period used for estimation of performance of PC. Beyond the desired process duration, that is  $t > t_{stop}$ , the SCM requires two additional equations to account for the crystallization of the counter enantiomer. In that second period of the process, a large deviation between model and experiment is accepted.

The effect of seed mass strategy on productivity was investigated with the SCM. For production of pure L-asparagine, the results showed estimated productivity from 0.5 to 4.0 g/h/L. It was also found that with rising values of initial supersaturation, the impact of seed

mass on productivity is higher. An extension of the SCM to simulate coupled PC and enzymatic racemization allowed assessment of productivity and yield. The kinetic behavior of racemization used in the simulations was obtained from experimental investigation of the amino acid racemase (see Chapter 5). The estimated productivity values were in the range from circa 1.1 to 1.4 g/h/L, varying according to process conditions: coupling configuration, enzyme preparation, and process duration. A comparison between single PC ( $Pr = 0.96$  g/h/L,  $Y = 22\%$ ) and PC coupled with immobilized AAR in separate vessels ( $Pr = 1.27$  g/h/L,  $Y = 30\%$ ) resulted in 32% increase in productivity and 36% increase in yield. At the expense of loss in process yield, productivity may increase up to 1.39 g/h/L if duration of the process is optimized.

As demonstrated, coupling preferential crystallization and enzymatic racemization can provide a significant improvement in the performance of the resolution process. This process integration is an attractive alternative, particularly if there is no economical interest in the counter enantiomer. When both enantiomers are valuable, continuous PC has been shown to be a great opportunity for process improvement. A comprehensive overview of performance of continuous crystallization resolving conglomerates was reported in ref (Koellges & Vetter, 2018). Particularly for preferential crystallization, productivity values were in the range up to 15 g/h/L for a variety of compounds. Recently, Gaensch and coworkers described unprecedented productivity results up to 90 g/h/L for the production of asparagine enantiomers (Gänsch et al., 2021). Preferential crystallization was held continuously in conical shaped fluidized bed crystallizers. Among the studied factors, the authors reported the placement of sensor for product withdraw strategy to show the strongest potential for performance optimization.

A relevant limitation of the SCM compared to PBE is the inability to describe the crystal size distribution. However, the SCM allows comparing PC with other resolution processes, such as preparative chromatography, temperature cycling and Viedma ripening. For instance, chromatography reaches typical productivities of 1 to 15 kg of pure enantiomers per kg of stationary phase per day (Blehaut et al., 2012). A broader and thorough comparison between these enantioselective separation processes has not yet been described in literature.

Finally, the shortcut model succeeded in the relatively fast acquisition of key performance indicators because isothermal batch preferential crystallization is a rather simple process. The model development and the results showed here form a basis for the design and optimization of batch PC and its combination with enzymatic racemization. An ongoing study is investigating the extension of the SCM for continuous process variants and the resolution of enantiomers

forming racemic compounds. For crystallization processes involving more complex mechanisms, for instance, of agglomeration and breakage, additional assumptions and parameters must be considered to estimate performance indicators. Furthermore, the SCM parameters would likely need adjustment when developing a scale-up strategy.

## 7 Concluding Remarks

Preferential crystallization is a straightforward and efficient separation technique for the production of optically pure substances. It can be applied to the direct resolution of enantiomers crystallizing as conglomerates, and it has relevant applications in life sciences industries in particular for pharmaceuticals (Coquerel, 2006; Lorenz & Seidel-Morgenstern, 2014). A major drawback of PC is the maximum yield limited to 50%. Intensive research has been reported towards application and improvements of PC, focused on, but not limited to, development of new setup configurations, continuous operation, control of crystal size distribution and crystal shape, as well as on the screening, discovering and formation of new conglomerates. While much advance has been done and further developments on PC are expected, it has been pointed out that few studies describe details regarding performance parameters. Recent works have highlighted the importance to stimulate research activities with emphasis on the quantitative provision of performance criteria such as productivity, yield and purity (Koellges & Vetter, 2018; Lorenz & Seidel-Morgenstern, 2020).

In this context, this dissertation was dedicated to study the development of efficient enantioselective resolution via preferential crystallization by two means: investigation of an enzymatic unit for racemization to improve yield and robustness of PC, and the assessment of performance parameters in early stages of process design with a novel, simplified but efficient tool.

The development of an enzymatic racemization unit suitable for improvement of preferential crystallization was studied for an amino acid racemase (EC 5.1.1.10). Previously, a proof of principle had been demonstrated for PC with *in situ* soluble AAR for the provision of pure L-asparagine (Würges et al., 2009a). In the present work, the racemase production and purification procedures were improved. The results showed that, despite the presence of inhibition effects,  $V_{max}$  values rose 7 to 12-fold and  $K_M$  values decreased 1.5 to 5-fold, resulting in more efficient enzymatic activity.

The racemase activity was investigated under operating conditions similar to preferential crystallization. The large importance of the initial enantiomeric excess on the reaction rate was evaluated and highlighted. The excess of counter enantiomer in solution generated by PC is rather low, producing low driving force for racemization. This fact is crucial in designing the

integrated process. Since the biocatalyst production can be time and resource consuming, enough material should be available with adequate activity and stability in order to achieve the desired performance. A strategy for immobilization of the AAR was studied on affinity and covalent supports. While the immobilization on the most promising affinity carrier was similarly active and technically more practical to execute than the covalent support ECR 8309, the covalent binding provided better stability, an important feature for the desired application. The behavior of the enzymatic column reactor packed with immobilized AAR was validated under conditions expected in a coupled process with PC. The packed bed reactor provided rapid racemization, capable of full conversion under 1 minute residence time. The reactor performance was successfully predicted by simulations using kinetic parameters estimated from results of batch runs. The high stability and high activity of the racemization reactor show the potential of the studied immobilized amino acid racemase to be efficiently used in combination with PC and other enantiomeric resolution techniques. Advantages and challenges of several coupling configurations were discussed considering aspects of practical experimental execution.

In the second part of this thesis, a novel shortcut model (SCM) independent from population balance equations was developed in cooperation with a fellow doctoral researcher to predict the performance of isothermal batch preferential crystallization. The SCM requires only two ODEs to describe anhydrous enantiomers, or three ODEs in case the chiral substance forms crystalline solvates. Two additional mass balance equations for the counter enantiomer are postulated, but they are not required to describe the PC process until the point of purity drop. The development of the SCM was possible thanks to practical assumptions leading to the formulation of the model equations. The model explores the overall mass transfer effects between the solid and liquid phases, lumping the most relevant aspects of crystallization into a couple of key parameters. An important feature of the SCM is its restriction to the first period of preferential crystallization, until a stop time is reached, i.e. before contamination of the solid product. The simplicity of the model comes at the expense of not being able to describe the full crystal size distribution. Clearly, prior to the model application reliable knowledge for description of solid-liquid equilibria (solubility and metastable zone) at the desired temperature range of application is needed. These data are applied to the SCM simulations to determine the saturation mass fractions using the ternary phase diagram.

An approach to estimate the three model parameters of the SCM with a minimum number of three experiments was proposed, demonstrated and validated for PC of asparagine

enantiomers. The role of initial supersaturation in the process performance was highlighted in the sub-models of parameters and in the evaluation of process productivity. The possibility to include the crystallization temperature as a varying parameter at the expense of additional experiments was also demonstrated and discussed. The model formulation to simulate enzymatic racemization with PC was established for two process configurations: single-unit setup, in which the processes are held in the same vessel, and two-unit setup, where the processes take place in separated units. Experimental data obtained for the amino acid racemase kinetics was used in the simulations.

The results from the shortcut model showed that the coupled PC and racemization can indeed exceed not only the yield but also productivity of single PC for the production of L-asparagine. The best performance was found using the immobilized AAR in the two-unit process variant. Yield and productivity increased by 36 and 32%, respectively. Varying the process time or relaxing purity specifications could improve each KPI individually, but loss in the other performance parameter must be accepted. Such a productivity investigation for the coupling of PC and enzymatic racemization for production of pure enantiomers had not been reported before (Oketani et al., 2018). Future optimization of coupling conditions can lead to further improvements in yield and productivity. It must be stated that the productivity of preferential crystallization integrated with enzymatic racemization is still far from what can be achieved, for instance in a continuous PC process (Gänsch et al., 2021). However, the integrated variant is attractive in case only the target enantiomer is economically interesting.

The tools developed in this work provide instructive insight for the design and improvement of preferential crystallization in future studies. The highly active amino acid racemase has the potential to improve PC and also to be applied on other purification processes such as temperature cycling deracemization (Intaraboonrod et al., 2020) and chromatography (Harriehausen et al., 2021). The SCM enables a relatively quick estimation of key performance indicators of preferential crystallization. Studies were already initiated to extend the SCM for more complex process alternatives, such as continuous process and the resolution of compound-forming systems. Further relevant foreseen application is the comparison between PC and other enantioselective resolutions, for instance, preparative chromatography, deracemization via ripening or temperature cycles. A broad assessment between these processes has not been described in literature so far. The evaluation of performance parameters of other process options should also stimulate future studies to perform required economic analysis. Such investigations

will then definitely contribute to enlarge the spectrum of industrial applications of preferential crystallization efficiently separating enantiomers.

## References

- Adamíková, J., Antošová, M., & Polakovič, M. (2019). A Method of Early Phase Selection of Carrier for *Aspergillus Oryzae*  $\beta$ -Galactosidase Immobilization for Galactooligosaccharides Production. *Biotechnology Journal*, 14(3), 1800120.
- Ali, I. (2007). Homochiral Drug Design and Development by Racemization. *Combinatorial Chemistry & High Throughput Screening*, 10(5), 326–335.
- Alvarez Rodrigo, A., Lorenz, H., & Seidel-Morgenstern, A. (2004). Online monitoring of preferential crystallization of enantiomers. *Chirality*, 16(8), 499–508.
- Andreassen, J.-P., & Lewis, A. E. (2017). Classical and Nonclassical Theories of Crystal Growth. I: A. E. S. Van Driessche, M. Kellermeier, L. G. Benning, & D. Gebauer (Eds.), *New Perspectives on Mineral Nucleation and Growth: From Solution Precursors to Solid Materials* (pp. 137–154). Springer International Publishing.
- Andreescu, S., Bucur, B., & Marty, J.-L. (2006). Affinity immobilization of tagged enzymes. I: *Immobilization of enzymes and cells* (pp. 97–106). Springer.
- Armor, J. N. (2011). A history of industrial catalysis. *Catalysis Today*, 163(1), 3–9.
- Arya, S. K., & Srivastava, S. K. (2006). Kinetics of immobilized cyclodextrin gluconotransferase produced by *Bacillus macerans* ATCC 8244. *Enzyme and Microbial Technology*, 39(3), 507–510.
- Aßmann, M., Mügge, C., Gaßmeyer, S. K., Enoki, J., Hilterhaus, L., Kourist, R., Liese, A., & Kara, S. (2017). Improvement of the process stability of arylmalonate decarboxylase by immobilization for biocatalytic profen synthesis. *Frontiers in Microbiology*, 8, 448.
- Bae, H.-S., Hong, S.-P., Lee, S.-G., Kwak, M.-S., Esaki, N., & Sung, M.-H. (2002). Application of a thermostable glutamate racemase from *Bacillus* sp. SK-1 for the production of d-phenylalanine in a multi-enzyme system. *Journal of Molecular Catalysis B: Enzymatic*, 17(6), 223–233.
- Baneyx, F., & Mujacic, M. (2004). Recombinant protein folding and misfolding in *Escherichia coli*. *Nature Biotechnology*, 22(11), 1399–1408.
- Bechtold, M., Makart, S., Reiss, R., Alder, P., & Panke, S. (2007). Model-based characterization of an amino acid racemase from *Pseudomonas putida* DSM 3263 for application in medium-constrained continuous processes. *Biotechnology and Bioengineering*, 98(4), 812–824.
- Besenhard, M. O., Chaudhury, A., Vetter, T., Ramachandran, R., & Khinast, J. G. (2015). Evaluation of parameter estimation methods for crystallization processes modeled via population balance equations. *Chemical Engineering Research and Design*, 94, 275–289.
- Bhandari, S., Carneiro, T., Lorenz, H., & Seidel-Morgenstern, A. (n.d.). *Modeling Preferential Crystallization with Racemization for Conglomerates Forming Systems using a Shortcut Model*.
- Binev, D., Seidel-Morgenstern, A., & Lorenz, H. (2016). Continuous separation of isomers in

- fluidized bed crystallizers. *Crystal Growth & Design*, 16(3), 1409–1419.
- Blehaut, J., Franco, P., Zhang, T., Lang, E., Valery, E., & Marcoux, J.-F. (2012). 9.17 *Industrial Applications of Chiral Chromatography*.
- Bollmann, J. (2020). *Experimentelle Untersuchung der Aktivität einer Aminosäuren-Racemase für neue Substrate unter geeigneten Kopplungsbedingungen mit einem vorgeschalteten enantioselektiven chromatographischen Trennprozess* (Master the). Otto-von-Guericke-Universität Magdeburg.
- Bornscheuer, U. T., & Buchholz, K. (2005). Highlights in Biocatalysis – Historical Landmarks and Current Trends. *Engineering in Life Sciences*, 5(4), 309–323.
- Boyle, J. (2005). Lehninger principles of biochemistry (4th ed.): Nelson, D., and Cox, M. *Biochemistry and Molecular Biology Education*, 33(1), 74–75.
- Bradford, M. M. (1976). A rapid and sensitive method for the quantitation of microgram quantities of protein utilizing the principle of protein-dye binding. *Analytical Biochemistry*, 72(1–2), 248–254.
- Brena, B. M., & Batista-Viera, F. (2006). Immobilization of Enzymes. I: J. M. Guisan (Ed.), *Immobilization of Enzymes and Cells* (pp. 15–30). Humana Press.
- Briggs, G. E., & Haldane, J. B. S. (1925). A note on the kinetics of enzyme action. *Biochemical Journal*, 19(2), 338.
- Calcaterra, A., & D'Acquarica, I. (2018). The market of chiral drugs: Chiral switches versus de novo enantiomerically pure compounds. *Journal of Pharmaceutical and Biomedical Analysis*, 147, 323–340.
- Canning, T. F., & Randolph, A. D. (1967). Some aspects of crystallization theory: Systems that violate McCabe's delta L law. *AIChE Journal*, 13(1), 5–10.
- Carneiro, T., Bhandari, S., Temmel, E., Lorenz, H., & Seidel-Morgenstern, A. (2019). Shortcut Model for Describing Isothermal Batch Preferential Crystallization of Conglomerates and Estimating the Productivity. *Crystal Growth & Design*, 19(9), 5189–5203.
- Carneiro, T., Wrzosek, K., Bettenbrock, K., Lorenz, H., & Seidel-Morgenstern, A. (2020). Immobilization of an amino acid racemase for application in crystallization-based chiral resolutions of asparagine monohydrate. *Engineering in Life Sciences*, 20(12), 550–561.
- Cassimjee, K. E., Kadow, M., Wikmark, Y., Humble, M. S., Rothstein, M. L., Rothstein, D. M., & Bäckvall, J.-E. (2014). A general protein purification and immobilization method on controlled porosity glass: biocatalytic applications. *Chemical Communications*, 50(65), 9134–9137.
- Chaaban, J. H., Dam-Johansen, K., Skovby, T., & Kiil, S. (2013). Separation of enantiomers by continuous preferential crystallization: Experimental realization using a coupled crystallizer configuration. *Organic Process Research & Development*, 17(8), 1010–1020.
- Chadwick, S. (1988). Ullmann's Encyclopedia of Industrial Chemistry. *Reference Services Review*, 16(4), 31–34.
- Chaplin, M., & Bucke, C. (1990). *Enzyme technology*. Cambridge University Press.

- Chen, J., Sarma, B., Evans, J. M. B., & Myerson, A. S. (2011). Pharmaceutical Crystallization. *Crystal Growth & Design*, *11*(4), 887–895.
- Coquerel, G. (2006). Preferential crystallization. I: *Novel optical resolution technologies* (pp. 1–51). Springer.
- Cornish-Bowden, A. (2012). *Fundamentals of enzyme kinetics* (4th ed.). Wiley-Blackwell.
- Doonan, S. (2002). *Peptides and proteins* (Vol. 15). Royal Society of chemistry.
- Dumesic, J. A., Huber, G. W., & Boudart, M. (2008). Principles of Heterogeneous Catalysis. I: G. Ertl, H. Knözinger, & J. Weitkamp (Eds.), *Handbook of Heterogeneous Catalysis*. Wiley-VCH Verlag GmbH & Co. KGaA.
- Ebbers, E. J., Ariaans, G. J. A., Houbiers, J. P. M., Bruggink, A., & Zwanenburg, B. (1997). Controlled racemization of optically active organic compounds: prospects for asymmetric transformation. *Tetrahedron*, *53*(28), 9417–9476.
- Eicke, M. J., Levilain, G., & Seidel-Morgenstern, A. (2013). Efficient resolution of enantiomers by coupling preferential crystallization and dissolution. Part 2: A parametric simulation study to identify suitable process conditions. *Crystal Growth & Design*, *13*(4), 1638–1648.
- Eisenthal, R., & Danson, M. J. (2002). *Enzyme assays: a practical approach* (2nd ed., Vol. 257). Oxford University Press.
- Elsner, M. P., Menéndez, D. F., Muslera, E. A., & Seidel-Morgenstern, A. (2005). Experimental study and simplified mathematical description of preferential crystallization. *Chirality*, *17*(S1), S183–S195.
- Elsner, M. P., Ziomek, G., & Seidel-Morgenstern, A. (2011). Simultaneous preferential crystallization in a coupled batch operation mode. Part II: Experimental study and model refinement. *Chemical Engineering Science*, *66*(6), 1269–1284.
- Ernst, K.-H., Wild, F. R. W. P., Blacque, O., & Berke, H. (2011). Alfred Werner's Coordination Chemistry: New Insights from Old Samples. *Angewandte Chemie International Edition*, *50*(46), 10780–10787.
- Faber, K. (2001). Non-sequential processes for the transformation of a racemate into a single stereoisomeric product: proposal for stereochemical classification. *Chemistry—A European Journal*, *7*(23), 5004–5010.
- Faber, K. (2018). *Biotransformations in Organic Chemistry: A Textbook* (7th ed.). Springer International Publishing.
- Femmer, C., Bechtold, M., & Panke, S. (2020). Semi-rational engineering of an amino acid racemase that is stabilized in aqueous/organic solvent mixtures. *Biotechnology and Bioengineering*.
- Femmer, C., Bechtold, M., Roberts, T. M., & Panke, S. (2016). Exploiting racemases. I: *Applied Microbiology and Biotechnology* (Vol. 100, Number 17, pp. 7423–7436). Springer Verlag.
- Fu, H., Dencic, I., Tibhe, J., Sanchez Pedraza, C. A., Wang, Q., Noel, T., Meuldijk, J., de Croon, M., Hessel, V., Weizenmann, N., Oeser, T., Kinkeade, T., Hyatt, D., Van Roy, S.,

- Dejonghe, W., & Diels, L. (2012). Threonine aldolase immobilization on different supports for engineering of productive, cost-efficient enzymatic microreactors. *Chemical Engineering Journal*, 207–208, 564–576.
- Fuereder, M., Femmer, C., Storti, G., Panke, S., & Bechtold, M. (2016). Integration of simulated moving bed chromatography and enzymatic racemization for the production of single enantiomers. *Chemical Engineering Science*, 152, 649–662.
- Galan, K., Eicke, M. J., Elsner, M. P., Lorenz, H., & Seidel-Morgenstern, A. (2015). Continuous preferential crystallization of chiral molecules in single and coupled mixed-suspension mixed-product-removal crystallizers. *Crystal Growth & Design*, 15(4), 1808–1818.
- Gänsch, J., Huskova, N., Kerst, K., Temmel, E., Lorenz, H., Mangold, M., Janiga, G., & Seidel-Morgenstern, A. (2021). Continuous enantioselective crystallization of chiral compounds in coupled fluidized beds. *Chemical Engineering Journal*, 422, 129627.
- Garcia-Galan, C., Berenguer-Murcia, Á., Fernandez-Lafuente, R., & Rodrigues, R. C. (2011). Potential of different enzyme immobilization strategies to improve enzyme performance. *Advanced Synthesis & Catalysis*, 353(16), 2885–2904.
- Gibbs, J. W. (1879). *On the equilibrium of heterogeneous substances*.
- Hanefeld, U., Gardossi, L., & Magner, E. (2009). Understanding enzyme immobilisation. *Chemical Society Reviews*, 38(2), 453–468.
- Harriehausen, I. (2017). *Production of pure enantiomers by coupling chromatography and crystallization based separation with racemization* (Master the). Otto-von-Guericke-Universität Magdeburg.
- Harriehausen, I., Bollmann, J., Carneiro, T., Bettenbrock, K., & Seidel-Morgenstern, A. (2021). Characterization of an Immobilized Amino Acid Racemase for Potential Application in Enantioselective Chromatographic Resolution Processes. I: *Catalysts* (Vol. 11, Number 6).
- Hein, J. E., Cao, B. H., van der Meijden, M. W., Leeman, M., & Kellogg, R. M. (2013). Resolution of omeprazole using coupled preferential crystallization: efficient separation of a nonracemizable conglomerate salt under near-equilibrium conditions. *Organic Process Research & Development*, 17(6), 946–950.
- Horn, A., Kumar, S., Liese, A., & Kragl, U. (2008). Reactions on Immobilized Biocatalysts. I: G. Ertl, H. Knözinger, & J. Weitkamp (Eds.), *Handbook of Heterogeneous Catalysis* (pp. 3831–3865). VCH Verlagsgesellschaft mbH.
- Hulburt, H. M., & Katz, S. (1964). Some problems in particle technology: A statistical mechanical formulation. *Chemical Engineering Science*, 19(8), 555–574.
- Hülsewede, D., Meyer, L., & von Langermann, J. (2019). Application of in situ product crystallization and related techniques in biocatalytic processes. *Chemistry—A European Journal*, 25(19), 4871–4884.
- Iggland, M., & Mazzotti, M. (2011). A population balance model for chiral resolution via Viedma ripening. *Crystal Growth & Design*, 11(10), 4611–4622.
- Intaraboonrod, K., Harriehausen, I., Carneiro, T., Seidel-Morgenstern, A., Lorenz, H., &

- Flood, A. E. (2020). Temperature Cycling Induced Deracemization of dl-Asparagine Monohydrate with Immobilized Amino Acid Racemase. *Crystal Growth & Design*, 21(1), 306–313.
- Jacques, J., Collet, A., & Wilen, S. H. (1994). Enantiomers, racemates and resolution, Krieger Publishing Company. *Malabar, Florida*.
- Jarvik, J. W., & Telmer, C. A. (1998). Epitope tagging. *Annual Review of Genetics*, 32(1), 601–618.
- Jeske, L., Placzek, S., Schomburg, I., Chang, A., & Schomburg, D. (2018). BRENDA in 2019: a European ELIXIR core data resource. *Nucleic Acids Research*, 47(D1), D542–D549.
- Jiang, M., & Braatz, R. D. (2019). Designs of continuous-flow pharmaceutical crystallizers: developments and practice. *CrystEngComm*, 21(23), 3534–3551.
- Johnson, I. S. (1983). Human insulin from recombinant DNA technology. *Science*, 219(4585), 632–637.
- Kaemmerer, H., Horvath, Z., Lee, J. W., Kaspereit, M., Arnell, R., Hedberg, M., Herschend, B., Jones, M. J., Larson, K., & Lorenz, H. (2012). Separation of racemic bicalutamide by an optimized combination of continuous chromatography and selective crystallization. *Organic Process Research & Development*, 16(2), 331–342.
- Kara, S., & Liese, A. (2019). Process Considerations for the Application of Enzymes. I: A. Vogel & O. May (Eds.), *Industrial Enzyme Applications* (pp. 71–94).
- Kashlev, M., Martin, E., Polyakov, A., Severinov, K., Nikiforov, V., & Goldfarb, A. (1993). Histidine-tagged RNA polymerase: dissection of the transcription cycle using immobilized enzyme. *Gene*, 130(1), 9–14.
- Koellges, T., & Vetter, T. (2018). Design and performance assessment of continuous crystallization processes resolving racemic conglomerates. *Crystal Growth & Design*, 18(3), 1686–1696.
- Köllges, T., & Vetter, T. (2016). Model-based analysis of continuous crystallization/reaction processes separating conglomerate forming enantiomers. *Crystal Growth & Design*, 17(1), 233–247.
- Levilain, G., & Coquerel, G. (2010). Pitfalls and rewards of preferential crystallization. *CrystEngComm*, 12(7), 1983–1992.
- Levilain, G., Rougeot, C., Guillen, F., Plaquevent, J.-C., & Coquerel, G. (2009). Attrition-enhanced preferential crystallization combined with racemization leading to redissolution of the antipode nuclei. *Tetrahedron: Asymmetry*, 20(24), 2769–2771.
- Lim, Y.-H., Yokoigawa, K., Esaki, N., & Soda, K. (1993). A new amino acid racemase with threonine alpha-epimerase activity from *Pseudomonas putida*: purification and characterization. *Journal of Bacteriology*, 175(13), 4213–4217.
- Liu, Y., Wang, X., Wang, J., & Ching, C. B. (2004). Structural characterization and enantioseparation of the chiral compound praziquantel. *Journal of Pharmaceutical Sciences*, 93(12), 3039–3046.

- Lorenz, H. (2013). Solubility and solution equilibria in crystallization. *Crystallization: Basic Concepts and Industrial Applications*, 35–74.
- Lorenz, H., Perlberg, A., Sapoundjiev, D., Elsner, M. P., & Seidel-Morgenstern, A. (2006a). Crystallization of enantiomers. *Chemical Engineering and Processing: Process Intensification*, 45(10), 863–873.
- Lorenz, H., Polenske, D., & Seidel-Morgenstern, A. (2006b). Application of preferential crystallization to resolve racemic compounds in a hybrid process. *Chirality: The Pharmacological, Biological, and Chemical Consequences of Molecular Asymmetry*, 18(10), 828–840.
- Lorenz, H., Sapoundjiev, D., & Seidel-Morgenstern, A. (2002). Enantiomeric mandelic acid system melting point phase diagram and solubility in water. *Journal of Chemical & Engineering Data*, 47(5), 1280–1284.
- Lorenz, H., & Seidel-Morgenstern, A. (2014). Processes To Separate Enantiomers. *Angewandte Chemie International Edition*, 53(5), 1218–1250.
- Lorenz, H., & Seidel-Morgenstern, A. (2020). Separation Processes to Provide Pure Enantiomers and Plant Ingredients. *Annual Review of Chemical and Biomolecular Engineering*, 11(1), 469–502.
- Majumder, A., & Nagy, Z. (2017). A comparative study of coupled preferential crystallizers for the efficient resolution of conglomerate-forming enantiomers. *Pharmaceutics*, 9(4), 55.
- Mateo, C., Palomo, J. M., Fernandez-Lorente, G., Guisan, J. M., & Fernandez-Lafuente, R. (2007). Improvement of enzyme activity, stability and selectivity via immobilization techniques. *Enzyme and Microbial Technology*, 40(6), 1451–1463.
- McCabe, W. L. (1929). Crystal growth in aqueous solutions1: I—Theory. *Industrial & Engineering Chemistry*, 21(1), 30–33.
- Mersmann, A. (2001). *Crystallization technology handbook*. CRC Press.
- Mohan, R., Lorenz, H., & Myerson, A. S. (2002). Solubility Measurement Using Differential Scanning Calorimetry. *Industrial & Engineering Chemistry Research*, 41(19), 4854–4862.
- Mullin, J. W. (2001). *Crystallization* (Fourth ed). Butterworth-Heinemann.
- Murakami, K., Ohashi, M., Matsunaga, A., Yamamoto, I., & Nohira, H. (1993). Asymmetric transformation of a racemic  $\alpha$ -(phthalimidooxy) arylacetic ester by a combination of preferential crystallization and simultaneous racemization. *Chirality*, 5(1), 41–48.
- Murray, R. K., Granner, D. K., Mayes, P. A., & Rodwell, V. W. (2014). *Harper's illustrated biochemistry*. Mcgraw-hill.
- Myerson, A. (2002). *Handbook of industrial crystallization*. Butterworth-Heinemann.
- Nagy, Z. K., Fevotte, G., Kramer, H., & Simon, L. L. (2013). Recent advances in the monitoring, modelling and control of crystallization systems. *Chemical Engineering Research and Design*, 91(10), 1903–1922.
- National Center for Biotechnology Information. (n.d.). *PubChem Compound Summary for*

- CID 6267, *Asparagine*. Retrieved August 10, 2020, from <https://pubchem.ncbi.nlm.nih.gov/compound/Asparagine>
- Nernst, W. (1904). Theorie der Reaktionsgeschwindigkeit in heterogenen Systemen. *Zeitschrift Für Physikalische Chemie*, 47(1), 52–55.
- Nestl, B. M., Bodlener, A., Stuermer, R., Hauer, B., Kroutil, W., & Faber, K. (2007). Biocatalytic racemization of synthetically important functionalized  $\alpha$ -hydroxyketones using microbial cells. *Tetrahedron Asymmetry*, 18(12), 1465–1474.
- Noorduyn, W. L., van Enkevort, W. J. P., Meekes, H., Kaptein, B., Kellogg, R. M., Tully, J. C., McBride, J. M., & Vlieg, E. (2010). The driving mechanism behind attrition-enhanced deracemization. *Angewandte Chemie International Edition*, 49(45), 8435–8438.
- Noyes, A. A., & Whitney, W. B. (1897). Über die Auflösungsgeschwindigkeit von festen Stoffen in ihren eigenen Lösungen. *Zeitschrift Für Physikalische Chemie*, 23(1), 689–692.
- Oketani, R., Hoquante, M., Brandel, C., Cardinael, P., & Coquerel, G. (2018). Practical role of racemization rates in deracemization kinetics and process productivities. *Crystal Growth & Design*, 18(11), 6417–6420.
- Overton, T. W. (2014). Recombinant protein production in bacterial hosts. *Drug Discovery Today*, 19(5), 590–601.
- Petruševska-Seebach, K. (2012). *Overcoming Yield Limitations when Resolving Racemates by Combination of Crystallization And, Or Chromatography with Racemization*. Docupoint-Verlag.
- Petruševska-Seebach, K., Würges, K., Seidel-Morgenstern, A., Lütz, S., & Elsner, M. P. (2009). Enzyme-assisted physicochemical enantioseparation processes-Part II: Solid-liquid equilibria, preferential crystallization, chromatography and racemization reaction. *Chemical Engineering Science*, 64(10), 2473–2482.
- Pieracci, J. P., Armando, J. W., Westoby, M., & Thommes, J. (2018). Industry Review of Cell Separation and Product Harvesting Methods. I: *Biopharmaceutical Processing: Development, Design, and Implementation of Manufacturing Processes* (pp. 165–206). Elsevier.
- Pithani, S., Karlsson, S., Emtenäs, H., & Öberg, C. T. (2019). Using Spinchem Rotating Bed Reactor Technology for Immobilized Enzymatic Reactions: A Case Study. *Organic Process Research & Development*, 23(9), 1926–1931.
- Porath, J., Carlsson, J. A. N., Olsson, I., & Belfrage, G. (1975). Metal chelate affinity chromatography, a new approach to protein fractionation. *Nature*, 258(5536), 598.
- Radkov, A. D., & Moe, L. A. (2013). Amino acid racemization in *Pseudomonas putida* KT2440. *Journal of Bacteriology*, 195(22), 5016–5024.
- Ramkrishna, D. (2000). *Population balances: Theory and applications to particulate systems in engineering*. Elsevier.
- Ramkrishna, D., & Singh, M. R. (2014). Population balance modeling: current status and future prospects. *Annual Review of Chemical and Biomolecular Engineering*, 5, 123–

146.

- Randolph, A. D., & Larson, M. A. (1988). *Theory of particulate processes : analysis and techniques of continuous crystallization* (2. ed.). I: Academic Press.
- Rao, N. N., Lütz, S., Seelbach, K., & Liese, A. (2006). Basics of Bioreaction Engineering. I: *Industrial Biotransformations* (pp. 115–145).
- Rodrigues, R. C., Ortiz, C., Berenguer-Murcia, Á., Torres, R., & Fernández-Lafuente, R. (2013). Modifying enzyme activity and selectivity by immobilization. *Chemical Society Reviews*, 42(15), 6290–6307.
- Roozeboom, H. W. B. (1899). Solubility and melting-point as criteria for racemate compounds, pseudoracemic mix-crystals and inactive conglomerates. *Z. Phys. Chem. Stoichiometrie Verwandtschaftslehre*, 28, 494–517.
- Rosano, G. L., & Ceccarelli, E. A. (2014). Recombinant protein expression in *Escherichia coli*: advances and challenges. *Frontiers in Microbiology*, 5, 172.
- Schnell, B., Faber, K., & Kroutil, W. (2003). Enzymatic racemisation and its application to synthetic biotransformations. *Advanced Synthesis & Catalysis*, 345(6-7), 653–666.
- Sheldon, R. A. (2007). Enzyme immobilization: the quest for optimum performance. *Advanced Synthesis & Catalysis*, 349(8-9), 1289–1307.
- Sheldon, R. A., & van Pelt, S. (2013). Enzyme immobilisation in biocatalysis: why, what and how. *Chemical Society Reviews*, 42(15), 6223–6235.
- Sheldon, R. A., & Woodley, J. M. (2017). Role of biocatalysis in sustainable chemistry. *Chemical Reviews*, 118(2), 801–838.
- Sifniades, S., Boyle Jr, W. J., & Van Peppen, J. F. (1976). Synthesis of L-lysine. Simultaneous resolution/racemization of. alpha.-amino-. epsilon.-caprolactam. *Journal of the American Chemical Society*, 98(12), 3738–3739.
- Singh, V. P., Guo, H., & Yu, F. X. (1993). Parameter estimation for 3-parameter log-logistic distribution (LLD3) by Pome. *Stochastic Hydrology and Hydraulics*, 7(3), 163–177.
- Soriano-Maldonado, P., Las Heras-Vazquez, F. J., Clemente-Jimenez, J. M., Rodriguez-Vico, F., & Martínez-Rodríguez, S. (2015). Enzymatic dynamic kinetic resolution of racemic N-formyl- and N-carbamoyl-amino acids using immobilized L-N-carbamoylase and N-succinyl-amino acid racemase. *Applied Microbiology and Biotechnology*, 99(1), 283–291.
- Srisanga, S., Flood, A. E., Galbraith, S. C., Rugmai, S., Soontaranon, S., & Ulrich, J. (2015). Crystal growth rate dispersion versus size-dependent crystal growth: appropriate modeling for crystallization processes. *Crystal Growth & Design*, 15(5), 2330–2336.
- Suwannasang, K., Flood, A. E., & Coquerel, G. (2016). A novel design approach to scale up the temperature cycle enhanced deracemization process: coupled mixed-suspension vessels. *Crystal Growth & Design*, 16(11), 6461–6467.
- Suwannasang, K., Flood, A. E., Rougeot, C., & Coquerel, G. (2013). Using programmed heating-cooling cycles with racemization in solution for complete symmetry breaking of a conglomerate forming system. *Crystal Growth and Design*, 13(8), 3498–3504.

- Talbert, J. N., & Goddard, J. M. (2012). Enzymes on material surfaces. *Colloids and Surfaces B: Biointerfaces*, 93, 8–19.
- Tavare, N. S., & Tavare, N. S. (1995). Crystallization Techniques and Phenomena. I: *Industrial Crystallization* (pp. 465–499). Springer US.
- Temmel, E., Eisenschmidt, H., Lorenz, H., Sundmacher, K., & Seidel-Morgenstern, A. (2016). A short-cut method for the quantification of crystallization kinetics. 1. Method development. *Crystal Growth & Design*, 16(12), 6743–6755.
- Temmel, E., Gänsch, J., Lorenz, H., & Seidel-Morgenstern, A. (2018). Measurement and evaluation of the crystallization kinetics of L-asparagine monohydrate in the ternary L-/D-asparagine/water system. *Crystal Growth & Design*, 18(12), 7504–7517.
- Temmel, E., Gänsch, J., Seidel-Morgenstern, A., & Lorenz, H. (2020). Systematic investigations on continuous fluidized bed crystallization for chiral separation. *Crystals*, 10(5), 394.
- Thompson, M. P., Derrington, S. R., Heath, R. S., Porter, J. L., Mangas-Sanchez, J., Devine, P. N., Truppo, M. D., & Turner, N. J. (2019). A generic platform for the immobilisation of engineered biocatalysts. *Tetrahedron*, 75(3), 327–334.
- Todorova, D., & Vijayalakshmi, M. A. (2005). Immobilized metal-ion affinity chromatography. I: D. S. Hage & J. Cazes (Eds.), *Handbook of affinity chromatography*. CRC Press Boca Raton.
- Tufvesson, P., Lima-Ramos, J., Nordblad, M., & Woodley, J. M. (2011). Guidelines and cost analysis for catalyst production in biocatalytic processes. *Organic Process Research & Development*, 15(1), 266–274.
- Tung, H.-H., Paul, E. L., Midler, M., & McCauley, J. A. (2009). *Crystallization of organic compounds: an industrial perspective*. John Wiley & Sons.
- Ulrich, J. (1989). Growth rate dispersion — a review. *Crystal Research and Technology*, 24(3), 249–257.
- Viedma, C. (2005). Chiral symmetry breaking during crystallization: complete chiral purity induced by nonlinear autocatalysis and recycling. *Physical Review Letters*, 94(6), 65504.
- Viedma, C., & Cintas, P. (2011). Homochirality beyond grinding: deracemizing chiral crystals by temperature gradient under boiling. *Chemical Communications*, 47(48), 12786–12788.
- Vogel, A., & May, O. (2019). *Industrial enzyme applications* (A. Vogel & O. May (eds.)). John Wiley & Sons.
- Volmer, M. (1939). *Kinetik der phasenbildung*.
- Webb, E. C. (1992). *Enzyme nomenclature 1992. Recommendations of the Nomenclature Committee of the International Union of Biochemistry and Molecular Biology on the Nomenclature and Classification of Enzymes* (Number Ed. 6). Academic Press.
- Wilson, K., & Walker, J. (2010). *Principles and techniques of biochemistry and molecular biology* (K. Wilson & J. Walker (eds.); 7th ed.). Cambridge university press.
- Wöltinger, J., Karau, A., Leuchtenberger, W., & Drauz, K. (2005). Membrane Reactors at

- Degussa. I: U. Kragl (Ed.), *Technology Transfer in Biotechnology: From lab to Industry to Production* (pp. 289–316). Springer Berlin Heidelberg.
- Wood, B., Girard, K. P., Polster, C. S., & Croker, D. M. (2019). Progress to date in the design and operation of continuous crystallization processes for pharmaceutical applications. *Organic Process Research & Development*, *23*(2), 122–144.
- Wrzosek, K., Harriehausen, I., & Seidel-Morgenstern, A. (2018). Combination of Enantioselective Preparative Chromatography and Racemization: Experimental Demonstration and Model-Based Process Optimization. *Organic Process Research & Development*, *22*(12), 1761–1771.
- Wuerges, K. (2011). *Enzyme supported crystallization of chiral amino acids* (Vol. 40). Forschungszentrum Jülich.
- Würges, K., Petruševska-Seebach, K., Elsner, M. P., & Lütz, S. (2009a). Enzyme-assisted physicochemical enantioseparation processes - Part III: Overcoming yield limitations by dynamic kinetic resolution of asparagine via preferential crystallization and enzymatic racemization. *Biotechnology and Bioengineering*, *104*(6), 1235–1239.
- Würges, K., Petruševska, K., Serci, S., Wilhelm, S., Wandrey, C., Seidel-Morgenstern, A., Elsner, M. P., & Lütz, S. (2009b). Enzyme-assisted physicochemical enantioseparation processes: Part I. Production and characterization of a recombinant amino acid racemase. *Journal of Molecular Catalysis B: Enzymatic*, *58*(1–4), 10–16.
- Xiouras, C., Fytopoulos, A. A., Ter Horst, J. H., Boudouvis, A. G., Van Gerven, T., & Stefanidis, G. D. (2018). Particle breakage kinetics and mechanisms in attrition-enhanced deracemization. *Crystal Growth & Design*, *18*(5), 3051–3061.
- Yamada, S., Yamamoto, M., & Chibata, I. (1973). Optical resolution of DL-lysine by preferential crystallization procedure. *Journal of Agricultural and Food Chemistry*, *21*(5), 889–894.
- Yoshioka, R. (2006). Racemization, optical resolution and crystallization-induced asymmetric transformation of amino acids and pharmaceutical intermediates. I: T. R. Sakai K., Hirayama N. (Ed.), *Topics in Current Chemistry* (Novel Opti, Vol. 269, pp. 83–132). Springer, Berlin, Heidelberg.

## Appendix

### A.1 Coordinate transformation

The transformation from the ternary phase diagram to the Cartesian (XY-orthogonal) coordinate system and vice-versa have been determined by geometry. The triangle-shaped diagram was placed in the Cartesian plane as depicted in Figure A.1. The scheme is in accordance with the following description:

- The three components are named 1, 2 and 3 and their respective mass fractions are  $w_1$ ,  $w_2$  and  $w_3$ .
- The total mass balance follows:  $w_1 + w_2 + w_3 = 1$ .
- The side length of the equilateral triangle is 1. Hence, by geometry the height  $h$  of the triangle is  $\frac{\sqrt{3}}{2}$ .
- The triangle side  $\overline{12}$  is located on the  $X$  axis of the Cartesian plane.
- The triangle vertex 1 is placed at the origin (0,0) of the XY-orthogonal system.

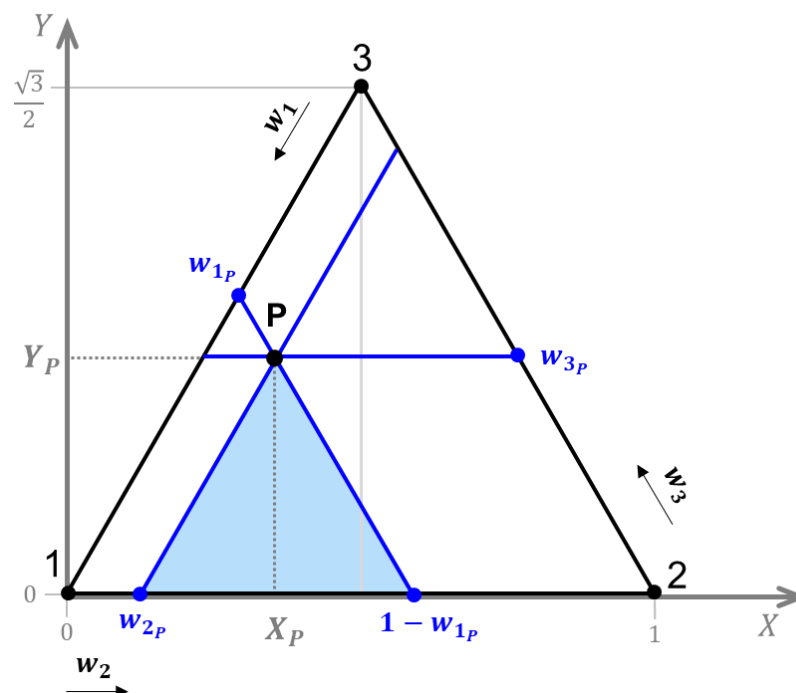


**Figure A.1** Illustration of relation between Cartesian XY-coordinates and mass fractions on the ternary phase diagram. The blue area is formed for any given ternary mixture P represented in the diagram. It works as a reference for the equations of coordinate transformation.

As a result, the coordinates  $(X, Y)$  of the vertices 1, 2 and 3 are  $(0,0)$ ,  $(1,0)$  and  $(\frac{1}{2}, \frac{\sqrt{3}}{2})$ , respectively. The coordinates for an arbitrary point P in the diagram are  $(X_P, Y_P)$  and  $(w_{1P}, w_{2P}, w_{3P})$ . By connecting the point P to its mass fraction points located on the sides of the TPD, an equilateral triangle is formed inside the phase diagram (blue area in Figure A.1). That is the reference area for the coordinate transformation. The X-coordinate is the middle point between the mass fractions vertices  $w_{2P}$  and  $(1 - w_{1P})$ . Hence:

$$X_P = \frac{1}{2}(1 - w_{1P} + w_{2P}) \quad (\text{A.1})$$

The Y-coordinate is the height of the equilateral triangle, which has a side of length  $(1 - w_{1P} - w_{2P})$ , therefore:

$$Y_P = \frac{\sqrt{3}}{2}(1 - w_{1P} - w_{2P}) \quad (\text{A.2})$$

The reverse transformations are then given by the following equations:

$$w_{1P} = 1 - X_P - \frac{Y_P}{\sqrt{3}} \quad (\text{A.3})$$

$$w_{2P} = X_P - \frac{Y_P}{\sqrt{3}} \quad (\text{A.4})$$

The mass fraction  $w_{3P}$  is bound to the composition of the other two components by the total mass balance equation. The ternary phase diagram and the component mass fractions can be easily plotted and manipulated by these equations. They were used in the shortcut model to facilitate mass balance calculations of the ternary mixtures.

## A.2 List of variables for simulations

The variables used on the shortcut model to simulate PC of asparagine monohydrate are summarized in the table below. Since the initial solutions applied in the process were racemic, the initial liquid phase conditions of enantiomers 1 and 2 are the same. The initial particle radius of enantiomer 1 was approximated from the average length value of seed mass distribution used during experiments, which was 90 to 125  $\mu\text{m}$ .

**Table A.1** Summary of SCM variables used to simulate experimental data.

Experiment	Parameter	Value	Unit	Comment
I	$w_i^0$	0.0456	g/g	Initial mass fraction of enantiomer $i$
II		0.0495	g/g	
III		0.0557	g/g	
IV		0.0368	g/g	
I	$m_i^0$	9.15	g	Initial mass of enantiomer $i$ in the liquid phase
II		10.02	g	
III		11.43	g	
IV		7.24	g	
all	$w_{ratio}$	2.07	-	Solubility ratio
all	$M_S$	150.13	g/mol	Molar mass of monohydrate enantiomer
all	$M_i$	132.12	g/mol	Molar mass of anhydrous enantiomer
all	$m_{seeds}$	0.20	g	Mass of seeds
all	$\rho_S$	1.543	g/cm <sup>3</sup>	Density of the solid phase
all	$R_1^0$	$50 \times 10^{-4}$	cm	Initial radius of solid enantiomer 1
all	$R_2^0$	$50 \times 10^{-9}$	cm	Initial radius of solid enantiomer 2

## List of Contributions

### Publications

Harriehausen, I., Bollmann, J., **Carneiro, T.**, Bettenbrock, K., Seidel-Morgenstern, A. (2021) Characterization of an Immobilized Amino Acid Racemase for Potential Application in Enantioselective Chromatographic Resolution Processes. *Catalysts*, 11, 726.

Kritsada I., Harriehausen I., **Carneiro T.**, Seidel-Morgenstern A., Lorenz H., & Flood A. E. (2020). Temperature Cycling Induced Deracemization of D1-Asparagine Monohydrate with Immobilized Amino Acid Racemase. *Crystal Growth & Design* 21 (1): 306–13.

**Carneiro, T.**, Wrzosek, K., Bettenbrock, K., Lorenz, H., & Seidel-Morgenstern, A. (2020). Immobilization of an amino acid racemase for application in crystallization-based chiral resolutions of asparagine monohydrate. *Engineering in Life Sciences*, 20(12), 550–561.

**Carneiro, T.**, Bhandari, S., Temmel, E., Lorenz, H., & Seidel-Morgenstern, A. (2019). Shortcut Model for Describing Isothermal Batch Preferential Crystallization of Conglomerates and Estimating the Productivity. *Crystal Growth & Design*, 19(9), 5189–5203.

**Carneiro T.**, Bettenbrock K., Lorenz H., & Seidel-Morgenstern A.. (2016). Combination of Preferential Crystallization and Racemization—First Results. In *BIWIC 2016: 23<sup>rd</sup> International Workshop on Industrial Crystallization*, 173–78. Göttingen: CuvillierVerlag.

### Conferences

15<sup>th</sup> Annual Meeting American Institute of Chemical Engineers, AIChE 2018. Pittsburgh, USA. Oct. 28 – Nov. 2, 2018. T. Carneiro, S. Bhandari, K. Wrzosek, E. Temmel, H. Lorenz and A. Seidel-Morgenstern. Resolution of conglomerates using preferential crystallization and enzymatic racemization. (Oral presentation)

9<sup>th</sup> International Congress on Biocatalysis, Biocat 2018. Hamburg, Germany. Aug 26 – 30, 2018. T. Carneiro, K. Wrzosek, A. Seidel-Morgenstern. Application of an immobilized biocatalyst to increase the performance of crystallization-based enantioseparation. (Poster, won poster award)

Himmelfahrtstagung 2018: Heterogeneities - A key for understanding and upscaling of bioprocesses in up- and downstream. Magdeburg, Germany. May 7 – 9, 2018. T. Carneiro, K. Wrzosek and A. Seidel-Morgenstern. Integration of enzymatic racemization and preferential crystallization to improve production of pure enantiomers. (Poster)

10<sup>th</sup> World Congress of Chemical Engineering, WCCE10. Barcelona, Spain. Oct 1 – 5, 2017. T. Carneiro, K. Wrzosek, H. Lorenz, and A. Seidel-Morgenstern. Study of integrated enzymatic racemization to improve production of pure enantiomers. (Poster)

20<sup>th</sup> International Symposium on Industrial Crystallization, ISIC20. Dublin, Ireland. Sep 3 – 6, 2017. T. Carneiro, K. Wrzosek, H. Lorenz, and A. Seidel-Morgenstern. Optical resolution of conglomerates by combination of Preferential Crystallization and enzymatic racemization. (Poster)

Jahrestreffen der ProcessNet-Fachgruppen Mechanische Flüssigkeitsabtrennung und Kristallisation. Cologne, Germany. Mar 6 – 10, 2017. T. Carneiro, H. Lorenz, and A. Seidel-Morgenstern. Application of enzymatic racemization and Preferential Crystallization for production of pure enantiomers. (Oral presentation)

23rd International Workshop on Industrial Crystallization, BIWIC. Magdeburg, Germany. September 6 – 8, 2016. T. Carneiro, K. Bettenbrock, H. Lorenz, and A. Seidel-Morgenstern. Combination of Preferential Crystallization and Racemization – First Results. (Poster)

8<sup>th</sup> International Congress on Biocatalysis, Biocat 2016. Hamburg, Germany. Aug 28 – Sep 1, 2016. T. Carneiro, K. Bettenbrock, H. Lorenz, and A. Seidel-Morgenstern. Investigation of an amino acid racemase for enantioseparation using preferential crystallization. (Poster)

5<sup>th</sup> International School of Crystallization, ISC2016. Granada, Spain. May 29 – Jun 3, 2016. T. Carneiro, K. Bettenbrock, H. Lorenz, and A. Seidel-Morgenstern. Initial investigation of combined preferential crystallization and enzymatic racemization. (Poster)